Transient, Laser-Driven Volume Plasma Density Structures

George Kenneth Holt

A thesis presented for the degree of

Doctory of Philosophy in Physics

Department of Physics

University of Strathclyde, Glasgow

2022

Signed:

Date:

Abstract

This thesis presents a study of time-dependent plasma density gratings formed by the forces of intersecting high-intensity, short-pulse lasers in gas and plasma. Such structures have been proposed as optical components for the manipulation of laser pulses with intensities beyond the damage threshold of conventional optical devices based on solid state technology. Two methods of plasma density grating formation are considered, both of which rely on the beat wave of two or more laser fields – (i) by ionisation of a neutral gas, and (ii) by driving an inertially evolving grating using the ponderomotive force in plasma.

A novel amplification method based on the interaction of a probe laser pulse with an evolving plasma density modulation, driven by ionisation, is identified and analysed theoretically, numerically and experimentally. Experimental evidence for the formation of a plasma density grating by counterpropagating high-power laser pulses in underdense plasma is presented, along with the first demonstration of the manipulation of the phase of a 100-femtosecond probe laser pulse by a plasma density grating. A peak phase shift of $\pi/4$ is measured.

A particle-in-cell study of the use of plasma density gratings for controlling laser wakefield accelerators is presented. It is found that the plasma density grating modifies the velocity of the back of the laser wakefield bubble and, through a simulation parameter scan, it is shown that the properties of the electron beam depend strongly on the amplitude and placement of the plasma density grating within the accelerator target.

List of Figures

List of Tables

Acknowledgements

This work would not have been possible without the support, patience and belief of a large number of people. In the following, I have attempted to distil the impact of several individuals on my experiences relating to this work over these last years. This is an insurmountable task. To each of you – please know that my gratitude is endless.

First, I would like to thank Prof. Dino Jaroszynski, my primary supervisor, for his tireless assistance, our fruitful discussions, and affording me the freedom to pursue the ideas I found most interesting. I sincerely acknowledge Dr. Bernhard Ersfeld for his expertise in building rigorous mathematical models based on experimental and numerical observations. I owe thanks to Dr. Gregory Vieux, in particular for his ambitious goals and thorough experimental skills, and also for his exceptional data organisation and record-keeping. I am indebted to Dr. Sam Yoffe for his Python wizardry, simulation code mastery and guidance on the trickier nuances of statistics. In addition, his coffee and whisky recommendations have helped me to stay focused and relaxed, in almost equal measure. I thank Dr. Enrico Brunetti for his helpful introductions to the field of laser-plasma physics and for ensuring that no technical problem delayed our research progress; Dr. Adam Noble for his wise and reassuring words regarding imposter syndrome; and Dr. Mohammed Shahzad for all the days spent in various labs.

Those outside of the academic setting have had no less impression on this work than those within. To Alex, whose unwavering support, kind understanding of my often ridiculous problems, and relentless patience has been my foundation – I am entirely beholden. Thanks to Lucas, Antoine and Ulle for the drinks, meals and rants, and to William and Ellen for making sure I took some time off and looked after myself. My dear granny and grandpa have my deepest appreciation for their unending belief. Finally, my deepest thanks to my parents, whose absolute love and support have been and always will be cherished gifts that I will forever reciprocate.

Role of the author

Particle-in-cell simulations with the EPOCH and FBPIC codes were performed by the author, who deployed and ran the software on the ARCHER, ARCHER2 and Cirrus supercomputing facilities and local hardware. Management, visualisation and analysis of the resulting data was performed by the author. The theoretical model for electromagnetic wave interaction with an evolving ionisation grating was developed by Dr. Bernhard Ersfeld. Modelling of the interaction of a probe beam with a transient ionisation and ponderomotive grating was performed by the author.

The author assisted in the design of the experiment conducted at the Central Laser Facility, Rutherford Appleton Laboratory, which was led by Dr. Grégory Vieux. The author, working with others in the experimental team, constructed the main pump paths, probe beam paths, diagnostics for one of the pump beams and diagnostics for both probe beams. Experimental data visualisation and analysis was performed by the author. The nozzle used in the experiment was designed by Dr. Grégory Vieux and fluid simulations were performed by Andrzej Kornaszewski.

Prof. Dino Jaroszynski came up with the original project idea and contributed at every stage to steer the research in interesting and promising directions.

General supervision and assistance was provided to the author throughout by Prof. Dino Jaroszynski and Drs. Grégory Vieux, Sam Yoffe, Bernhard Ersfeld and Enrico Brunetti.

Contents

Chapter 1

Introduction

High-power lasers have been a major enabler of discovery and innovation since the application of the chirped pulse amplification (CPA) technique to lasers in the mid-1980s [1], for which the Nobel Prize in Physics was awarded to Donna Strickland and Gérard Mourou in 2018. In their 2020 report on ultra-high intensity laser facilities worldwide [2], the International Committee on Ultra-high Intensity Lasers (ICUIL) listed over 100 facilities in more than 20 countries. This represents a stark increase in the prevalence of such facilities since the first review paper on high-power, ultra-fast lasers in 1998, which detailed a single petawatt-class laser system [3]. These laser systems are used across a plethora of research activities, including particle acceleration [4, 5], new mechanisms of radiation generation [6, 7], laboratory astrophysics [8, 9], nuclear fusion for energy production [10], and many others. The advent of turnkey, university-scale laser systems with peak powers in the multi-terawatt range and exceeding 10 TW is driving significant advancements in their applications in industrial and medical environments [11–16]. The peak irradiance of the highest intensity laser pulses now exceeds $10^{23}\,\mathrm{W\,cm^{-2}}$ [17], which permits the study of the (hitherto unreachable) regime of strong field quantum electrodynamics [18–20].

High-power lasers have also instigated the novel research area of plasma optics, in which intense laser pulses interact with plasma to (i) perform similar functions to existing solid state optical devices, but with unique properties, and (ii) facilitate useful and interesting optical processes that are not otherwise possible with established technologies.

Plasma-based optical devices can (theoretically) have significantly higher damage thresholds than their solid state or gas-based counterparts (where they exist) due to plasma being a medium that is already ionised. This property makes them attractive candidates for use in future generation high-power lasers because they can potentially increase the robustness of the system. Schemes based on Raman [21–24] and Brillouin [25, 26] processes propose promising alternatives to conventional amplification methods that may further increase achievable laser powers. Plasma mirrors are routinely used to significantly enhance the temporal contrast of high-power lasers [27, 28] and are also able to holographically manipulate ultra-intense beams [29] and scatter attosecond-duration high-harmonic pulse trains [30]. Plasma structured by the ponderomotive force associated with colliding laser pulses has been proposed as a novel medium for controlling the polarisation of [31] and directing [32, 33] high-power laser beams and acting as a holographic lens [34] or double-pass chirped pulse amplifier [35].

This thesis presents a study of volume plasma density gratings created by intersecting laser pulses in underdense plasma. Ch. 2 introduces the key laser and plasma definitions and gives a review of the processes and phenomena that are built upon in the subsequent sections. A numerical and theoretical investigation into the formation of volume plasma density gratings and their interactions with probing laser pulses is discussed in Ch. 3. Ch. 4 reports on the results of an experiment conducted to investigate the creation of a volume plasma density grating and its use as a waveplate. A novel method of controlling electron beam injection dynamics in a laser wakefield accelerator by using a volume plasma density grating is proposed in Ch. 5. Finally, conclusions and suggested future research areas of interest are presented in Ch. 6.

Chapter 2

Laser interaction with matter

A thorough understanding of the interaction of high-intensity laser fields with gas or plasma requires a firm grasp of several fundamental and derived processes. This chapter introduces the basic theory and concepts necessary for describing the dynamics of laser-matter interaction, and provides additional background. The chapter is divided into three main sections – Sec. 2.1 'Light', Sec. 2.2 'Light-matter interactions' and Sec. 2.3 'Laser-plasma interactions'. Sec. 2.1 introduces the fundamental concept of electromagnetism using Maxwell's equations, Gaussian laser pulses, and high-power, short-pulse lasers. Sec. 2.2 discusses the mechanisms of photoionisation, the elucidating example of a charged particle interacting with an infinite plane wave, and the ponderomotive force. Sec. 2.3 gives a general description of plasma and describes two key wave modes in plasma (electromagnetic and Langmuir), introduces the concept of laser wakefield acceleration, discusses the evolution of a laser pulse in plasma and presents an overview of simulations of plasma using the kinetic method.

2.1 Light

A description of light presents a logical jumping-off point for providing a necessary theoretical background to the processes studied in this thesis. Electromagnetism describes the dynamics of laser pulses, which are propagating electromagnetic waves. It is also necessary for investigating the motion of charged particles and plasma and their interactions with light.

2.1.1 Electromagnetism

The propagation of electric ($\vec{E}$) and magnetic ($\vec{B}$) fields and their interaction with charge (ρ) and current ($\vec{j}$) densities is governed by Maxwell's equations [36]

$$\nabla \cdot \vec{E} = \frac{\rho}{\varepsilon_0}, \tag{2.1a}$$

$$\nabla \cdot \vec{B} = 0, \tag{2.1b}$$

$$\nabla \times \vec{E} = -\frac{\partial \vec{B}}{\partial t}, \tag{2.1c}$$

$$\nabla \times \vec{B} = \mu_0 \varepsilon_0 \frac{\partial \vec{E}}{\partial t} + \mu_0 \vec{j}, \tag{2.1d}$$

where ε_0 and μ_0 are the permittivity and permeability of vacuum, respectively, and $\frac{\partial}{\partial t}$ is the derivative with respect to time. Using the vector identities[1]

$$\nabla \cdot \left(\nabla \times \vec{A}\right) = 0, \tag{2.2}$$

$$\nabla \times (\nabla \phi) = 0, \tag{2.3}$$

the electric and magnetic fields can also be expressed in terms of a magnetic vector potential $\vec{A}$ and electric scalar potential ϕ:

$$\vec{E} = -\nabla \phi - \frac{\partial \vec{A}}{\partial t}, \tag{2.4}$$

$$\vec{B} = \nabla \times \vec{A}. \tag{2.5}$$

Using these definitions and Eqns. (2.1a) and (2.1d), we arrive at Maxwell's equations in potential form

$$\nabla^2 \phi + \nabla \cdot \frac{\partial \vec{A}}{\partial t} = -\frac{\rho}{\varepsilon_0}, \tag{2.6}$$

$$\nabla^2 \vec{A} - \mu_0 \varepsilon_0 \frac{\partial^2 \vec{A}}{\partial t^2} = -\mu_0 \vec{j} + \nabla \left(\mu_0 \varepsilon_0 \frac{\partial \phi}{\partial t} + \nabla \cdot \vec{A}\right), \tag{2.7}$$

which is a system of coupled equations that does not have a unique solution in general. The process of gauge fixing allows sufficient constraints to be placed on the system to find solutions when initial and boundary conditions are known. Two commonly used

[1]For any vector field $\vec{A}$ and scalar field ϕ.

gauges are the Coulomb and Lorenz gauges. The former sets $\nabla \cdot \vec{A} = 0$, which yields a simple expression for the electric potential but an unwieldy one for the magnetic potential and is most useful for electrostatic problems. The Lorenz gauge sets

$$\nabla \cdot \vec{A} + \varepsilon_0 \mu_0 \frac{\partial \phi}{\partial t} = 0, \tag{2.8}$$

which yields

$$\varepsilon_0 \mu_0 \frac{\partial^2 \phi}{\partial t^2} - \nabla^2 \phi = \frac{\rho}{\varepsilon_0}, \tag{2.9}$$

$$\varepsilon_0 \mu_0 \frac{\partial^2 \vec{A}}{\partial t^2} - \nabla^2 \vec{A} = \mu_0 \vec{j}. \tag{2.10}$$

In contrast to the Coulomb gauge, ϕ and $\vec{A}$ are decoupled in the Lorenz gauge. In vacuum,

$$\varepsilon_0 \mu_0 \frac{\partial^2 \vec{A}}{\partial t^2} = \nabla^2 \vec{A}, \tag{2.11}$$

with a special solution

$$\vec{A}\left(\vec{x}, t\right) = \vec{A}_0 \mathrm{e}^{\mathrm{i}\left(\vec{k}\cdot\vec{x} - \omega t + \varphi\right)}, \tag{2.12}$$

which is a plane wave travelling in the x-direction with velocity $c = \left(\varepsilon_0 \mu_0\right)^{-\frac{1}{2}}$, wavevector $\vec{k}$, angular frequency ω, amplitude $\vec{A}_0 \in \Re$ and phase φ, which may be time-dependent in general. Expressions for the electric and magnetic fields can be found from Eqns. (2.4) and (2.5):

$$\vec{E} = \Re\left(-\mathrm{i}\omega \vec{A}_0 \mathrm{e}^{\mathrm{i}\left(\vec{k}\cdot\vec{x} - \omega t + \varphi\right)}\right), \tag{2.13}$$

$$\vec{B} = \Re\left(\mathrm{i}\left(\vec{k} \times \vec{A}_0\right) \mathrm{e}^{\mathrm{i}\left(\vec{k}\cdot\vec{x} - \omega t + \varphi\right)}\right), \tag{2.14}$$

where the real component is chosen to represent the physical fields and the imaginary components encodes the complex phase. $\vec{E}$ must be divergence-free in vacuum, so

$$-\mathrm{i}\mathrm{e}^{\mathrm{i}\left(\vec{k}\cdot\vec{x} - \omega t + \varphi\right)}\left(\vec{k} \cdot \vec{A}_0\right) = 0, \tag{2.15}$$

and $\vec{B}$ is always divergence-free, hence

$$\vec{k} \cdot \vec{A}_0 = 0. \tag{2.16}$$

Eqn. (2.13) shows that $\vec{E}$ is parallel to $\vec{A}$ and Eqn. (2.14) shows that $\vec{B}$ is perpendicular to $\vec{A}$, $\vec{E}$ and $\vec{k}$. Thus, for a plane wave in vacuum, the electric field also oscillates perpendicular to $\vec{k}$.

2.1.2 Gaussian laser pulses

Whilst the plane wave description of light is useful in that it allows for exact solutions to many physically-relevant problems (for example, the motion of a charged particle interacting with an electromagnetic wave), it is usually not a sufficient descriptor of laser radiation because of their finite extent in space and time.

Laser beams are well modelled with Gaussian spatial and temporal intensity profiles [37]. Resonant transverse (spatial) modes in solid-state laser cavities are usually Gaussian. Longitudinal (temporal) modes are often described using hyperbolic secant functions. However, a Gaussian approximation is usually sufficient. A Gaussian beam with only fundamental mode components propagating in the x-direction with radial (r) symmetry has an electric field given by

$$\vec{E}\,(x, r, t) = E_0 \Re\left(\mathrm{e}^{\mathrm{i}(\omega_0 t - k_0 x + \varphi(t) + \psi(x))}\right) \mathrm{e}^{-\frac{r^2}{w^2}} \mathrm{e}^{-\frac{(t-x/c)^2}{\sigma_t^2}}, \tag{2.17}$$

where ω_0 is the central angular frequency corresponding to wavenumber $k_0 = \omega_0/c$, w is the beam radius[2], σ_t is the 1/e half-duration of the pulse, which is related to the full-width at half-maximum (FWHM) duration by $\tau = \sqrt{2\ln(2)}\sigma_t$, and $\psi\,(x)$ is the Gouy phase.

The Poynting vector, $\vec{S} = \vec{E} \times \vec{B}$, describes the energy flow of the wave and is used to define the intensity,

$$I(\vec{x}, r, t) = c\varepsilon_0 \left|\vec{E}(\vec{x}, r, t)\right|^2. \tag{2.18}$$

[2] Defined as the radial position at which the wave amplitude envelope falls to 1/e of its maximum value, which is also where intensity is 1/e^2 of its maximum.

The peak intensity is $I_{\text{peak}} = c\varepsilon_0 E_0^2$. Perhaps confusingly, 'intensity' is also often used to describe the cycle-averaged Poynting flux[3],

$$I_{\text{RMS}} = \left\langle \left| \vec{S} \right| \right\rangle_T = \kappa I_{\text{peak}}, \tag{2.19}$$

where

$$\kappa = \begin{cases} \frac{1}{2} & \text{for linear polarisation} \\ 1 & \text{for circular polarisation} \end{cases}. \tag{2.20}$$

A laser pulse with finite bandwidth (and therefore finite duration) can exhibit a frequency chirp, which can be described as a second order phase term

$$\varphi\,(x, t) = \frac{\alpha (t - x/c)^2}{2}, \tag{2.21}$$

for a given chirp rate α.

It is useful to define the normalised vector potential

$$a_0 = \frac{eE_0}{m_e \omega_0 c}, \tag{2.22}$$

where e is the elementary charge and m_e the rest mass of an electron, which leads to the convenient numerical approximation:

$$a_0 \approx 0.855\lambda\,[\mu\text{m}]\,\sqrt{I_0\,\left[10^{18}\,\text{W}\,\text{cm}^{-2}\right]}. \tag{2.23}$$

a_0 is dimensionless and corresponds to the momentum (normalised to $m_e c$) of an electron oscillating in the laser field. Therefore, a laser with $a_0 \gtrsim 1$ is said to be relativistic, and non-relativistic otherwise.

During propagation of a Gaussian beam, the radius evolves as

$$w(x) = w_0 \sqrt{1 + \left(\frac{x}{x_R}\right)^2}, \tag{2.24}$$

[3] Unless otherwise specified, all proceeding references to 'intensity' will refer to the RMS value. The peak RMS intensity will be designated I_0.

where w_0 is the minimal beam radius at focus, called the waist, at which the intensity is largest, and $x_R = \pi w_0^2/\lambda$ is the Rayleigh range (the distance from the waist to the point where $w(z) = \sqrt{2}w_0$). The far field divergence half-angle is given by [38]

$$\theta = \frac{\lambda}{\pi w_0}. \tag{2.25}$$

In this paraxial approximation, the focus is considered a point source and

$$\theta \approx \frac{D}{2f}, \tag{2.26}$$

where D is the diameter of the beam in the far field and f is the focal length of a focusing optic. Equating Eqns. (2.25) and (2.26) gives

$$w_0 = \frac{2\lambda f}{\pi D}. \tag{2.27}$$

The above concepts are summarised in Fig. 2.1.

2.1.3 High-power, short-pulse lasers

The technique of chirped-pulse amplification (CPA), a concept that originates in radar technology, was first applied to lasers by D. Strickland and G. Mourou in the mid-1980s [1]. It employs optical stretching and compression methods developed by E. Treacy [39] and O. E. Martinez *et al.* [40] to reduce the power of laser pulses undergoing amplification, thus avoiding self-focusing of the beam and subsequent damage to gain media and allowing greater final pulse energies to be obtained. The steps involved in CPA are outlined below:

1. A low-energy ($\sim$nJ), ultrashort-duration ($\lesssim 1\,\mathrm{ps}$) pulse is generated in a mode-locked laser cavity (or 'oscillator').

2. Using dispersive optics (such as gratings), the pulse duration is lengthened by introducing a frequency chirp, which reduces the peak power by several orders of magnitude.

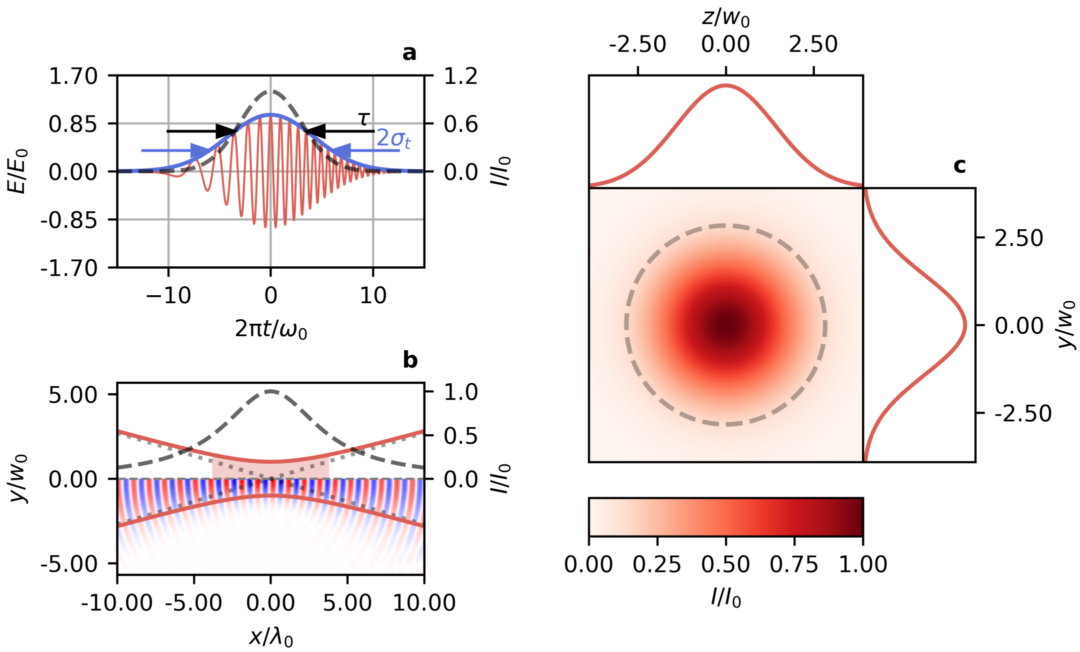

Figure 2.1: **a**, The temporal profile of a Gaussian laser pulse with positive frequency chirp, showing the electric field (thin solid red) and field envelope (thick solid blue) and corresponding intensity (dashed black). **b**, A Gaussian beam propagating through focus. Red solid lines show the beam radius, grey dashed lines the local peak intensity, red-blue colour scale the electric fields (which are symmetric about $y = 0$) and grey dotted lines the far field approximation. The Rayleigh range is shaded red. **c**, The transverse spatial intensity profile of a Gaussian pulse. The upper- and side-panels show horizontal and vertical lineouts through the centre of the beam, respectively. The dashed circle indicates the beam circumference.

3. The pulse is then amplified by a factor of $10^6 - 10^9$. The long duration of the stretched pulse ensures that the peak power remains below the damage threshold of the amplifying devices. The sizes of optical components are often limited due to practicality and technology.

4. Finally, the pulse is compressed to a similar duration to what it was originally by another set of dispersive optics configured to counter the effect of those in step 1.

CPA is shown schematically in Fig. 2.2.

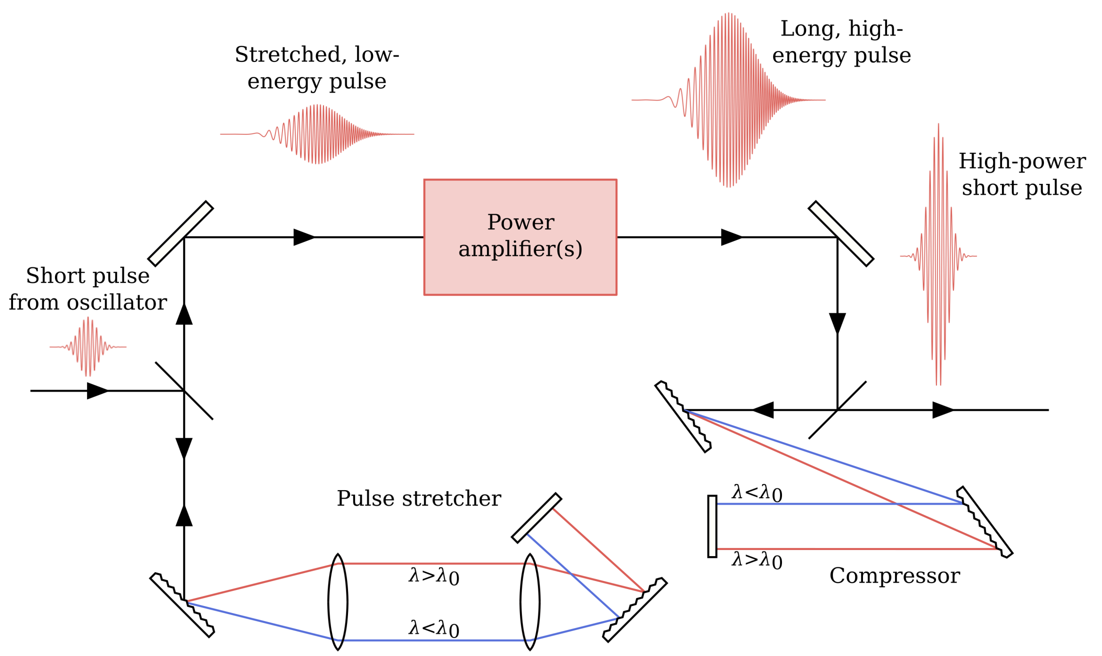

Figure 2.2: Schematic representation of chirped pulse amplification.

Examples of lasing media and their corresponding typical central gain wavelength values are Ti:sapphire (800 nm), Nd:glass (1.06 µm) and Cr:LiSAF (900 nm). These materials are used because of their desirable properties for generating ultrashort pulses with high peak power at reasonable repetition rates and system sizes.

Ti:sapphire, developed by P. F. Moulton in the 1980s [41], is by far the most commonly used laser material for multi-TW and PW-class lasers, and therefore most relevant to this thesis. CPA using a Ti:sapphire crystal was first demonstrated by D. E. Spence *et al.* in 1991 [42]. Its very high energy density (up to $\sim$1 J cm^{-2}) makes it suitable for high-energy amplification, although Kerr-lens modelocking had to be developed to enable the use of the crystal [43]. Ti:sapphire also has a high optical damage threshold ($\sim$10 J cm^{-2}) and high thermal conductivity (46 W mK^{-1} at room temperature), allowing for compact, high repetition rate systems. Frequency doubled YAG lasers can efficiently pump the crystal, which absorbs strongly at 500 nm with a bandwidth around 100 nm.

During amplification of a high power laser pulse, the spectrum can be modified due to frequency dependence of the gain curve. This leads to gain narrowing [44, 45] and lengthening of the pulse after compression. Gain depletion can also occur when the pulse reaches a high enough power during amplification for the head of the pulse to deplete the energy stored in the laser crystal, inhibiting amplification of the tail and thus distorting the pulse in the time and frequency domains [3]. The final pulse duration is further limited by high-order dispersion [46–49]. Several techniques and design considerations exist to minimise high-order dispersion. The choice of grating separation and beam angle-of-incidence on each grating as well as careful alignment of optical devices in all stages can mitigate second- and third-order dispersion. Fourth-order dispersion can be compensated by introducing prescribed quantities of optical material [50]. The spectral phase and amplitude can be modified using an acousto-optic programmable dispersive filter [51, 52].

Incremental advances in technology and the availability of significant funding, driven by breakthroughs in scientific understanding and application development, have led to a continuous increase in the peak power of state-of-the-art laser systems. National scale facilities such as the Extreme Light Infrastructure (ELI) [53–56], Apollon [57] and the Shanghai Superintense Ultrafast Laser Facility (SULF) [58] now operate in the 10 PW regime. The BELLA laser [59] has a repetition rate up to 1 Hz with a peak power of 1.3 PW, VEGA-3 at the Centro de Láseres Pulsados (CLPU) [60] offers the same repetition rate at 1 PW. The Texas Petawatt Laser delivers 186 J in 167 fs [61]. The Central Laser facility at the Rutherford Appleton Laboratory hosts a dual-arm high-power, short-pulse laser system with two independent 500 TW beams [62]. Regional and institutional facilities host PW-class lasers, such as the Scottish Centre for the

Application of Plasma-based Accelerators (SCAPA) [63,64], which can deliver 350 TW pulses at up to 5 Hz. For a recent review of the development of petawatt and exawatt class laser facilities, see Ref. [65].

2.2 Light-matter interactions

Having introduced a framework for describing propagation of light, its interaction with matter is now discussed. The different regimes of photoionisation are described, which plays two important roles in this thesis – it is the primary method of plasma creation considered in these studies, and it can significantly affect the scattering processes when two or more intense laser pulses intersect in gas (discussed in later chapters). The analytic dynamics of a single charged particle interacting with an infinite electromagnetic plane wave are described, and the ponderomotive force that arises during interaction with an inhomogeneous field is discussed.

2.2.1 Photoionisation

In the context of the present work, most matter encountered by a laser in a laboratory environment is initially in a gaseous state. For high laser intensities, the first interesting process that occurs during the interaction is photoionisation. Thus, the interaction of light with atoms represents a reasonable starting point for a discussion of the interaction of laser beams with matter.

Einstein's theory of the photoelectric effect [66] described early experimental observations that the energy of a light quanta impinging on a material, W_γ, must surpass an energy threshold, W_{bind}, to liberate an electron from the surface,

$$W_\gamma = \hbar\omega > W_{\mathrm{bind}}, \tag{2.28}$$

where the subscript γ denotes properties of a photon (see Fig. 2.3**a**) and $\hbar$ is equal to Planck's constant divided by 2π. This revelation contradicts the classical description of light, which predicts that a continuous stream of light will eventually liberate even the most tightly-bound electron.

Multiphoton ionisation

With increasing laser intensity comes a greater rate of ionisation. This photoionisation occurs with incident photons that do not satisfy Eqn. (2.28), but may be rectified with the quantum theory of light by considering the probability that a bound electron may virtually absorb the energy of multiple low-energy photons before it can radiate the energy from its excited state by the process of multiphoton ionisation (MPI, see Fig. 2.3**b**). The probability of transition from a bound (b) to free (f) state by absorption of N photons can be calculated using lowest-order perturbation theory (LOPT), and is given by [67]

$$\Gamma^{(N)}_{b\to f} = \hat{\sigma}_N I^N, \tag{2.29}$$

for cross-section $\hat{\sigma}_N$. For infrared photons from a Ti:sapphire laser, measurable quantities of MPI-generated electrons are produced when $I \gtrsim 10^9\,\mathrm{W\,cm^{-2}}$. Laser-induced MPI was first demonstrated in negative iodine ions in 1965 using a ruby laser focused to an intensity $2 \times 10^9\,\mathrm{cm^{-3}}$ [68], and in noble gases in the 1960s [69, 70].

At yet higher intensities the photoelectron may absorb the energy of surplus (S) photons whilst still under the influence of the atomic Coulomb potential, by the process of above-threshold ionisation (ATI, see Fig. 2.3**c**) [71–73]. Such an electron is born with energy [74]

$$W_f = (N + S)\,\hbar\omega - W_{\mathrm{bind}}. \tag{2.30}$$

Eqn. (2.30) is again calculated by LOPT, but later experiments revealed suppression of ATI peaks in the photoelectron energy spectrum, suggesting that higher-order effects such as Stark shifting of the bound energy states must be accounted for, and that ATI is therefore non-perturbative [75–77]. The expression for the final electron energy is still valid as the quiver energy imparted to the bound electron, which diminishes the free electron energy, is exactly compensated by the energy picked up by the recently-liberated particle as it is accelerated by the ponderomotive potential [78].[4]

[4]See Sec. 2.2.3 for a discussion of the ponderomotive force.

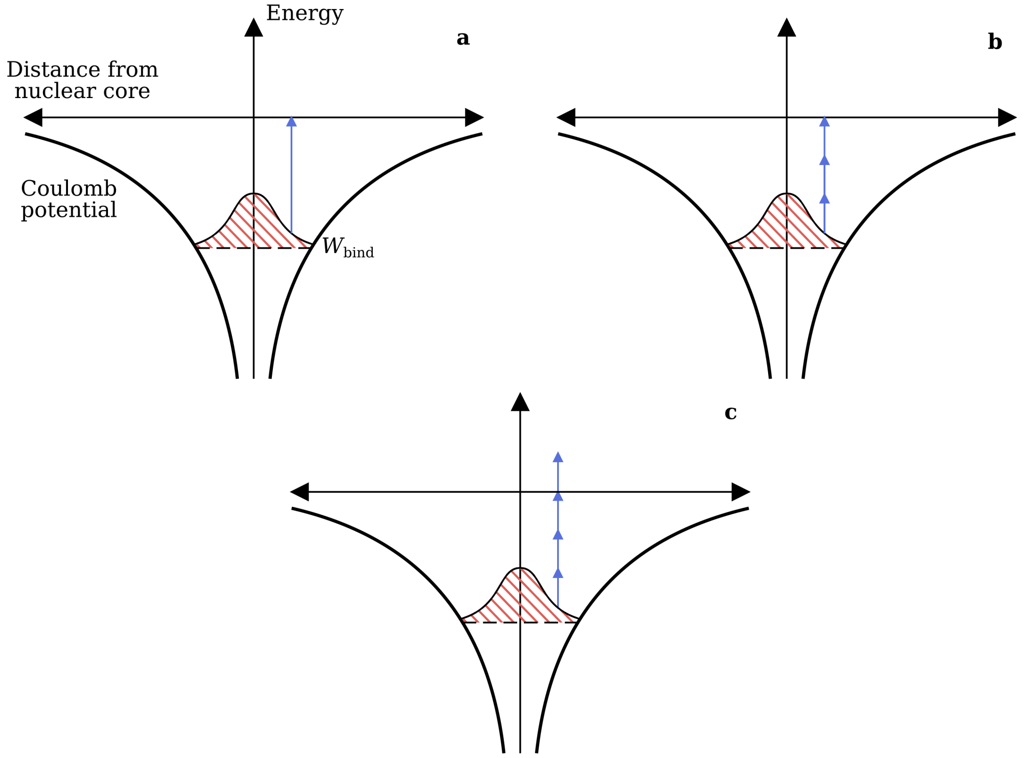

Figure 2.3: Representation of **a**, single- and **b**, multi-photon ionisation and **c**, above threshold ionisation.

Barrier suppression ionisation

In the presence of strong external fields, the Coulomb potential binding the electron to the atomic nucleus may be suppressed. The electron then has a finite probability of occupying an unbound state through the process of quantum tunnelling [79]. Further increasing the field strength leads to suppression of the Coulomb potential beyond the binding energy, at which point the electron is classically unbound and occupies a state in the continuum. These scenarios, called barrier suppression ionisation (BSI) or tunnel ionisation and over-the-barrier ionisation (OTBI), respectively, are shown schematically in Fig. 2.4**a** and **b**.

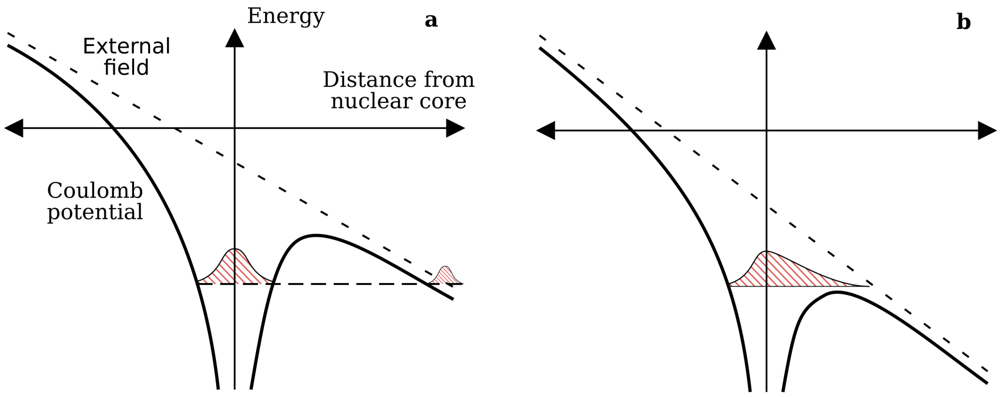

Figure 2.4: Representation of **a**, tunnel and **b**, over-the-barrier ionisation.

Evaluating the Coulomb potential at the Bohr radius allows for the determination of the atomic intensity [80], which for hydrogen is $I_a \simeq 3.51 \times 10^{16}\,\mathrm{W\,cm^{-2}}$. Due to barrier suppression, significant ionisation occurs at intensities much below this. To demonstrate this, consider the threshold of OTBI established by a static external potential, $F = eE_F r$ [81]. The electric potential a distance r from the atomic core is given by

$$V(r) = -\frac{Ze^2}{r} - F(r), \tag{2.31}$$

for atomic number Z. By setting $V'(r) = 0$ and $V = W_{\mathrm{bind}}$, the critical electric field, beyond which OTBI occurs, is found to be

$$E_c = \frac{W_{\text{bind}}^2}{4Ze^3}, \tag{2.32}$$

from which a critical intensity can be derived as

$$I_c = \frac{cW_{\text{bind}}^4}{128\pi Z^2 e^6}. \tag{2.33}$$

For hydrogen, $I_c \simeq 1.4 \times 10^{14}\,\mathrm{W\,cm^{-2}}$, which is several orders of magnitude below that readily achievable using modern laser systems.

Calculating the exact ionisation rate due to tunnelling in BSI requires integration of the Schrödinger equation. In general, for complex atomic configurations, this constitutes an enormous set of partial differential equations. Numerical solutions can be found in many cases but require huge computational resources. A powerful approximation that allows for accurate determination of the tunnelling ionisation rate of single- and multi-electron atoms or ions in arbitrary states, driven by alternating fields with arbitrary polarisation, was derived by M. V. Ammosov *et al.* [82][5] and verified experimentally at intensities in the range 10^{13}–$10^{18}\,\mathrm{W\,cm^{-2}}$ by T. Auguste *et al.* [83].

Separation of photoionisation regimes

The regimes of MPI and BSI are clearly not distinct. Ionisation of atoms subjected to intermediate field strengths will be due to a combination of MPI and BSI. Despite this, L. V. Keldysh was able to determine an adiabaticity parameter (now commonly called the Keldysh parameter) [79]

$$\gamma = \omega \left(\frac{2\,|W_{\text{bind}}|}{I} \right), \tag{2.34}$$

which distinguishes the limiting cases and is valid for $I \ll I_a$ and $\omega \ll \omega_a$, where $\omega_a = |W_{\text{bind}}|\,/\hbar$. A laser field is said to be "strong" if $\gamma \ll 1$ and "weak" if $\gamma \gg 1$. The ionisation rate induced by a strong laser field will be dominated by contributions from the BSI mechanism, while a weak laser field will predominantly induce MPI.

[5]Known as the ADK model.

In the discussion above, a static field has been assumed. By contrast, the fields of a laser are oscillatory and the instantaneous ionisation rate will therefore vary between extrema. Ionisation is most likely to occur when the fields are maximal and none can take place as the field changes direction.

2.2.2 Charged particle interaction with an infinite plane wave

While this thesis primarily deals with the interaction of spatially and temporally varying laser fields with a large number of particles, it is nevertheless instructive to consider the interaction of a single charged particle with an infinite electromagnetic plane wave. The motion of a charged particle in an electromagnetic field is governed by the Lorentz equation [84]

$$\vec{F} = \frac{\mathrm{d}\vec{p}}{\mathrm{d}t} = q\left(\vec{E} + \vec{v} \times \vec{B}\right), \tag{2.35}$$

for charge q, velocity $\vec{v}$ and momentum $\vec{p}$. The non-relativistic equations of motion for a particle experiencing a sinusoidally oscillating electromagnetic wave are then

$$\begin{aligned} F_x &= qv_y \mathrm{i}kA_0\mathrm{e}^{\mathrm{i}(kx-\omega t+\varphi)} && \text{(2.36a)} \\ F_y &= -\mathrm{i}q\omega A_0\mathrm{e}^{\mathrm{i}(kx-\omega t+\varphi)} - v_x\mathrm{i}kA_0\mathrm{e}^{i(kx-\omega t+\varphi)} \\ &= -\mathrm{i}qA_0\mathrm{e}^{\mathrm{i}(kx-\omega t+\varphi)}\left(\omega + v_x k\right) && \text{(2.36b)} \\ F_z &= 0 && \text{(2.36c)} \end{aligned}$$

where subscripts x, y and z denote quantities in the respective vector directions. The instantaneous velocity of the particle, called the quiver velocity, is maximal at the trough of the electric field oscillation

$$\max\left(v_q\right) = \frac{qE_0}{m\omega}. \tag{2.37}$$

By normalising Eqn. (2.37) to c and taking $m = m_e$, the mass of an electron, we re-obtain Eqn. (2.22), the normalised vector potential.

In vacuum, the dispersion relation is

$$\omega = ck, \tag{2.38}$$

so the equations of motion can be written as

$$\begin{aligned} v_x &= \frac{1}{m}\int F_x \,\mathrm{d}t \\ &= \frac{-qA_0}{mc}\mathrm{e}^{\mathrm{i}(kx-\omega t+\varphi)}\left(\frac{q}{2m}\mathrm{e}^{\mathrm{i}(kx-\omega t+\varphi)} + v_{y,0}\right) + v_{x,0} \qquad (2.39\mathrm{a}) \\ v_y &= \frac{1}{m}\int F_y \,\mathrm{d}t \\ &= \frac{q}{m}A_0\mathrm{e}^{\mathrm{i}(kx-\omega t+\varphi)} + v_{y,0} \qquad (2.39\mathrm{b}) \\ v_z &= v_{z,0} \qquad (2.39\mathrm{c}) \end{aligned}$$

where the v_x term in Eqn. (2.36b) has been neglected under the assumption that $v_x \ll c$ to arrive at Eqn. (2.39b), and the subscript 0 represents an initial value.

The intensity of 800 nm light required to exceed the relativistic threshold $a_0 \gtrsim 1$ is $I \approx 2\times 10^{18}\,\mathrm{W\,cm^{-2}}$, which is several orders of magnitude below what is readily achievable today. Relativistic effects are therefore very important for this thesis and may be resolved by taking $\vec{p} = \gamma m\vec{v}$, where $\gamma = \left(1 - |v|^2/c^2\right)^{1/2}$ is the Lorentz factor, and no longer neglecting momentum contributions from a crossed magnetic field. For rigorous derivations of the relativistic equations of motion in various gauges and coordinate frames, see Refs. [85–90]. The trajectory of an electron interacting with a linearly polarised wave in the lab frame is given by

$$y(\tau) = \frac{ca_0}{\omega}\sin(\omega\tau) \tag{2.40}$$

$$x(\tau) = \frac{ca_0^2}{4}\left(\tau + \frac{1}{2\omega}\sin(2\omega\tau)\right), \tag{2.41}$$

where $\tau = t - \frac{x(t)}{c}$ (for which $\mathrm{d}\tau = \mathrm{d}t/\gamma$). The electron oscillates in the rapidly-alternating fields of the laser, but also with a drift velocity

$$\frac{v_d}{c} = \frac{a_0^2}{a_0^2 + 4}, \tag{2.42}$$

which corresponds to the average velocity over a laser cycle. Trajectories in the laboratory and drift frames are shown in Fig. 2.5**a** and **b**, respectively. Motion in the longitudinal direction increases with increasing a_0. In the drift frame, the electron exhibits a characteristic 'figure-of-eight' motion.

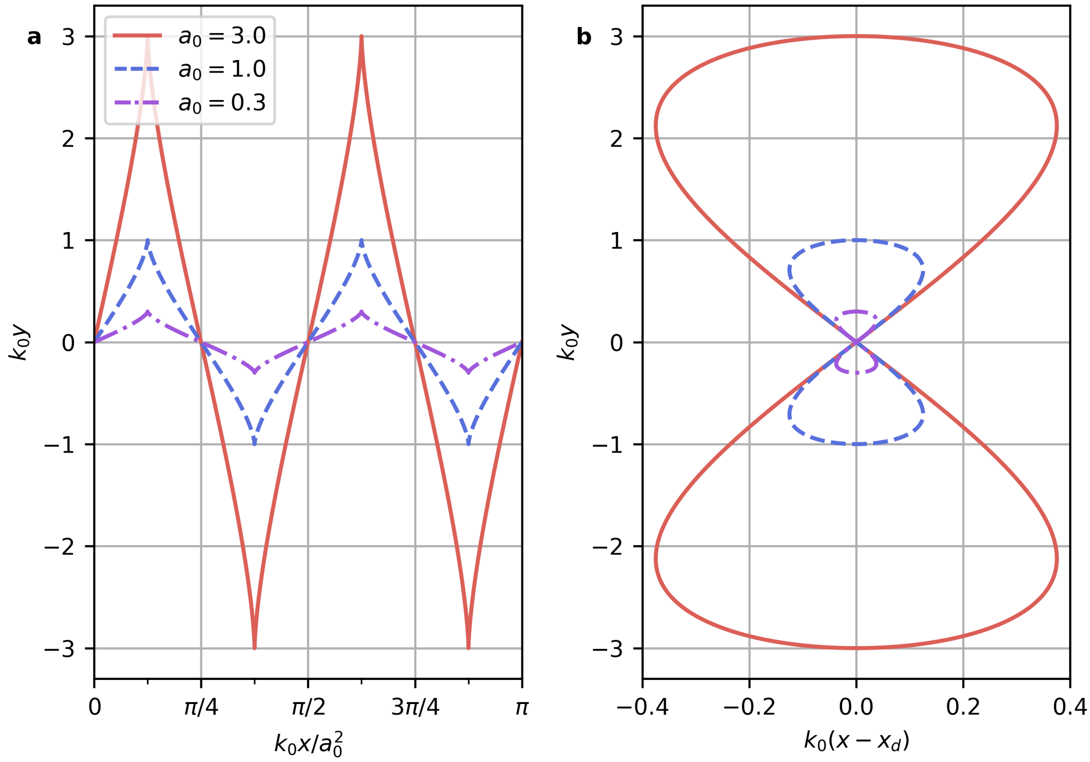

Figure 2.5: Trajectories in **a**, the lab frame and **b**, the drift frame of an electron oscillating in an electromagnetic plane wave with $a_0 = 3.0$ (solid, red), 1.0 (dashed, blue) and 0.3 (dot-dashed, purple).

2.2.3 The ponderomotive force

In the above, the central assumptions are that

1. the electromagnetic wave is planar, and

2. its temporal envelope is non-evolving.

This model is helpful for elucidating key concepts, but is clearly inappropriate for high-power laser pulses focused to small spots (see Fig. 2.1**b** and **c**). A useful approximation in this regime involves considering the spatial profile of the fields to be inhomogeneous, whilst averaging over the fast oscillations of the field and maintaining assumption 2. This gives rise to the "ponderomotive force", which presents as a potential with gradient between high- and low-field areas [91–95].

The force may be calculated using perturbation theory [96], and the non-relativistic expression is

$$\vec{F_p} = -\frac{q^2}{4m\omega^2}\nabla E^2. \tag{2.43}$$

A derivation of the relativistic generalisation presented in Ref. [80] begins by rewriting Eqn. (2.35) in terms of $\vec{A}$ and isolating contributions to the particle motion due to the (comparatively) fast oscillation of the field and the slow variation of the envelope, which results in

$$\vec{F_p} = -mc^2\nabla\bar{\gamma}, \tag{2.44}$$

where

$$\bar{\gamma} = \sqrt{1 + \frac{p_{\text{slow}}^2}{m^2c^2} + \bar{a_y^2}}, \tag{2.45}$$

and p_{slow} is the momentum imparted due to the slowly-varying envelope. This treatment arrives at analogous results to those derived using more thorough formulations [97, 98]. The direction of $\vec{F_p}$ is independent of the sign of the charge and points from regions of high to low intensity. For a Gaussian field envelope, charged particles are displaced most strongly from the laser axis.

2.3 Laser-plasma interactions

The core concepts upon which the studies in this thesis are built are now discussed. A brief description of plasma is given and the formation of plasma waves is established, which is linked to the propagation of light through plasma. The laser wakefield acceleration scheme, which can be used to accelerate electrons to relativistic momenta, is introduced, and an overview of the popular method of particle-in-cell simulation is given.

2.3.1 General description of plasma

Often described as the 'fourth state of matter', plasma is the most common form of ordinary[6] matter in the observable universe. An intuitive definition is 'a gas of charged particles', although this does not account for the behaviour that vastly distinguishes plasma from more familiar states of matter. Despite different plasmas spanning several orders of magnitude of density, time, temperature and magnetic field strengths, they can always be characterised by quasineutrality and collective behaviour [99]. The latter is due to the long-range action of the Coulomb force, $F \propto r^{-2}$ for distance r, which allows local regions of plasma to influence those further afield.

Quasineutrality can be understood through the concept of Debye shielding [100]. Consider an arbitrary ball of immobile positive charge placed in a plasma. The plasma electrons will be attracted to the foreign charge and quickly form a 'sheath' surrounding it. At some distance from the edge of the ball, the shielded Coulomb potential will be equal to $k_B T_e$, the thermal energy of the electrons, where k_B is the Boltzmann constant. Beyond this distance, electrons have enough energy to surpass the Coulomb potential and thus electric fields can 'leak' into the plasma. By assuming the ions are stationary due to their inertia and the electron number density follows a Boltzmann distribution

$$n = n_0 \exp\left(\frac{e\phi}{k_B T_e}\right), \tag{2.46}$$

where n_0 is the unperturbed density, then Poisson's equation,

$$\varepsilon_0 \nabla^2 \phi = -e\left(n_i - n_e\right), \tag{2.47}$$

may be linearised to find

$$\lambda_D = \left(\frac{\varepsilon_0 k_B T_e}{n e^2}\right), \tag{2.48}$$

[6]Excluding dark matter and energy.

which is called the Debye length, where $n \simeq n_i \simeq n_e$ is the plasma density in the bulk of the plasma. For cold plasma (where $T_e = 0$), the sheath has no thickness. λ_D also decreases with increasing n as there are more electrons available in a given volume to shield the foreign charge. If the characteristic scale length of a gas composed of charged particles is greater than λ_D, any fields associated with local charge fluctuations will be shielded out and the rest of the plasma will have $n_i \simeq n_e$, i.e. the gas will be quasineutral.

2.3.2 Waves in plasma

Plasma supports numerous types of waves. This section focuses on the two modes most relevant to this thesis: light waves and Langmuir waves.

Light waves

The dispersion relation for an electromagnetic wave propagating in a cold, unmagnetised plasma with $\vec{E}$ transverse to $\vec{k}$, assuming immobile ions, a nonrelativistic electron response and negligible contribution by the magnetic field to the electron motion, is

$$\omega^2 = \omega_p^2 + k^2c^2, \tag{2.49}$$

where k here is the wavevector of the radiation and ω_p is the plasma frequency (derived in the following section). We identify a critical plasma density, n_c, at which $\omega_p = \omega$ and only evanescent wave solutions exist. A plasma with $n < n_c$ ($\omega > \omega_p$) is called underdense and the converse is called overdense. Physically, an electromagnetic wave interacting with overdense plasma excites electron oscillations that are strongly damped by the restoring force due to the ensuing charge separation and re-radiate fields that are π out of phase with the incident radiation. Electromagnetic fields are therefore not free to propagate within overdense materials.

The group and phase velocities in an underdense plasma are given by

$$v_g = \frac{\mathrm{d}\omega}{\mathrm{d}k} = c\left(1 - \frac{\omega_p^2}{\omega^2}\right)^{\frac{1}{2}} \tag{2.50}$$

$$v_p = \frac{\omega}{k} = c\left(1 - \frac{\omega_p^2}{\omega^2}\right)^{-\frac{1}{2}}. \tag{2.51}$$

The phase of the wave propagates faster than the speed of light in vacuum, while the group velocity is less than c, which is consistent with the limit on the speed of information transfer imposed by special relativity.

Langmuir waves and wakefields

Consider a plasma in which a group of electrons have been perturbed from their equilibrium position. This results in electric fields that act to restore the particle positions. Assuming an immobile background of ions, the electrons will be accelerated to their original position and, neglecting any collisions, will overshoot. This process repeats at the characteristic plasma frequency, ω_p. To determine this frequency, we require the Lorentz equation,

$$m_e n_e\left(\frac{\partial \vec{v_e}}{\partial t} + (\vec{v_e}\cdot\nabla)\,\vec{v_e}\right) = -en_e\vec{E}, \tag{2.52}$$

which gives the force on the perturbed electrons travelling with velocity v due to the resulting electric field $\vec{E}$, and the continuity equation

$$\frac{\partial n_e}{\partial t} + \nabla\cdot(n_e\vec{v_e}) = 0, \tag{2.53}$$

which states that the number of electrons is invariant and is a consequence of the assumption that there is no recombination or further ionisation. By applying small perturbations

$$n_e = n_{e,0} + n_{e,1},\;\; \vec{v}_e = \vec{v}_{e,1},\;\; \vec{E} = \vec{E}_1 \tag{2.54}$$

to Eqns. (2.47) (and therefore Eqn. (2.4), with $A = 0$), (2.52) and (2.53), linearising and assuming sinusoidal oscillations with frequency ω, we arrive at

$$\omega = \omega_p = \left(\frac{n_0 e^2}{\varepsilon_0 m_e}\right)^{\frac{1}{2}}. \tag{2.55}$$

Intuitively, a higher plasma density results in a more rapid oscillation about the equilibrium because the greater number of ions contribute to a stronger restoring field.

In the case of plasma with electrons that have a finite temperature, the electron thermal pressure acts in addition to the displacement electric field to restore the electrons. Using a fluid model, a wave is found to propagate, known as the Langmuir wave, that obeys the Bohm-Gross dispersion relation [101, 102]

$$\omega^2 = \omega_p^2 + 3k^2 v_{e,th}^2, \tag{2.56}$$

where $v_{e,th}$ is the electron thermal velocity,

$$v_{e,th} = \left(\frac{k_B T}{m}\right). \tag{2.57}$$

The nonlinear response evident during high-power laser interaction with plasma, which is of interest to much of the work in this thesis, requires a relativistic treatment. A. I. Akhiezer & R. V. Polovin used the plasma fluid approximation to describe the nonlinear response of a cold plasma wave with large amplitude [103]. A. Decoster then determined that analytic solutions can only be found under certain conditions (e.g. in unmagnetised, highly underdense plasmas) [104]. Most pertinent to this thesis is the work of R. J. Noble, who restricted analysis to purely longitudinal plasma waves in underdense plasma [105], such as those driven by a laser pulse. A plasma wave excited by a driving laser pulse will propagate behind the laser with phase velocity equal to the group velocity of the pulse in the plasma. Following this, an often useful assumption is that the laser pulse is non-evolving, and therefore elicits a plasma response that does not vary in the frame of the moving laser [106, 107]. This is the quasistatic approximation, and is characterised by the variable $\xi = x - v_p t$. The governing formulae in this case are the Poisson equation and the plasma fluid equations [108–110]

$$\frac{\mathrm{d}^2\Phi}{\mathrm{d}\xi^2} = \frac{\gamma_p^2}{k_p^2}\left(\beta_p\left(1-\frac{\gamma_\perp^2}{\gamma_p^2P^2}\right)^{-\frac{1}{2}}-1\right), \tag{2.58}$$

$$\frac{n}{n_0} = \gamma_p^2\beta_p\left(\left(1-\frac{\gamma_\perp^2}{\gamma_p^2P^2}\right)^{-\frac{1}{2}}-\beta_p\right), \tag{2.59}$$

$$u_x = \gamma_p^2P\left(\beta_p-\left(1-\frac{\gamma_\perp^2}{\gamma_p^2P^2}\right)^{\frac{1}{2}}\right), \tag{2.60}$$

$$\gamma = \gamma_p^2P\left(1-\beta_p\left(1-\frac{\gamma_\perp^2}{\gamma_p^2P^2}\right)^{\frac{1}{2}}\right), \tag{2.61}$$

where $\Phi = e\phi/m_ec^2$ is the normalised electrostatic potential, $P = 1+\Phi$, $\gamma_\perp \simeq \sqrt{1+a^2}$ is the Lorentz factor associated with the quiver velocity in a linearly polarised laser field and $\beta_p = v_p/c$ is the normalised phase velocity of the plasma wave and therefore $\gamma_p = \left(1-\beta_p^2\right)^{-\frac{1}{2}}$. In the following sections, the driving laser pulse duration is restricted to $\lesssim \lambda_p/c$, where $\lambda_p = 2\pi c/\omega_p$ is the cold nonrelativistic plasma wavelength.

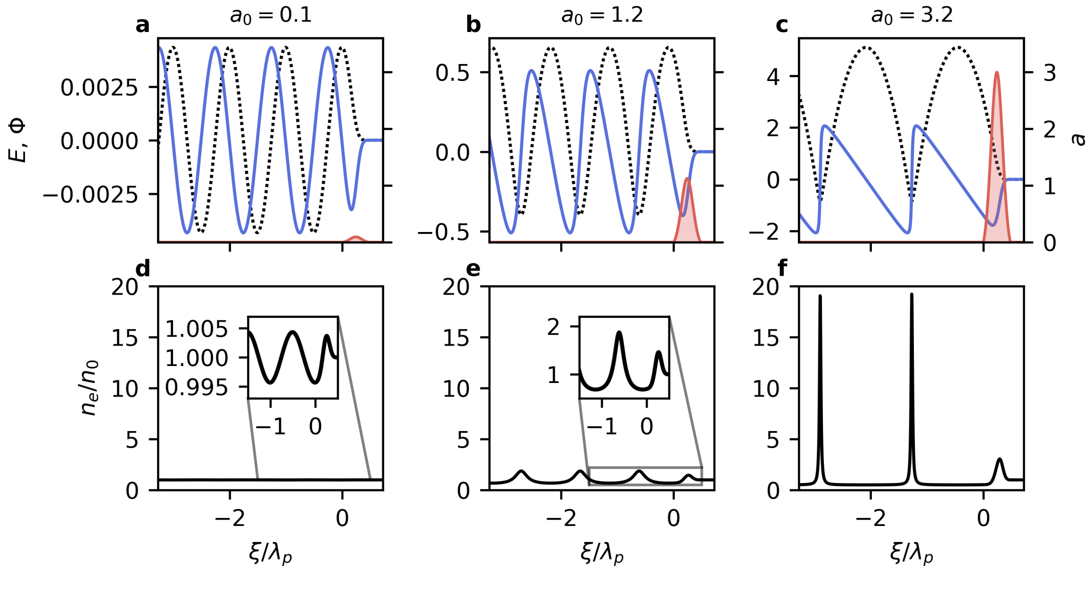

Figure 2.6: Wakefields and density perturbation due to a driving laser pulse with $a_0 = 0.1,\ 1.2,\ 3.2$, in the left, middle and right columns, respectively. **a-c**, Solutions to Eqn. (2.58) (dotted black) and their derivative, E (solid blue), driven by a quasi-Gaussian laser pulse (shaded red). **d-f**, Solutions to Eqn. (2.59).

The density perturbation and accompanying wakefields driven by a quasi-Gaussian laser pulse are shown in Fig. 2.6 for various values of a_0. The laser envelope is given by

$$a(\xi) = a_0 \mathrm{e}^{\frac{-4\ln(2)\xi^2}{\sigma_l^2} - \frac{1}{16}} \theta\left(\sigma_l - |\xi|\right), \tag{2.62}$$

where $\sigma_l = 10\lambda_l$ for laser wavelength λ_l has been used and θ is the Heaviside step function. The units of co-moving spatial coordinate are shown as multiples of λ_p. In the linear regime, the wakefields and plasma response are sinusoidal. By contrast, the electric fields driven by a relativistic laser pulse are more sawtooth and the plasma density perturbation exhibits characteristic spikes. The period of the waveform trailing the laser also increases with a_0 due to the relativistically enhanced inertia of the electrons. The near-depletion of electrons in each 'bucket' at very high a_0 is accompanied by large electric fields.

In the 1-dimensional linear regime, the plasma can support a maximum electric field $E_{\mathrm{CNWB}} = cm_e\omega_p/e$, where the subscript 'CNWB' indicates the cold nonrelativistic wavebreaking limit [111]. Beyond this limit, the fluid equations predict an electron number density approaching infinity and the wave is said to 'break'. Using the above relativistic equations (Eqns. (2.58)-(2.61)), the cold relativistic wavebreaking (CRWB) limit is found to be $E_{\mathrm{CRWB}} = \sqrt{2\left(\gamma_p - 1\right)}E_{\mathrm{CNWB}}$ [103].

2.3.3 Laser wakefield acceleration

In Sec. 2.3.2, the linear and nonlinear plasma wave response to a driving laser pulse was described. In their seminal 1979 paper, Tajima & Dawson proposed utilising the strong electric fields associated with the plasma wave to accelerate electrons [112], in a scheme now referred to as the laser wakefield accelerator (LWFA).

For a plasma with $n_0 = 1 \times 10^{19}\,\mathrm{cm}^{-3} \simeq 0.006 n_{c,800\,\mathrm{nm}}$, $E_{\mathrm{CNWB}} \simeq 300\,\mathrm{GV\,m}^{-1}$ and $E_{\mathrm{CRWB}} \simeq 1.5\,\mathrm{TV\,m}^{-1}$, which is 3 to 4 orders of magnitude greater than the largest accelerating fields in conventional[7] particle accelerator RF cavities [4]. Early experiments [113–120] corroborated these predictions, but it was not until 2004 that high-quality (high charge and energy, low energy spread and divergence) electron beams

[7]'Conventional' here refers to the methods of particle acceleration based on the highly mature RF accelerators.

were generated, the results of which were published in the 'Dream beam' edition of Nature that year [121–123]. This advancement followed the invention of chirped-pulse amplification laser systems [1], which led to terawatt, femtosecond lasers. These papers spurred a huge amount of interest, and significant progress in producing high-quality electron beams has since been made. Recent demonstrations include multi-GeV electron beams [124, 125], a kHz-repetition rate 15 MeV LWFA with low divergence [126], and 24-hour stable accelerator operation [127].

The high accelerating gradients of LWFAs makes them potentially attractive stages for a future compact linear e^+e^- collider [128–130]. The intrinsically ultrashort bunches are promising as drivers of fifth-generation light sources [131, 132]. The tight coupling of the high-energy electron beams and relativistic lasers make them ideal for the study of high-field QED effects [133]. In addition, LWFAs have potential application as secondary sources for use in a plethora of applied fields. Electron oscillations in the accelerator lead to synchrotron-like emission of spatially coherent X-rays [134–136], which are also bright [11] and ultrashort [6], and may extend to the γ range [137]. These X-rays can be used for phase contrast imaging of biological [138–140] and non-organic [12] specimens, for micro-computed tomography [13, 15, 141], or for probing warm dense matter via absorption spectroscopy [142, 143]. Colliding the accelerated electron bunches with high-Z targets produces γ-rays that can be used to probe dense matter [144, 145].

Electron acceleration in a nonlinear wake

In the 1D nonlinear fluid regime ($E_{\mathrm{max}} < E_{\mathrm{CRWB}}$), electrons with sufficient initial momentum[8] may be captured by the accelerating portion of a plasma wave bucket trailing the driving laser pulse. Once injected, they quickly gain significant energy. The plasma wave, however, travels with phase velocity approximately equal to the group velocity of the laser in the plasma, which is less than the speed of light. The electrons therefore outrun the plasma wave and eventually enter the decelerating portion of the wake bucket and 'dephase'.

[8]Particles with insufficient initial momentum simply slip backwards in the comoving frame.

For sufficiently high laser intensity, a 3D LWFA enters the 'bubble' regime, which is characterised by near-complete evacuation of the electrons from the region behind the laser and a string of ion cavities [146–148]. Electrons in a bucket experience strong accelerating and focusing fields. Nonlinear effects (discussed in Sec. 2.3.4) allow the driving laser to propagate stably over many Rayleigh lengths.

Fig. 2.7 shows a snapshot of a simulated[9] laser wakefield accelerator operating in the bubble regime, performed with FBPIC [10] [149], for a laser with initial laser amplitude $a_0 = 4$ and plasma density $n_0 = 1 \times 10^{18}\,\mathrm{cm}^{-3}$ (see Appx. C.1 for the simulation file). Electrons displaced by the driving laser form a sheath around the ion cavity and are strongly attracted back to the axis by the electric field of the bubble. Most displaced electrons go on to form subsequent buckets after either crossing or bouncing off the strong fields at the back of the bubble [150–153], and some are ejected at wide angles (10s degrees) with modest energies (up to $\sim$10 MeV) [154–157]. Under certain conditions (discussed later), a small number of electrons can become trapped in the bubble and accelerated to high energies [148, 158].

The bubble is approximately spherical and is efficiently formed when the laser waist is such that the displacing ponderomotive force at the laser waist is balanced by the restoring fields due to the ion cavity, giving $k_p w_0 \sim \sqrt{a_0}$, where $k_p = \omega_p/c$ is the plasma wavenumber. Through numerical simulation, W. Lu *et al.* [159, 160] found that a laser pulse is 'matched' to a plasma with constant density when $k_p w_0 \simeq 2\sqrt{a_0}$ and its pulse length is similar to the diameter. In this case, laser diffraction is balanced by relativistic self-focusing,[11] and the pulse is guided over many Rayleigh lengths.

Bunch injection

There are several mechanisms by which an electron may find itself with the necessary velocity to be trapped by the bubble fields and accelerate to high energies. The most conceptually trivial, but experimentally challenging, is external injection, which involves injecting a pre-accelerated electron beam into the wake at just the right phase

[9] For details of the simulation method, see Sec. 2.3.5.
[10] Fourier-Bessel Particle-in-Cell. See Sec. 2.3.5.
[11] See Sec. 2.3.4 for a discussion of relativistic effects governing laser pulse evolution in a plasma.

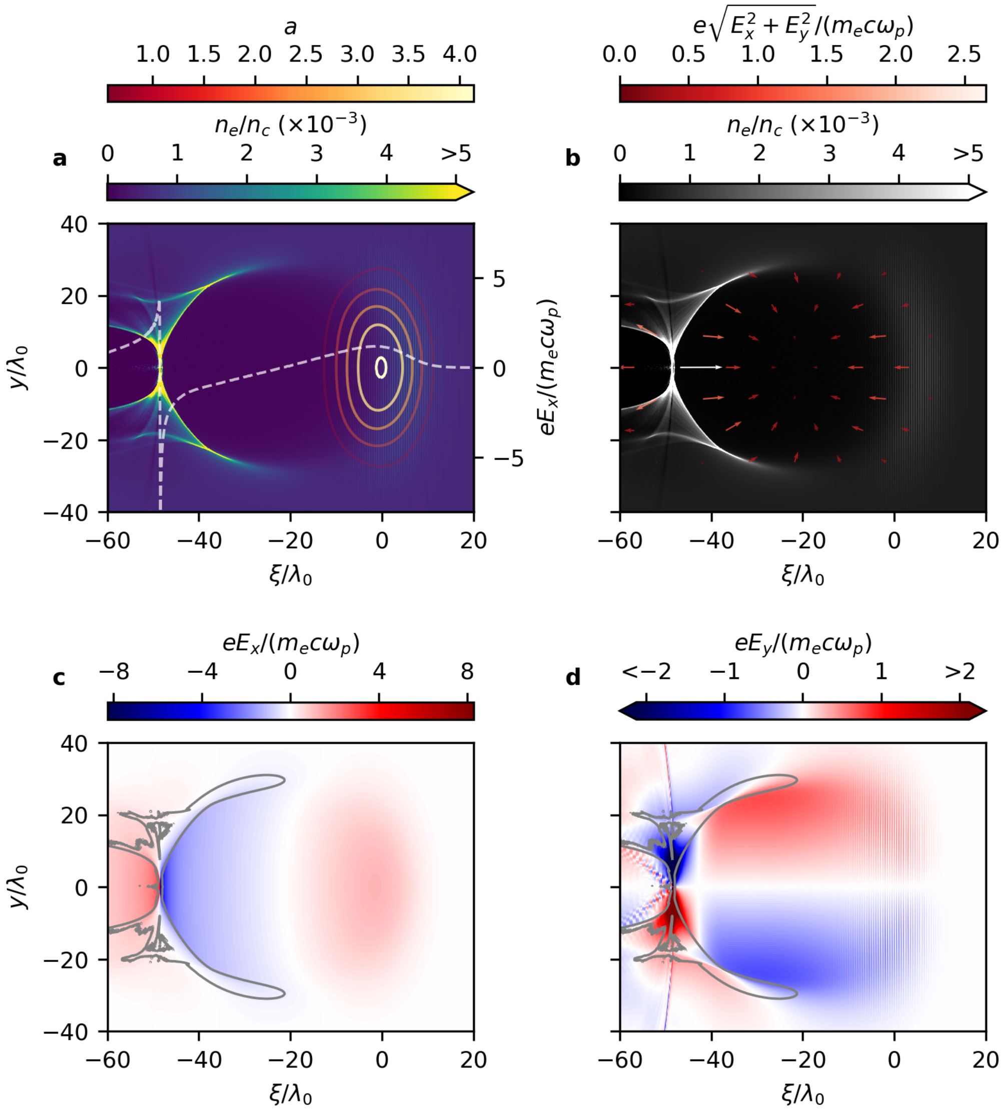

Figure 2.7: Snapshot of a quasi-3D FBPIC simulation of a laser wakefield accelerator operating in the bubble regime. **a**, A relativistic laser pulse (contours show isolines of field envelope strength) 'blows out' electrons (colour map) in the trailing wake, creating strong on-axis fields (dashed white) in the back half of the bubble. **b**, The $(E_x,\ Ey)$ vector field (arrows) shows the off-axis focusing fields. **c** & **d**, Regions of accelerating (**c**) and focusing (**d**) fields, shown with $n = 8\times10^{-4}n_c$ density isolines. Electric fields are given as multiples of the cold nonrelativistic wavebreaking limit, $E_{\mathrm{CNWB}} = 96.2\,\mathrm{GV\,m^{-1}}$ for the $n_0 = 1\times10^{18}\,\mathrm{cm^{-3}}(\approx 5.7\times10^{-4}n_c)$ used here.

for it to experience the accelerating fields [129,161,162]. Coupling the electron beam between stages is a major challenge and requires advanced beam transport devices [163] and laser optics [164]. A two-stage accelerator that used independent drivers and plasma targets was demonstrated by S. Steinke *et al.* [165].

The remaining injection methods involve sourcing the electrons from the background gas/plasma of the LWFA. Typical lasers used in LWFAs are focused to intensities many orders of magnitude greater than that required to fully ionise hydrogen. Depending on the intensity of the laser pulse, the more deeply bound electrons of higher-Z atoms (e.g. nitrogen, oxygen) may only be liberated towards the spatiotemporal centre of the pulse, where the fields are highest. By carefully choosing the target gas and laser profile and intensity, this phenomenon may be used to cause free electrons to be born in the accelerating portion of the wake and be efficiently trapped, by the process of ionisation injection [166–168]. Electrons can be continuously born in the wake in a homogenous gas target, resulting in beams with very high charge (nC-scale) and current (10s kA) but broad energy spectra as the fields due to the injected bunch distort the wake fields [169], although high-charge beams with monoenergetic features have also been demonstrated [170, 171].

Self-injection occurs when electrons enter the accelerating structure following breaking of the plasma wave. In the bubble regime, electrons may be injected when the bubble expands and encompasses electrons that would otherwise flow along the sheath, during its natural temporal evolution. The trajectory of electrons forming the sheath and within the bubble can be analysed using Hamiltonian dynamics [151,172–174]. An expansion of the bubble (triggering injection) followed by stabilisation or contraction is predicted to lead to the production of monoenergetic electron bunches in both the quasistatic [172] and ultrarelativistic [151] approximations, which are corroborated by simulations.

Optical techniques have been demonstrated that use 'injection' laser pulses to 'kick' electrons into the trapping fields. These are broadly divided into ponderomotive and colliding pulse mechanisms. In optical ponderomotive injection, the injection pulse propagates transversely to the driving pulse and interacts with the wake without overlapping with the driver. The injection pulse must have sufficiently large intensity for its ponderomotive force to accelerate electrons to the velocity of the wake, so they can be trapped [175–177]. The colliding pulse technique requires three laser pulses in total – one to drive the wake, and two to enable injection. All of the beams are collinear, which simplifies the experiments. The first injection pulse travels a non-overlapping distance behind the drive pulse. The second injection pulse has a frequency slightly detuned from the first injection pulse, travels counter to the other beams, and is made to collide with the first injection pulse. On collision, the ponderomotive force of the resulting slow beat wave pre-accelerates wake electrons to the velocity of the fast-moving wake [178]. A single injection pulse can also be made to beat slowly with the drive pulse and cause injection by a similar mechanism [179–182]. Both ponderomotive and colliding pulse injection allow for tuning of the injected charge and final energy and energy spread by controlling the intensity and delays of the injection pulse(s) [179,180].

The properties of the bubble can also be manipulated to enable injection. A plasma density down-ramp can cause longitudinal wavebreaking and injection [183–188]. Carefully tailored density profiles with a short (10s µm) density bump can cause the velocity of the back of the bubble to decrease very briefly, allowing the injection of 100 as-scale electron bunches [189]. Small-scale density perturbations produced in the gas targets typically used for LWFAs can be deleterious by the same mechanism, with many discrete injection events leading to significant dark current in the accelerator [190].

Acceleration and quality limits

Several processes exist that limit the maximum electron energy in a single-stage LWFA with homogeneous plasma density. The most obvious is related to the diffraction of the driving laser as it propagates. In the linear regime, the beam waist evolves in plasma in much the same way it evolves in vacuum, governed by Eqn. (2.24). At some point beyond the focal plane, the driver intensity will drop to such a low level that a useful wake is no longer generated and the accelerating fields drop substantially, halting particle acceleration. In the relativistic regime, nonlinear effects (discussed in Sec. 2.3.4) enable a high-intensity laser pulse to self-guide over multiple Rayleigh lengths. The laser pulse can also be externally guided by using a parabolic density profile [191], where the radial plasma density is given by

$$m(r) = n_0 \left(1 + \frac{r^2}{b^2}\right), \tag{2.63}$$

where n_0 is the on-axis plasma density and b is a channel depth parameter. For a constant plasma profile and assuming no radially-dependent energy change in the laser during the interaction, a Gaussian beam with matched waist $w_m = (b/k_p)^{1/2}$ can propagate in such a channel with constant spot size. A parabolic plasma density profile can be created by a Z-pinch [192], separate laser pulse [191,193–196], electric discharge [197–201], or combination of capillary discharge and axial heating laser pulse [202].

While displacing plasma electrons to form the accelerating wake structure, the driving laser pulse loses energy, which leads to pump depletion. The length over which this occurs for a 1-dimensional top hat pulse is [203, 204]

$$L_{\mathrm{pd}} = \frac{\lambda_p^3}{\lambda^2} \times \begin{cases} \frac{2}{a_0^2} & \text{for } a_0^2 \ll 1 \\ \frac{\sqrt{2}a_0}{\pi} & \text{for } a_0^2 \gg 1 \end{cases}. \tag{2.64}$$

After some time in the accelerator, electrons can reach velocities that exceed the group velocity of the driving laser pulse and begin to outrun the plasma wave. If the interaction continues for long enough, the electron bunch will dephase by entering the decelerating region of the wake, which reduces the final energy and the efficiency of the accelerator. For the same idealised 1-dimensional accelerator, the dephasing length for a bunch in the first bucket is given by [205]

$$L_{\mathrm{d}} = \begin{cases} \frac{\lambda_p^3}{2\lambda^2} & \text{for } a_0^2 \ll 1 \\ \frac{\lambda_p^3 \sqrt{2}a_0}{2\lambda^2} & \text{for } a_0^2 \gg 1 \end{cases}. \tag{2.65}$$

The pump depletion and dephasing lengths both have dependency $L \propto \omega_p^{-3}$, while $E_{\mathrm{CNWB}} \propto \omega_p$. To reach higher electron energies, it is therefore advantageous to reduce the plasma density, even though the magnitude of the accelerating fields will be lower. A longitudinally tapered plasma profile may be used to partially compensate for dephasing [206–213].

2.3.4 Laser pulse evolution in plasma

The refractive index of a plasma is

$$\eta = \frac{c}{v_p} = \sqrt{1 - \frac{\omega_p^2}{\omega^2}}. \tag{2.66}$$

Electrons oscillating in the large-amplitude fields of a high-intensity laser pulse acquire a cycle-averaged relativistic mass increase given by $m_e = m_{e,0}\sqrt{1 + a^2/2}$ for a linearly polarised pulse, where $m_{e,0}$ is the electron rest mass. This decreases the local plasma frequency, which is given by

$$\omega_p = \left(\frac{n_e e^2}{m_e \varepsilon_0}\right)^{1/2}, \tag{2.67}$$

and results in a higher refractive index and lower phase velocity. For a laser pulse with a radially decreasing a_0 (as is the case for a Gaussian beam), the axial refractive index will be lowest on axis and the plasma will act as a positive lens [214, 215].

The spot size of a Gaussian pulse (cf. Eqn. (2.24)) evolves as [216]

$$w(r) = w_0 \sqrt{1 + \left(1 - \frac{P}{P_c}\right)\frac{x^2}{x_R^2}}, \tag{2.68}$$

where

$$P_c = \frac{2ce^2\omega^2}{r_e^2\omega_p^2} \tag{2.69}$$

is the critical power for relativistic self-focusing, at which the diffraction and focusing effects are balanced and the constant-energy pulse does not diverge in the homogeneous plasma. For $\lambda = 800\,\mathrm{nm}$ light, $P_c \simeq 53\,\mathrm{GW}$, which is far exceeded in modern laser systems.

The behaviour of a relativistic self-focused pulse is shown in Fig. 2.8. A laser pulse with $P < P_c$ is seen to propagate beyond the Rayleigh range, but nevertheless diffracts similar to in vacuum, though at a lesser rate. A pulse with $P > P_c$ catastrophically self-focuses under this model. Higher-order effects relating to the refractive index of a relativistic plasma will cause a self-focused pulse to refract and its spot size to increase. After this occurs, the pulse will either oscillate about an average spot size or continue to diffract, depending on the initial radius of curvature of the wavefront [216].

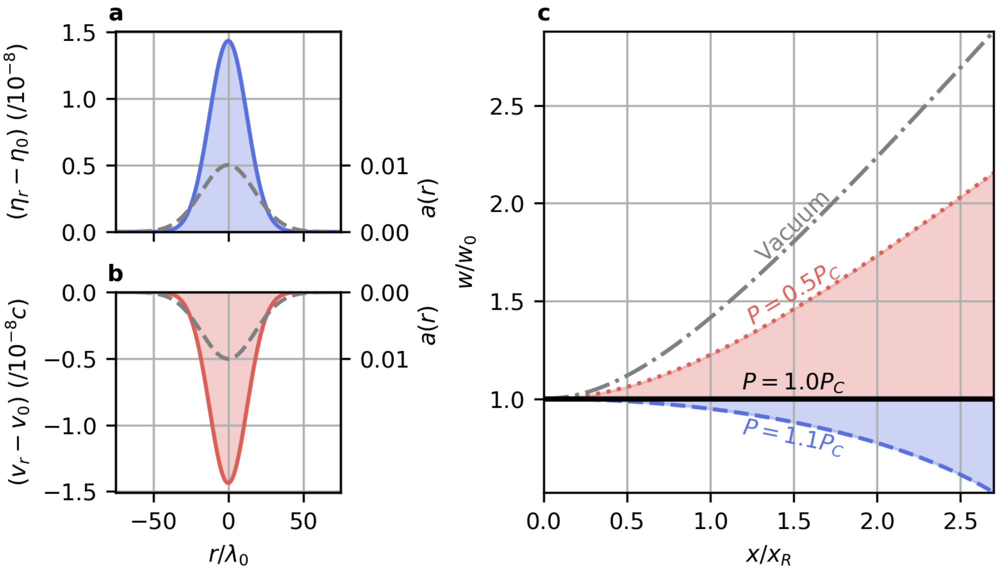

Figure 2.8: **a** & **b**, Radial change in refractive index (**a**) and laser phase velocity (**b**) due to a weakly relativistic ($a_0 = 0.01$) Gaussian laser with $w_0 = 25\lambda_0$ (dashed) in a plasma with $n_0 = 5.75 \times 10^{-4} n_c$. **c**, Spot size evolution in vacuum (dot-dashed) and with weak (dotted), matched (solid) and catastrophic (dashed) self-focusing.

Very short pulses are typically used in the LWFA bubble regime. Ponderomotive self-focusing that leads to self-guiding occurs on time scales $\sim\omega_p^{-1}$ (and not $\sim\omega_0^{-1}$), therefore it is challenging to self-guide an LWFA driver because the head of the pulse diffracts, causing pulse front erosion [106–108, 217, 218]. However, W. Lu *et al.* developed a phenomenological theory of the blowout regime, showing self-guiding of very short pulses when the head of the driver undergoes pump depletion before it diffracts, while the bulk and tail of the pulse are guided by the bubble structure [159, 160]. In this case, a laser with

$$w_0 \simeq \frac{2\sqrt{a_0}}{k_p} \tag{2.70}$$

and similar pulse length is said to be matched to the plasma, where the factor of 2 is determined from numerical simulation [219].

Local plasma density gradients can lead to frequency shifting of photons [220], which is known as photon acceleration (or deceleration) and provides an intuitive understanding of the pulse front erosion process. The plasma perturbation towards the head of the laser pulse leads to a downshifting in frequency. The number of photons is invariant and the head of the pulse therefore loses energy. The spatially-dependent spectral shifting can also lead to self-compression of the driver (and therefore intensity enhancement), as the phase velocity of frequency-upshifted photons towards the tail of the pulse is greater than those frequency-downshifted towards the head [221–224].

2.3.5 Kinetic laser-plasma simulation

The *de facto* technique for the numerical simulation of high-intensity laser interactions with plasma is the particle-in-cell (PIC) method, where simulated particle properties evolve self-consistently with electromagnetic fields defined on a grid of cells. The simulation particles comprise a collection of a large number of physical particles represented by a smaller number of macroparticles (also called super-particles, quasiparticles and pseudoparticles). The core algorithms used in the PIC method of plasma physics simulation are described in Refs. [225, 226]. Several incremental advancements have been made recently, and modern codes now include extensions to model additional physics, such as particle collisions, ionisation and high-field QED effects. While PIC codes can model the time- and length-scales relevant to laser-plasma interactions, as well as microscopic and macroscopic plasma quantities, the method is often computationally expensive. Large-scale facilities hosting supercomputers are often required to resolve the necessary physics. The modern implementations of the key algorithms are reviewed here for completeness, as well as the physics extensions most relevant to this thesis.

There are two standard components that make up the PIC algorithm:

1. A particle pusher, which calculates the position and velocity of charged particles in continuous space due to the presence of electromagnetic fields, as well as any resulting current, and

2. a field solver, which uses Maxwell's equations (Eqns. (2.1a)-(2.1d)) to determine

the electric and magnetic field values on a discrete grid, due to the currents calculated by the particle pusher.

The electric and magnetic fields are defined on staggered grids [227]. In Cartesian coordinates, the m-directional grid-centred partial derivative of the n-directional component of the electric field at position (i_0, j_0, k_0) is given by

$$\frac{\partial E_{n_{i_0,j_0,k_0}}}{\partial m} = \frac{E_{n_{i_1,j_1,k_1}} - E_{n_{i_0,j_0,k_0}}}{\Delta m}, \tag{2.71}$$

where $(m,\, n) \in \{x,\, y,\, z\}$ and $i_1 \to i_0 + 1,\; j_1 \to j_0,\; k_1 \to k_0$ for the x-directional derivative, etc. The finite-difference time-domain (FDTD) approach also ensures that the solutions are time-centred [228]. A modified leapfrog scheme is typically used in modern PIC codes so that the fields are defined simultaneously (as opposed to the electric and magnetic fields being known a half-step apart), and the particle positions and velocities are defined at every time step and half time step [229].

The macroparticle positions and velocities are often calculated using the Boris algorithm [230], which is relatively computationally inexpensive. If the problem requires resolution of highly relativistic particles, the Boris algorithm may introduce errors as it is not Lorentz invariant. In such cases, a more advanced algorithm may be used [231,232]. A charge-conserving scheme is then used to deposit charge on the grid [233].

The above process is iteratively computed, with a time step governed by the Courant-Friedrichs-Lewy (CFL) condition [234]:

$$\Delta t < \frac{\sqrt{\Delta x^2 + \Delta y^2 + \Delta z^2}}{c}, \tag{2.72}$$

where Δx, Δy and Δz are the grid sizes in the x-, y- and z-direction, respectively. This is one criterion of numerical stability of the simulation and can be interpreted physically as preventing packets of field information (i.e. electromagnetic waves) from traversing the discrete spatial grid faster than they can be resolved. The algorithm is summarised in Fig. 2.9.

A more specialised implementation uses a decomposition into azimuthal modes (in cylindrical coordinates), which can be computed on a 2D grid [149, 235]. As usual,

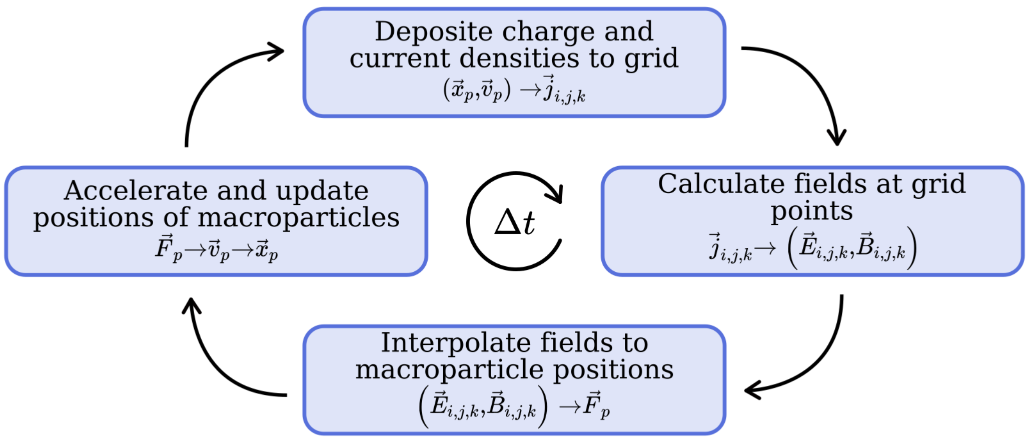

Figure 2.9: The core particle-in-cell algorithm. Subscripts p and i, j, k denote particle and grid quantities, respectively.

the particles move in continuous 3D space. This scheme is well suited to problems that have close to cylindrical symmetry (such as modelling an LWFA) with the main advantage being a significant reduction in computational resources (both memory and compute) when compared with a full-3D implementation. The resource requirements scale with the spatial resolution and macroparticle count, as with Cartesian PIC, but also with the number of modes, which must be chosen to amply describe the problem. For instance, an idealised LWFA will require the first two modes ($m = 0$ to describe the ideal wake, $m = 1$ to describe a linearly polarised laser), while nonlinear phenomena (such as off-axis wavebreaking or the acceleration of an asymmetric electron bunch) can require higher modes.

FDTD-based schemes can suffer from spurious numerical dispersion [236], which can drastically affect simulation results when relativistic beams are present. In particular, numerical Cherenkov radiation arises when highly relativistic particles exceed the speed of electromagnetic wave propagation, which is artificially lowered due to the grid [237]. A technique that can eliminate numerical dispersion at the cost of flexibility in the space of solvable problems involves transforming the fields to frequency space by the Fourier transform (or the Hankel transform in the case of radial grid components), which allows the analytic solution of Maxwell's equations in time, then transforming back to cylindrical space before the field gathering step [149].

Of particular relevance to this thesis is the impact of ionisation on the system, where the particle species is initially in a neutral gaseous state. In PIC codes, ionisation is included using the Monte Carlo method. The following describes the methods employed in the EPOCH code [229] (which is used for the ionisation studies discussed in later chapters of this thesis). The steps remain broadly relevant in any PIC code that models ionisation, although exact implementation details can vary.

The ionisation rate W is determined at every time step using the local electric field for each macroparticle that has at least one bound electron, and is given by

$$W(E) = \begin{cases} \mathtt{min}\left(W_{\mathrm{MPI}}(E),\, W_{\mathrm{ADK}}\left(E_T\right)\right) & \text{for } E \leq E_M \\ W_{\mathrm{ADK}}(E) & \text{for } E_M < E \leq E_T \\ \mathtt{min}\left(W_{\mathrm{ADK}}(E),\, W_{\mathrm{BSI}}(E)\right) & \text{for } E_T < E \leq E_B \\ W_{\mathrm{BSI}}(E) & \text{for } E > E_B \end{cases}, \tag{2.73}$$

where W_{MPI} is the rate of multiphoton ionisation [238], W_{ADK} is the tunnel ionisation rate [82], W_{BSI} is the barrier suppression ionisation rate [239], and E_T is the ADK cut-off [238], $E_B = \omega\sqrt{8\varepsilon}$ is the transition point between MPI and BSI tunnelling models [240] and E_B is the turning point of the ADK rate equation [229]. At each step, the neutral macroparticle is replaced by an ion and electron if $U_1 < 1 - \mathrm{e}^{-W\Delta t}$, where $U_1 \in [0,\, 1]$ is a random number drawn from a uniform sample.

The PIC codes used in this thesis are EPOCH [229] and FBPIC [149], each of which is more suited to a given problem. Both are open source and actively maintained [241,242]. EPOCH is a mature, versatile and robust code and is a long-used tool within the laser-plasma physics community. It is used for problems that require laser beams propagating along oblique axes, consideration and control of ionisation effects[12], and/or where a 1D coordinate space is sufficient. FBPIC is used for LWFA studies where the system approaches cylindrical symmetry. It has the further advantage of being able to run on graphics processing units (GPUs), which enables highly efficient computation.

[12]While FBPIC does implement ionisation, the routines are directly controllable in EPOCH and well documented in Ref. [229].

Chapter 3

Numerical and theoretical investigation of plasma gratings

Solid state optical components used in high-power laser systems have damage thresholds governed by the breakdown of the material due to photoionisation. For the ∼10 fs pulses from the highest-power state-of-the-art lasers at the time of writing, the fluence damage threshold is $\sim 1\,\mathrm{J\,cm^{-2}}$ [243–245]. The beam diameters in the late stages of a high-power laser chain are large to avoid the risk of damage to optical components. However, these optics are expensive and damage to the devices can still occur, which often leads to costly repairs and setbacks to research and application programmes.

A possible solution to damage susceptibility is to use plasma as the optical medium. Plasma is optically active and already 'broken down', so components based on plasma would have a damage threshold orders of magnitude greater than those based on solid state media. Plasma is also replenishable; a new optical device can be generated on each laser shot, and any 'damage' to the plasma itself is inconsequential.

These promising features have driven significant research efforts in the field of plasma optics, and several schemes have been proposed and are in various stages of investigation and development. For example, solid density plasma mirrors are now routinely used to enhance the temporal contrast of ultra-intense laser pulses [27, 28], providing a potential path to fields at the Schwinger limit [30], enabling holographic manipulation of intense lasers [29], and producing attosecond-duration high-harmonic pulses [246–248]. The stimulated Raman [21–24] and Brillouin [25, 26] backscattering instability utilise electron and ion acoustic waves, respectively, to provide high gain amplification of a seed laser pulse. Plasma waveguides are often used to guide high-intensity laser pulses over many Rayleigh lengths [191].

This chapter presents a numerical and theoretical investigation into the creation of volume plasma density gratings by nonrelativistic, intersecting laser pulses in underdense plasma. Two methods of grating creation are considered: a two-stage process driven by the ponderomotive force of the beat wave of crossing laser pulses combined with exploiting ion inertia in Sec. 3.1;[1] and by ionisation of neutral gas in Sec. 3.2.[2] The formation and evolution of the gratings and their effect on a probing laser pulse is discussed. A novel amplification method is demonstrated. Finally, it is shown in Sec. 3.3 that both inertial and ponderomotive gratings contribute to the dynamics, which is of direct relevance to the experimental investigation presented in Ch. 4.

3.1 Inertial plasma gratings

When two or more laser pulses with a common electric field component collide in underdense plasma, the ponderomotive force associated with the beat wave separates electrons from ions that form the background. The resulting space-charge force of displaced electrons imparts momentum to the ions, which begin moving towards the ponderomotive troughs. Due to their inertia, the ions maintain their trajectory when the pulses have passed. The electrons are compelled to maintain quasineutrality of the plasma by the Coulomb force and the ions thus drag the electrons along with them. A longitudinal focus of the ion trajectories is created at the nodes of the electric field beat wave (which may not be present). A deep, quasineutral density grating eventually forms at the focus, after which the structure washes out [249].

The formation of an inertial grating is discussed in Sec. 3.1.1 and key parameters are investigated numerically. The dispersion relations for electromagnetic waves propagating in an inertially-produced plasma grating are presented in Sec. 3.1.2 and

[1] Abbreviated to 'inertial' or 'ponderomotive' grating.
[2] Abbreviated to 'ionisation grating'.

its optical properties are discussed. Particular attention is paid to an inertial plasma grating acting as a waveplate.

3.1.1 Formation of the structure

It is instructive to first develop an analytical model of the laser-plasma interaction. The methodology of Lehmann & Spatschek (2016) [32] is followed, and all steps are shown for completeness.

Consider two degenerate laser pulses, denoted 1 and 2, counterpropagating in the x-direction with amplitudes $a_1 = a_2 \equiv a_0$ and frequencies $\omega_1 = \omega_2 \equiv \omega_0$. The vector potential of each pulse is

$$\vec{A}_{1,2} = a_0 \cos\left(k_{1,2}x - \omega_0 t\right)\hat{z}, \tag{3.1}$$

where $k_1 = -k_2$. The fields form a stationary beat wave when the pulses overlap. If this occurs in uniform underdense plasma with number density n_0, the beat wave has an associated ponderomotive potential given by Eqn. (2.44). If the pump pulses have $a_0 \ll 1$ (which is the case throughout this thesis), then the relativistic factor averaged over fast oscillations due to the laser pulses is given by [250]

$$\begin{aligned}\bar{\gamma} &\approx 1 + \frac{1}{4}\left(a_1^2 + a_2^2 + 2a_1a_2\cos(2kx)\right) \\ &= 1 + \frac{a_0^2}{2}\left(1 + \cos(2kx)\right),\end{aligned} \tag{3.2}$$

where

$$k = k_0\left(1 - \frac{n_0}{n_c}\right)^{\frac{1}{2}} \tag{3.3}$$

is the laser wavenumber in plasma and $|k_1| = |k_2| \equiv |k_0|$. The ponderomotive force is therefore

$$F_{p,e} = -m_e c^2 a_0^2 k \sin(2kx). \tag{3.4}$$

As usual, the effect of the ponderomotive force on the ions is neglected as it is smaller by a factor of ~1836 for hydrogen plasma. By also neglecting the evolution of the pump lasers and assuming only a small perturbation $n_e = n_{e,0} + n_{e,1}$ near the beginning of the interaction, the linearised fluid equations may be used to describe the electron motion:

$$\frac{\partial v_e}{\partial t} = \frac{e}{m_e}\partial_x \phi - \frac{F_{p,e}}{m_e} \tag{3.5}$$

$$\frac{\partial n_{e,1}}{\partial t} + n_{e,0}\frac{\partial v_e}{\partial x} = 0 \tag{3.6}$$

$$\frac{\partial^2 \phi}{\partial x^2} = \frac{e}{\varepsilon_0} n_{e,1}. \tag{3.7}$$

Differentiating Eqn. (3.5) with respect to x and substituting in Eqns. (3.4) (3.7) gives

$$\frac{\partial^2 v_e}{\partial t \partial x} = \frac{e^2}{m_e \varepsilon_0} n_{e,1} + 2c^2 a_0^2 k^2 \cos(2kx). \tag{3.8}$$

Differentiating Eqn. (3.6) with respect to t and inserting Eqn. (3.8) gives

$$\frac{\partial^2 n_{e,1}}{\partial t^2} + \omega_p^2 n_{e,1} + 2n_{e,0} c^2 a_0^2 k^2 \cos(2kx) = 0. \tag{3.9}$$

Setting $n_{e,1} = \delta n_e n_{e,0}$ results in the second order inhomogeneous differential equation

$$\frac{\partial^2 \delta n_e}{\partial t^2} + \omega_p^2 \delta n_e = -2c^2 a_0^2 k^2 \cos(2kx). \tag{3.10}$$

The general solution to the homogeneous equation is

$$\delta n_e = C \mathrm{e}^{i\omega_p t}, \tag{3.11}$$

for some constant C. Assuming a particular solution that is constant in time and using Euler's formula gives

$$\delta n_e = A\cos(\omega_p t) + \frac{2c^2 a_0^2 k^2}{\omega_p^2}\cos(2kx). \tag{3.12}$$

Evaluating the solution at $t = 0$ (when the pulses arrive and where the plasma is unperturbed) and assuming $F_{p,e}$ starts at the same time results in

$$\delta n_e = \frac{2c^2 a_0^2 k^2}{\omega_p^2}\cos(2kx)\left(\cos(\omega_p t) - 1\right). \tag{3.13}$$

The electron perturbation gives rise to an electric field, which can be found by integrating Eqn. (3.7):

$$E_x = -\frac{\partial \phi}{\partial x} = \frac{k m_e c^2 a_0^2}{e} \sin(2kx)\left(\cos(\omega_p t) - 1\right), \tag{3.14}$$

which imparts momentum to the ion species. For the hydrogen plasma considered here, the ion motion is governed by

$$\frac{\partial v_i}{\partial t} = -\frac{e}{m_i}\frac{\partial \phi}{\partial x}. \tag{3.15}$$

By substituting Eqn. (3.14) and integrating, the ion velocity is

$$v_i = k c^2 a_0^2 \frac{m_e}{m_i} \sin(2kx)\left(\frac{\sin(\omega_p t)}{\omega_p} - t\right). \tag{3.16}$$

Following the same procedure as for the electrons, the ion perturbation is

$$\delta n_i = \frac{m_e}{m_i}\frac{c^2 k^2 a_0^2}{\omega_p^2} \cos(2kx)\left(2 - 2\cos(\omega_p t) - \omega_p^2 t^2\right), \tag{3.17}$$

where $n_{i,1} = \delta n_i n_{i,0}$. The electron and ion perturbations and electric field at time $t = 200\pi/\omega_0$ after being driven by pump pulses with $a_0 = 0.02$ are shown in Fig. 3.1. The electron and ion perturbations are in phase and both π out of phase with the E-field beat wave. The ion density perturbation is negligible as expected due to the prefactor of Eqn. (3.17) being $\ll 1$.

The ion perturbation is significant when $n_{i,1} \to n_{i,0}$ and therefore $\delta n_i \to 1$. Setting $x = n\pi/k$, an estimate for the time for significant ion perturbation to occur is

$$t \approx \left(\frac{m_i}{m_e}\frac{1}{k^2 c^2 a_0^2}\right)^{\frac{1}{2}}. \tag{3.18}$$

For $m_i/m_e = 1836$ (hydrogen plasma), $n_0 = 0.1 n_c$, $\lambda = 800\,\mathrm{nm}$ and $a_0 = 0.02$, the ion time scale is of order 1 ps. This perturbative approximation is valid while $\delta n_e \ll 1$.

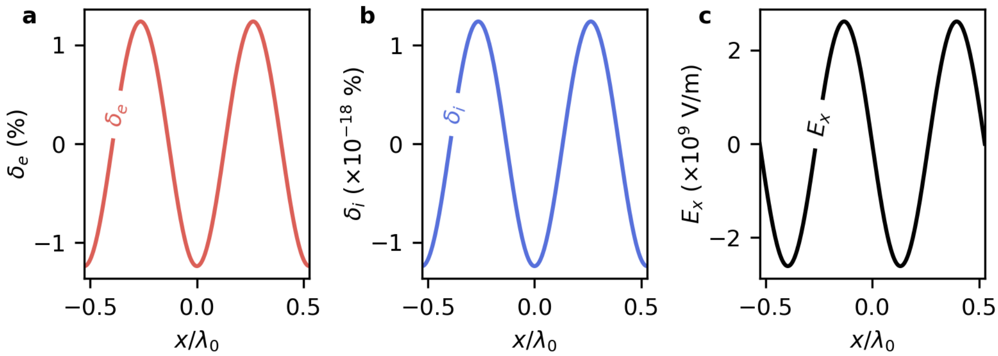

Figure 3.1: Number density perturbations and corresponding electric field for a 1-dimensional plasma grating at $t = 200\pi/\omega_0$ driven by pump pulses with $a_0 = 0.02$. **a**&**b**, The electron and ion perturbations, respectively. **c**, The resulting electric field.

One-dimensional particle-in-cell (PIC) simulations

The method of PIC simulation of plasma physics problems is described in Sec. 2.3.5. The current section presents a study of the evolution of one-dimensional inertial plasma gratings (i.e., those formed by pump laser beams of infinite extent in the directions transverse to the propagation axis, but with variable temporal structure) and the dependence of their temporally evolving properties on a number of parameters. The one-dimensional approximation is chosen to allow for very high resolution of the discrete spatial grid and particle phase spaces. The greater tractability when compared with higher-dimensional simulations also allows for an increased number of simulations, enabling multi-parametric scans to be performed.

The evolution of a 1-dimensional inertial plasma grating is shown in Fig. 3.2. The data are generated using EPOCH, where two counterpropagating, degenerate laser pulses with $a_0 \simeq 0.02$ collide at the centre of a fully ionised hydrogen plasma slab with $n_0 = 0.1n_c$. The lasers have wavelengths $\lambda = 800\,\text{nm}$ and Gaussian temporal intensity profiles with full-width at half-maximum durations $\tau = 250\,\text{fs}$, and are coupled into the plasma via linear density ramps of length 2λ.[3] To finely resolve the plasma processes and distribution functions, the simulation employs a cell size of 1.6 nm and 2^{14} macroparticles per cell per species. The simulation input file is given in Appx. C.2.

[3]The linear density coupling ramps reduce reflection of the pump pulses compared with a step vacuum-plasma boundary.

The initially homogeneous plasma in the plateau region is relatively undisturbed as the pump pulses collide and pass (Fig. 3.2**a**, $t < 1\,\mathrm{ps}$). However, on inspection of the position-momentum phase space distribution just after the pump pulses have passed at $t = 1\,\mathrm{ps}$ (Fig. 3.2**b**,**d**), there is evidence of phase space mixing of the electrons and acceleration of the ions towards the prior positions of the beat wave nodes. The ions continue along their inertial trajectories and the plasma remains locally neutral as the electrons are strongly attracted to the slowly-moving ions. The grating amplitude is maximised when the neighbouring ion sheets maximally overlap in space, which occurs at $t = 1.98\,\mathrm{ps}$, around $1.4\,\mathrm{ps}$ after the pump pulses maximally overlapped. This agrees very well with the predictions of Eqn. (3.18), despite the simplifying assumptions. The corresponding peak density in this case is $n_{\mathrm{sat}} \simeq 2.7n_0 \simeq 0.27n_c$.

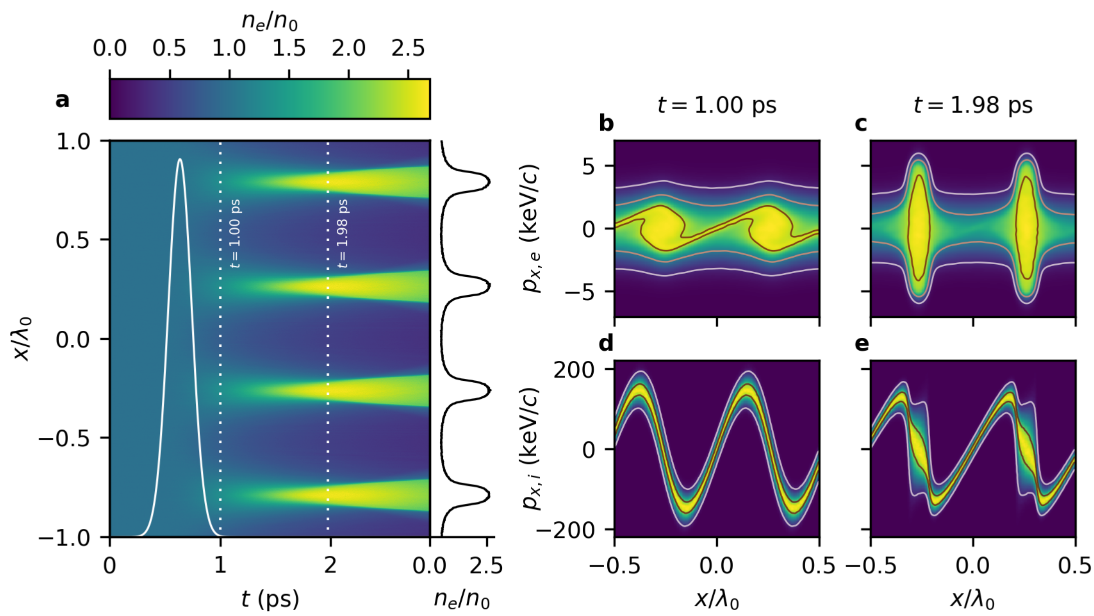

Figure 3.2: A 1-dimensional inertial plasma grating. **a**, Evolution of the electron number density (colour scale) during and after being driven by overlapping pump pulses (solid white). A snapshot of the number density at $t = 1.98\,\mathrm{ps}$, where the grating is saturated, is shown in the right pane. **b**-**e**, Position-momentum phase space of the electrons (**b** & **c**) and ions (**d** & **e**) at the times indicated by the dotted lines in **a**.

The x-directional electric fields of the plasma are shown in Fig. 3.3. Around the time of maximum overlap of the pumps, indicated by the dashed white line, a periodic electric field is set up by the charge separation of electrons and ions, driven by the ponderomotive force. It is this briefly-present field that imparts momentum to the ions. The plasma remains mostly locally neutral following this charge separation, except for the build-up of electron sheaths surrounding the ion density peaks, which is evidenced by the relatively strong localised fields. Sheaths are present due to the finite temperature of the electron species, whose thermal pressure is sufficiently strong to broaden the number density distribution of the electrons and displace them from the bunched ions.

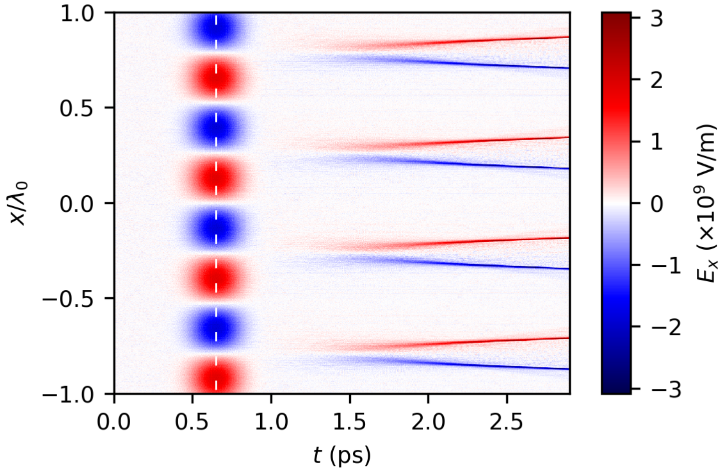

Figure 3.3: The x-directional plasma electric fields during the formation and early decay of a 1-dimensional plasma grating. The dashed white line indicates the time of maximal overlap of the pump laser pulses.

Fig. 3.4 shows the evolution of the electron (panel **a**) and ion (panel **b**) momentum distributions. As the laser electric fields are perpendicular to the propagation vector, electrons are not accelerated in the x-direction by the laser electric fields, which are centred at t_0. Because of their low mass, they pick up very little x-directional momentum from the ponderomotive force. This is nevertheless sufficient to drive charge separation of the electrons and ions. The ions respond strongly to the fields set up by the charge separation but gain no further momentum when the pump pulses have passed. The ions gradually lose the imparted momentum to the electrons.

Two 1D simulation parameter scans were performed to investigate the effects of pump pulse intensity and duration and initial plasma temperature on the formation of

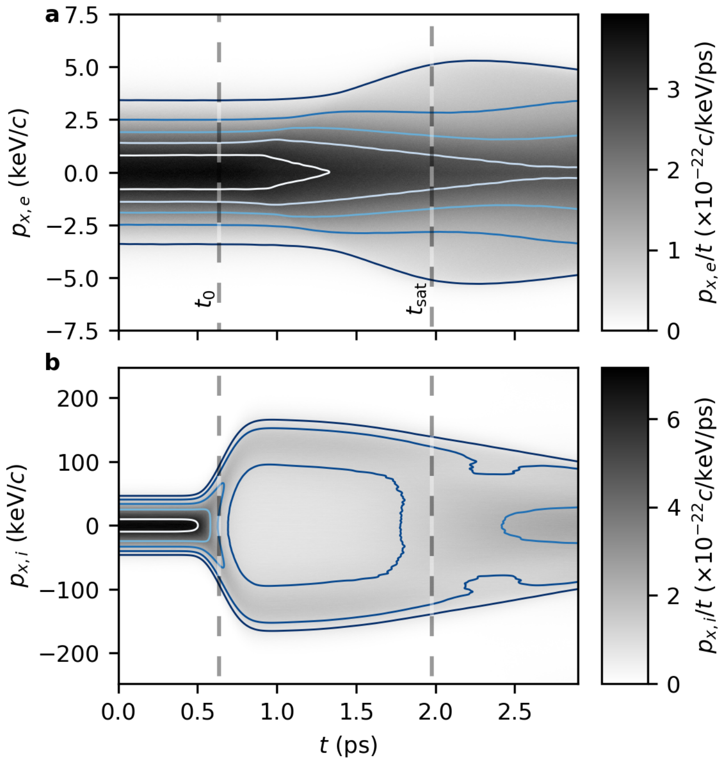

Figure 3.4: **a**, Temporal evolution of the electron momentum distribution of a 1-dimensional plasma grating. The pump laser temporal centres, t_0, and grating saturation time t_{sat}, are indicated by the dashed lines. The solid contours show isolines of the distribution function. **b**, As **a** but for the ion species.

an inertial plasma grating. Both employed $\lambda = 800\,\mathrm{nm}$ Gaussian pump pulses colliding in a plasma slab of length 4λ and density $0.1n_c$, and used 100 cells per laser wavelength and 2^9 macroparticles per species per cell.

The first parameter scan comprises 100 simulations with 10 equally-spaced pump pulse intensity values ranging from $I_0 = 1 \times 10^{15}\,\mathrm{W\,cm^{-2}}$ to $1 \times 10^{16}\,\mathrm{W\,cm^{-2}}$ ($a_0 \simeq$ 0.022 to 0.068) and 10 equally-spaced values of the pump pulse duration (full-width at half-maximum of the intensity) ranging from $\tau = 100\,\mathrm{fs}$ to $500\,\mathrm{fs}$. The initial electron and ion species temperatures are kept the same at $T_e = 5\,\mathrm{eV}$ and $T_i = 0.1T_e$, respectively, which are indicative of plasmas produced by short-pulse, high-power lasers [193]. Results of the simulation scan are shown in Fig. 3.5. A bicubic interpolation has been performed on the data in panels **a** and **b** to illustrate the continuous nature of the underlying distributions. The electron number density is measured at grating amplitude maximum and the peak value, $n_{e,\mathrm{peak}}$, is shown in panel **a** normalised to the initial number density, n_0. The peak number density depends strongly on both pump pulse intensity and duration. The time-to-maximum, determined from the time of maximum spatial overlap of the pump pulses, t_0, shown in panel **b**, is relatively stable for parameters $I_0 > 2.5 \times 10^{15}\,\mathrm{W\,cm^{-2}}$, $\tau > 200\,\mathrm{fs}$. However, for low values of pump pulse duration and intensity, $t_{\mathrm{sat}} - t_0$ varies strongly. The maximum electron and ion number densities in a subset of simulations are plotted over time for fixed τ and varying I_0 in panel **c**, and fixed I_0 and varying τ in panel **d**. The more strongly-driven gratings are seen to maximise and decay more rapidly and exhibit a larger peak density.

The simulations of the second parameter scan uses identical conditions to the first, except the second parameter scanned is the plasma temperature instead of pump pulse duration, which is fixed at $\tau = 250\,\mathrm{fs}$. Ten evenly-spaced initial electron temperature values are simulated, with values ranging from $T_e = 1\,\mathrm{eV}$ to $20\,\mathrm{eV}$. Ion temperature is fixed at $T_i = 0.1T_e$, as before. Results are shown in Fig. 3.6. Panel **a** shows $n_{e,\mathrm{peak}}$, which is again seen to depend strongly on pump pulse intensity. The peak number density also diminishes with increasing initial plasma temperature as the thermal pressure works against the inertia of the ions and the Coulomb attraction of the electrons to the ions. The time to saturation depends weakly on the temperature, shown in panel

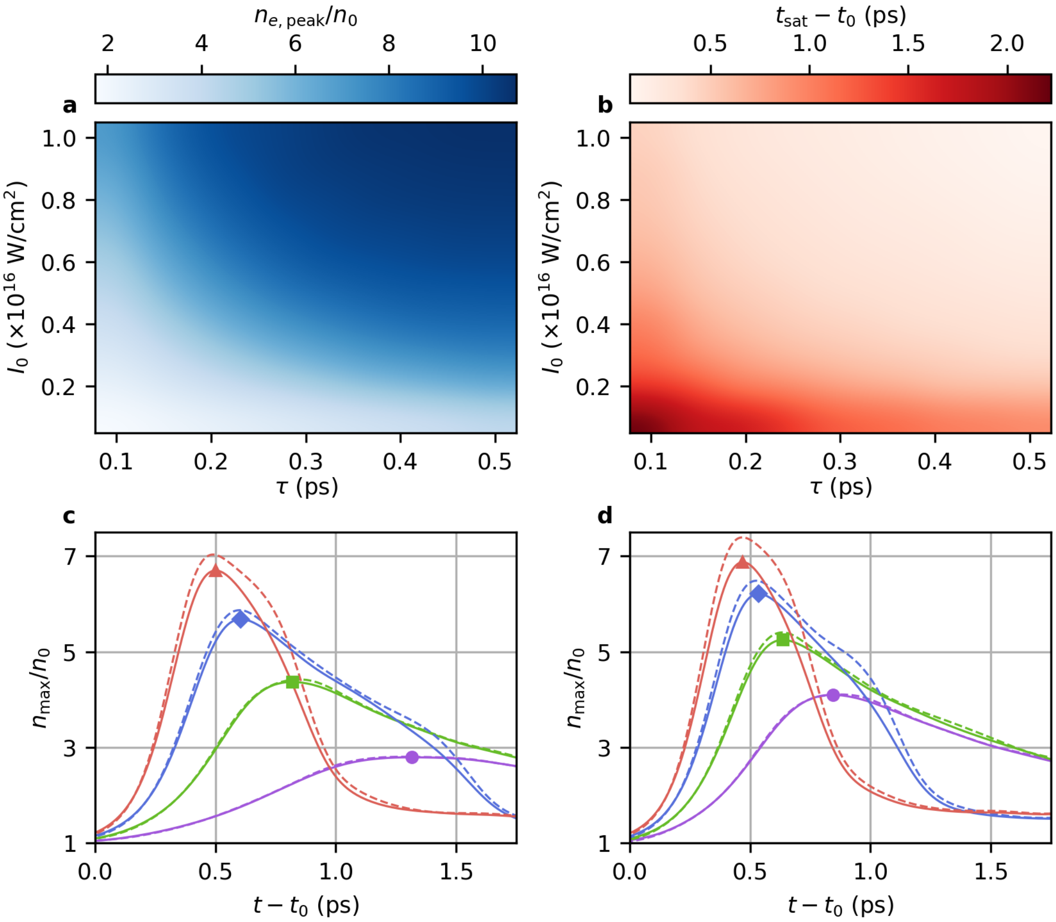

Figure 3.5: Results of a pump intensity and duration parameter scan for an initial plasma density $n_0 = 0.1n_c$. **a**, Peak electron number density (at saturation) of the plasma grating. **b**, Formation time of the plasma grating, measured from the pump pulse temporal centre overlap (t_0) to the grating saturation (t_{sat}). **c**, Evolution of the maximum number density of electrons (solid) and ions (dashed) for pump pulses with fixed $\tau = 0.278\,\mathrm{ps}$ and varying intensity $I_0 = 1 \times 10^{15}$ (purple circle), 2×10^{15} (green square), 3×10^{15} (blue diamond), $4 \times 10^{15}\,\mathrm{W\,cm^{-2}}$ (red triangle). The markers are located at $n_{e,\mathrm{peak}}$. **d**, As **c** but for fixed pump pulse intensity $I_0 = 5 \times 10^{15}\,\mathrm{W\,cm^{-2}}$ and varying $\tau = 100$ (purple circle), 144 (green square), 189 (blue diamond), 233 fs (red triangle).

b, as the electron and ion thermal velocity is small compared to the velocity acquired due to the space-charge forces.

Simulations with particle collisions

A simulation has been performed to investigate the importance of particle collisions on the formation of an inertial plasma grating. The simulation has identical parameters to that presented in Fig. 3.2 ($a_0 = 0.02$, $n_0 = 0.1n_c$, $\lambda = 800\,\mathrm{nm}$, $\tau = 250\,\mathrm{fs}$, cell size of $1.6\,\mathrm{nm}$ and 2^{14} macroparticles per cell), except collisional modules were enabled. These are typically disabled due to their computational cost. The collision modules used are built into EPOCH and derive from Ref. [251], which are in turn based on Ref. [252], and described in Sec. 2.3.5. Another collisionless simulation with identical parameters, except $I_0 = 5 \times 10^{15}\,\mathrm{W\,cm^{-2}}$, is performed. For this section, the collisional simulation is referred to as simulation (a) and the low- and high-intensity pump collisionless simulations as simulations (b) and (c), respectively.

The evolution of the electron number density profile for the three simulations described above is shown in Fig. 3.7. The panel labels are consistent with the above description. There are no immediately perceivable differences between simulations (a) and (b).

To quantify any variations in the simulations, three measurements are made: (i) the minimum and (ii) maximum number density values achieved during the simulation, and (iii) the normalised sum of square differences of the spatiotemporal number density profiles. The latter is defined as

$$\hat{S}_{i,j} = \frac{\sum_{n,m} \left(n_i[n,m] - n_j[n,m]\right)^2}{\sqrt{\sum_{n,m} n_i[n,m]^2 \times \sum_{n,m} n_j[n,m]^2}} \tag{3.19}$$

for two spatiotemporal number density profiles $n_{i,j}$ with m discrete measurement points in time and n in space and $i, j \in \{a, b, c\}$. This is a measure of the similarity of the two profiles. Two similar profiles will have a low value, and for $i = j$, $\hat{S}_{i,j} = 0$. The density measurements are summarised in Table 3.1. The differences between the minimum and maximum number density measurements of simulations a and b are minimal. As

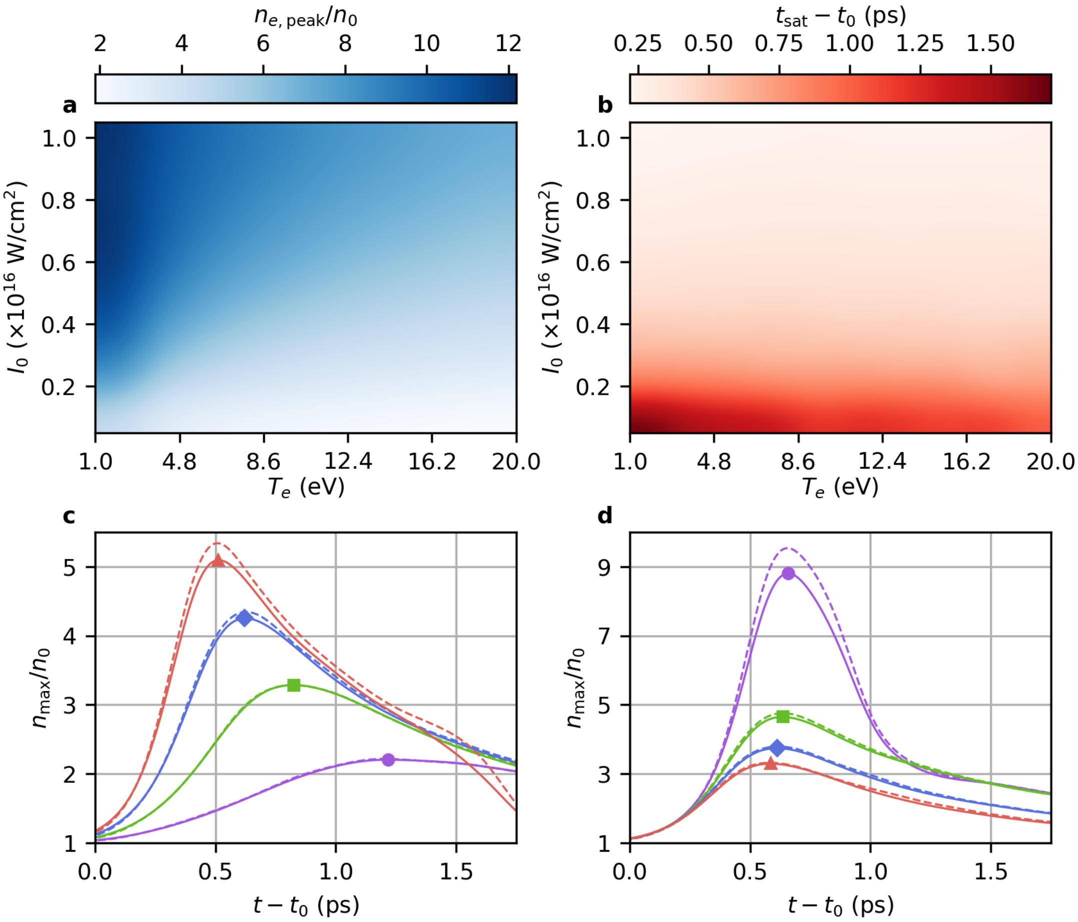

Figure 3.6: Results of pump intensity and initial plasma temperature scan for an initial plasma density $n_0 = 0.1n_c$. The initial ion temperature is $T_i = 0.1T_e$. **a**&**b**, As Fig. 3.5**a**&**b**, but with varying initial plasma temperature instead of pump pulse duration. **c**, Evolution of maximum number density of electrons (solid) and ions (dashed) with fixed $T_e = 9.44\,\mathrm{eV}$ and varying intensity $I_0 = 1 \times 10^{15}$ (purple circle), 2×10^{15} (green square), 3×10^{15} (blue diamond), $4 \times 10^{15}\,\mathrm{W\,cm^{-2}}$ (red triangle). **d**, As **c** but for fixed pump pulse intensity $I_0 = 3 \times 10^{15}\,\mathrm{W\,cm^{-2}}$ and varying $T_e = 1.0$ (purple circle), 7.3 (green square), 13.7 (blue diamond), 20.0 eV (red triangle).

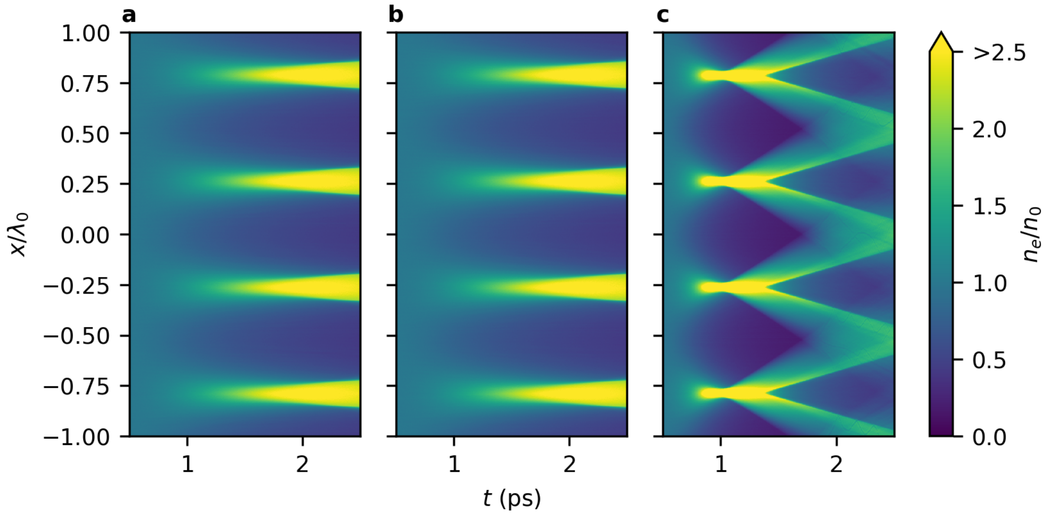

Figure 3.7: Comparison of the number density evolution of inertial gratings simulated with and without collisions, as described in the text. **a**, With collisional modules enabled. **b&c**, Low ($I_0 = 1 \times 10^{15}\,\mathrm{W\,cm^{-2}}$) and high ($I_0 = 5 \times 10^{15}\,\mathrm{W\,cm^{-2}}$) intensity pumps without collisional modules.

expected, the higher pump intensity drives greater depletion in the antinodes of the beat wave and stronger bunching in the troughs, leading to a significantly smaller n_{min} and larger n_{max}.

Simulation	n_{min}/n_0	n_{max}/n_0
a	0.36	2.68
b	0.35	2.67
c	0.18	7.97

Table 3.1: Minimum and maximum number density measurements.

The calculated normalised sum of square difference values are $\hat{S}_{a,b} = 1.41 \times 10^{-4}$ and $\hat{S}_{a,c} = 5.69 \times 10^{-1}$, respectively. This shows that collisions play a negligible role in the dynamics of the grating when compared with other variables such as the pump intensity.

Higher-dimensional gratings

The gratings discussed above are 'one-dimensional' as, at any given time, one spatial coordinate is sufficient to describe the properties of the structure, making 1D simulations sufficient for their analysis. An equivalent assumption is that the plasma and pump beams are infinite in all extents except for the direction of propagation of the pump pulses. Pump pulses with flat spatial profiles but finite extent[4] generate gratings that are one-dimensional within the spatial extent of the plasma or pump pulses (whichever is smaller). These gratings are still referred to as one-dimensional layered structures.

If the pump pulses have a non-flat-top spatial profile, the grating will exhibit variation in its properties in the direction transverse to the pump pulse propagation, in addition to the usual variation in the longitudinal direction. If the transverse variations are slow compared with the grating periodicity, the grating is 'quasi-one-dimensional' (or just 'one-dimensional', for brevity). An example of a quasi-1D grating is that which is formed by intersecting laser pulses with Gaussian spatial profiles. The transverse intensity profile of the pulses will lead to a transverse variation in both the peak of the grating and the time it takes for the grating to maximise.

Results from a 2D EPOCH simulation demonstrating a grating formed by counter-propagating pump pulses with Gaussian spatial profiles are shown in Fig. 3.8. The laser pulses have $\lambda = 800\,\mathrm{nm}$, $I_0 = 5 \times 10^{15}\,\mathrm{W\,cm^{-2}}$, $\tau = 500\,\mathrm{fs}$ and $w = 16\,\mathrm{\mu m}$ and are made to collide in a plasma slab with $n_0 = 6 \times 10^{19}\,\mathrm{cm^{-3}}$. Transverse variation in the grating number density at saturation is clear. A slice through one of the central grating peaks at this time reveals that the transverse profile is approximately Gaussian, similar to the pump pulses. The slice in Fig. 3.8**a** has been Gaussian-filtered to reduce the discrete particle sampling noise [253]. The maximum number density in three slices parallel to the laser axis is measured over time and shown in Fig. 3.8**b**. The axial slice (dashed red) is seen to maximise most rapidly and with the greatest amplitude, while the slices further from the laser axis exhibit a grating that forms over a longer time with a smaller amplitude.

[4]Called 'flat-top' or 'top hat' beams.

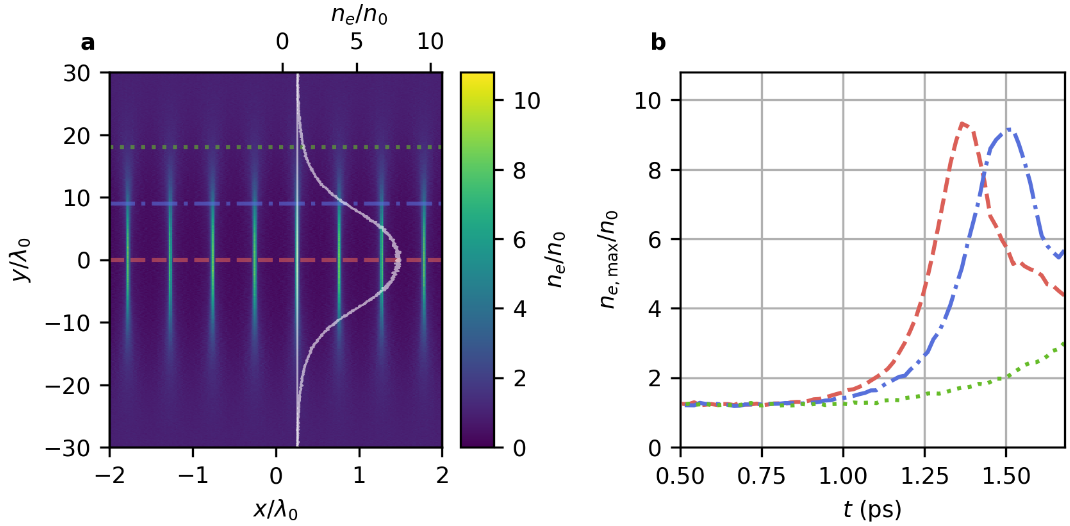

Figure 3.8: A quasi-one-dimensional inertial grating formed by intersecting Gaussian pump pulses. **a**, Number density around the centre of the grating near saturation. The white line shows a vertical slice through the grating number density at $x = 0.25\lambda$. **b**, Maximum number density in a longitudinal slice through the evolving structure. Slices are taken on the laser axis (dashed red) and $0.45w$ (9λ) and $0.9w$ (18λ) from the axis (dot-dashed blue and dotted green, respectively). The slice positions are indicated by the matching horizontal lines in panel **a**.

It is also possible to create fully two- and three-dimensional plasma structures by intersecting more than two driving laser pulses within plasma. An example of a 3D 'egg box' structure created by intersecting six degenerate laser pulses with $\lambda = 800\,\mathrm{nm}$, $\tau = 200\,\mathrm{fs}$ and $I_0 = 1 \times 10^{15}\,\mathrm{W\,cm^{-2}}$ in a plasma slab with $n_0 = 0.3n_c$ is shown in Fig. 3.9. In this configuration, two of the pump beams counterpropagate in x, two in y, and two in z. The colour scale indicates the electron density, and the local maximum electron density at any time during the interaction is $2.7n_c$.

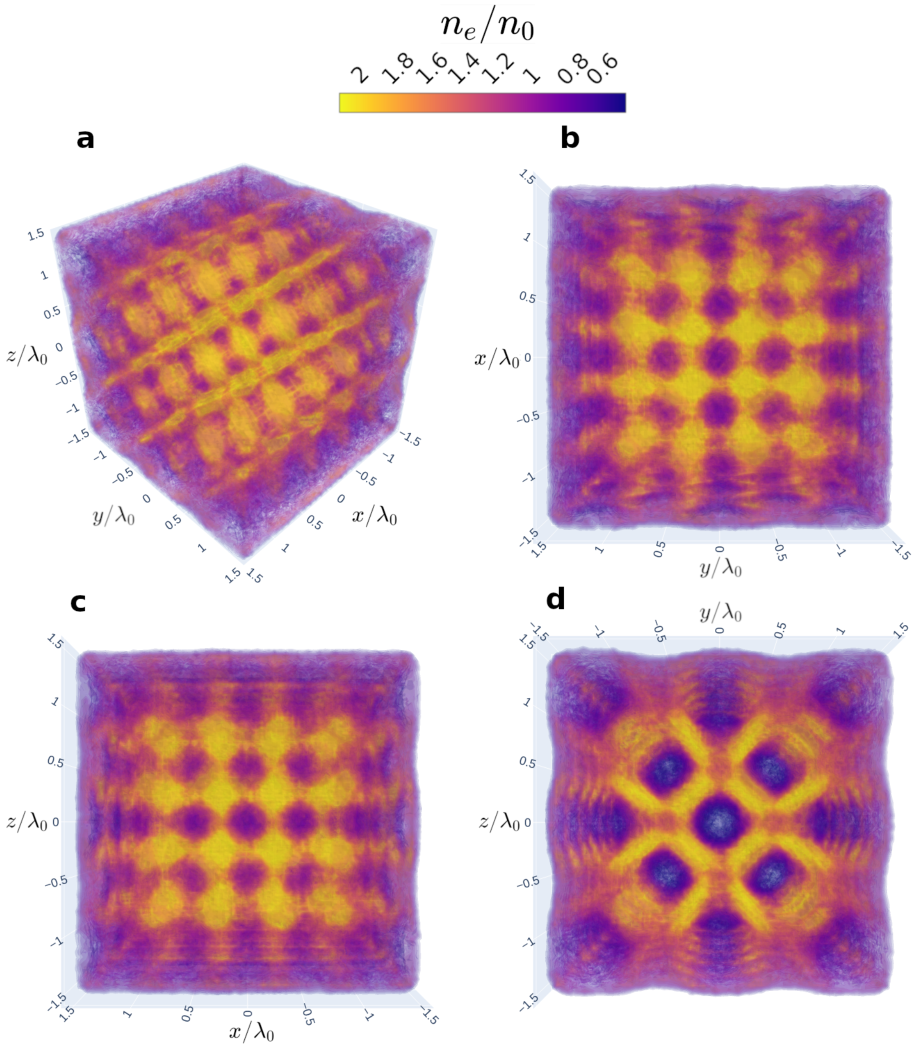

Figure 3.9: A three-dimensional plasma structure formed by six intersecting pump pulses.

3.1.2 Effect on a probing laser pulse

A 1-dimensional grating can be modelled as a layered medium with alternating values of refractive index [31, 254]. With this simple model, the performance of a 1-dimensional grating as one of several optical devices can be described, including a mirror, polariser and waveplate.

Consider the number density of the 1-dimensional plasma grating shown in Fig. 3.2**a** at its maximum. The number density profile is periodic in space and roughly rectangular. A reasonable model of the structure is one of a stratified medium, commonly found in the study of applied optics [254] and analogous to the quantum mechanical description of a crystal lattice [255]. The medium comprises alternating layers of high and low plasma density with $n = n_a$ and $n = n_b$, respectively. The thickness of each region is denoted a and b, where $\Lambda = a + b$ is the periodicity (or length of the unit cell) and is related to the pump pulse wavelength by

$$\Lambda = \frac{\lambda_0}{2\sqrt{1 - n_0/n_c}}. \tag{3.20}$$

Conservation of charge implies

$$n_0 = \frac{a n_a + b n_b}{\Lambda}. \tag{3.21}$$

The model is shown in Fig. 3.10, where the underlying plasma structure shown is taken from a simulation with identical parameters to that presented in Fig. 3.2 at saturation. Here, $n_a = 0.255 n_c$, $n_b = 0.057 n_c$, $a = 0.21\Lambda$, $b = 0.79\Lambda$.

The distinct low and high density regions of the structure have respective plasma frequencies and refractive indices, for a given wavelength of light. For the following, the normalisations

$$\omega \to \Omega = \frac{\omega\Lambda}{2\pi c} \tag{3.22}$$

$$k \to K = \frac{k\Lambda}{2\pi} \tag{3.23}$$

are used for frequencies and wavenumbers, respectively. Following the method laid

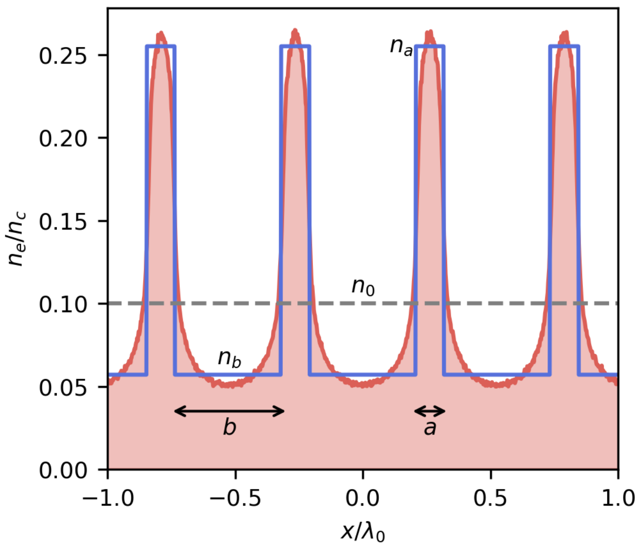

Figure 3.10: A 1-dimensional plasma grating overlaid with a model of the structure as a stratified medium.

out in Ref. [254], the dispersion relations for electromagnetic waves with electric field perpendicular (the s-wave or transverse electric (TE) wave) and parallel (the p-wave or transverse magnetic (TM) wave) to the incidence plane are

$$\begin{aligned}\cos\left(2\pi K_x^s\right) = \; & \cos\left(2\pi\frac{a}{\Lambda}K_{x,a}^s\right)\cos\left(2\pi\frac{b}{\Lambda}K_{x,b}^s\right) \\ & -\frac{1}{2}\left(\frac{K_{x,a}^s}{K_{x,b}^s}+\frac{K_{x,b}^s}{K_{x,a}^s}\right)\sin\left(2\pi\frac{a}{\Lambda}K_{x,a}^s\right)\sin\left(2\pi\frac{b}{\Lambda}K_{x,b}^s\right),\end{aligned} \tag{3.24}$$

and

$$\begin{aligned}\cos\left(2\pi K_x^p\right) = \; & \cos\left(2\pi\frac{a}{\Lambda}K_{x,a}^p\right)\cos\left(2\pi\frac{b}{\Lambda}K_{x,b}^p\right) \\ & -\frac{1}{2}\left(\frac{K_{x,a}^p\left(\Omega^2-\Omega_{p,b}^2\right)}{K_{x,b}^p\left(\Omega^2-\Omega_{p,a}^2\right)}+\frac{K_{x,b}^p\left(\Omega^2-\Omega_{p,a}^2\right)}{K_{x,a}^p\left(\Omega^2-\Omega_{p,b}^2\right)}\right)\sin\left(2\pi\frac{a}{\Lambda}K_{x,a}^p\right) \\ & \times\sin\left(2\pi\frac{b}{\Lambda}K_{x,b}^p\right),\end{aligned} \tag{3.25}$$

respectively, where

$$K_{x,a}^{s,p} = \sqrt{\Omega^2 - \Omega_{p,a}^2 - (K_y^{s,p})^2} \tag{3.26}$$
$$K_{x,b}^{s,p} = \sqrt{\Omega^2 - \Omega_{p,b}^2 - (K_y^{s,p})^2}, \tag{3.27}$$

for y-directional components of the electromagnetic field wavevector K_y and where the subscript p denotes a plasma quantity and the superscripts s and p indicate polarisation.

The dispersion relations for both s and p waves are shown in Fig. 3.11 for the grating shown in Fig. 3.10 and incident waves with $K_y = 0.5$. The inset shows a zoomed-in view of the relations around $k_x = 0$, $\omega = \omega_0$, which represents the case of a perpendicularly probing laser pulse.[5] The mismatch between the frequency of TE and TM modes about $k_x = 0$ can be understood by considering the motion of plasma electrons moving due to these fields, which oscillate either along or against the plasma grating density gradients.

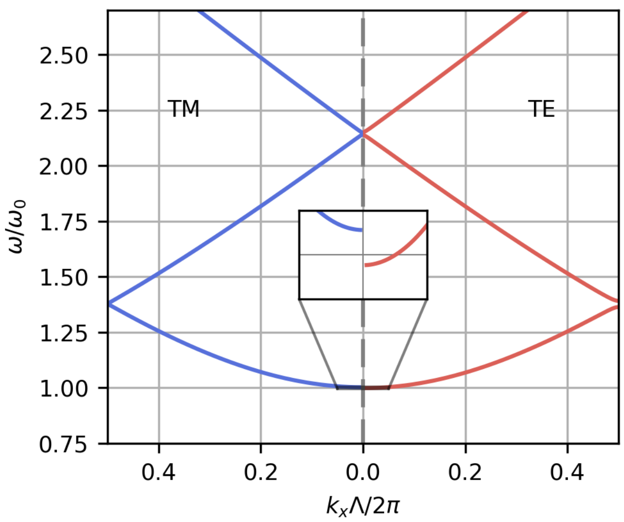

Figure 3.11: Dispersion relations for s and p waves in a subcritical plasma grating. The inset shows a zoomed-in region around $k_x = 0$ to reveal the discontinuity between the TE and TM dispersions.

The value of ω at $k_x = 0$ can be found numerically by determining the value ω

[5]This is the regime of primary interest in Ch. 4.

closest to 1 that gives a purely imaginary value of k_x.

The corresponding phase velocity is given by

$$v_{\mathrm{ph}} = \frac{\omega}{k} \tag{3.28}$$

and Eqn. (2.66) can be used to find the refractive index of the structure for each polarisation. The birefringence,

$$\Delta\eta = \eta_s - \eta_p, \tag{3.29}$$

can then be used to determine the retardance of the structure (or relative phase shift between the orthogonally polarised s and p waves) as a function of propagation distance L,

$$\Gamma = \frac{2\pi L \Delta\eta}{\lambda_0}. \tag{3.30}$$

The relation between Γ and L for the grating discussed above is shown in Fig. 3.12. This structure can act as a quarter-wave plate (inducing $\pi/2$ phase shift between orthogonal polarisation components) over a distance of ~50 µm and a half-wave plate (inducing π phase shift) over ~100 µm. These calculations are based on the assumption of a non-evolving grating that has spatial variation only perpendicular to the grating planes. With the characteristic timescale of 1 ps previously discussed, a probing laser pulse will experience a quasi-static grating for around $ct = 300$ µm.

The retardance (and, more generally, optical characteristics) of an optical device based on the ponderomotive grating scheme is highly tunable. The choice of initial plasma density and pump pulse strength and spatial extent are the key parameters of interest.

3.2 Ionisation-induced gratings

When two degenerate laser pulses overlap in neutral gas, the superposition of electric fields can result in spatially-varying levels of ionisation. The formation of such a structure is described in Sec. 3.2.1, and a mechanism of scattering of electromagnetic waves from an evolving ionisation grating that can lead to amplification is outlined in

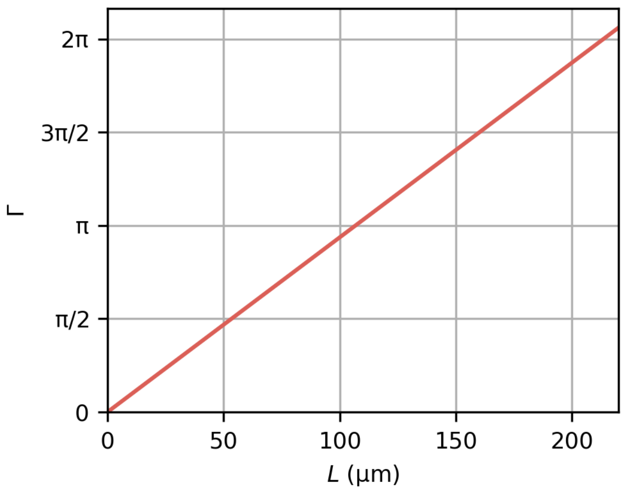

Figure 3.12: Phase shift between s and p waves propagating through an underdense plasma grating.

Sec. 3.2.2. A numerical investigation into this behaviour is presented in Sec. 3.2.3.

3.2.1 Formation of the structure

The mathematical model presented in this section and Sec. 3.2.2 were developed by Dr. Bernhard Ersfeld.

The same stationary electric field beat wave used to create the ponderomotively-driven structures presented in previous sections can also be used to create a periodic structure by ionisation. As shown in Fig. 3.13, the evolving superposition of the fields has stationary nodes where the probability of ionisation of any neutral species present is always zero. The time-averaged probability of ionisation varies with position and is maximal at the antinodes of the beat.

If the two beams are near-degenerate, but with slightly different frequencies, the beat wave spatial pattern moves slowly in the direction of the faster-oscillating field. The ionisation pattern therefore also exhibits this slow motion at the ionisation fronts. Unlike the beat wave, whose nodes move with the wave, the plasma remains ionised in the prior positions of the antinodes as the recombination time is significantly longer than the time scales of the laser.

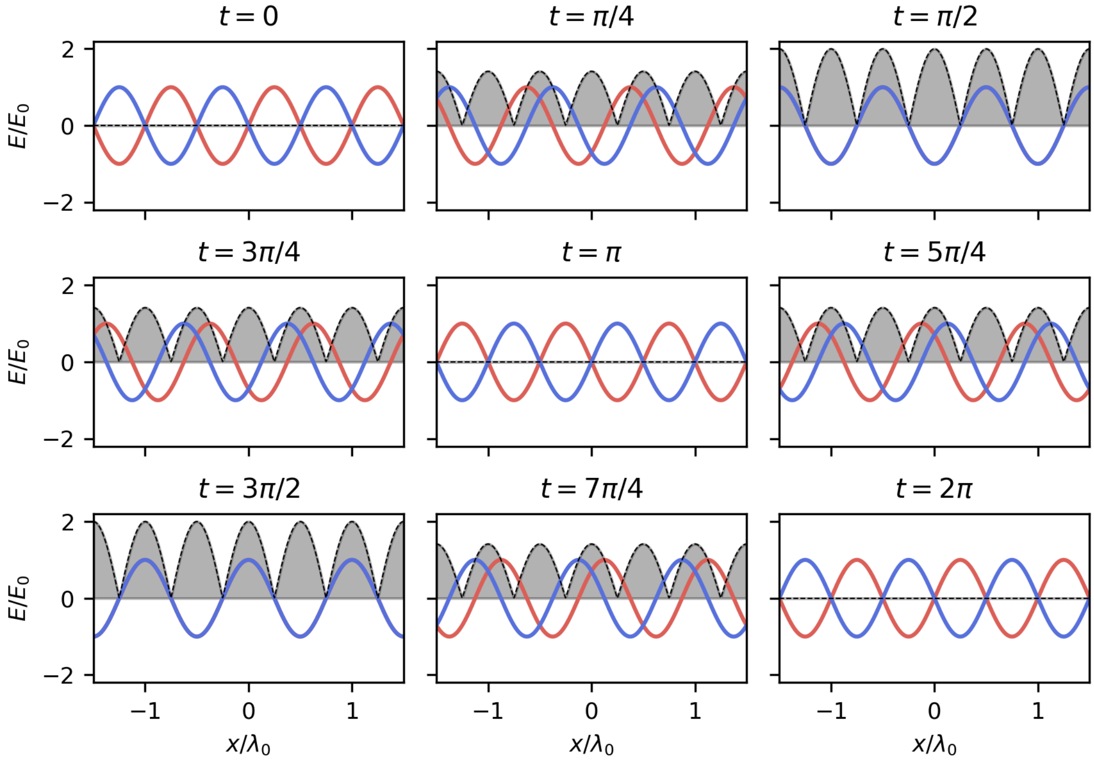

Figure 3.13: Temporal evolution of the superposition of two counterpropagating, degenerate laser fields. The individual laser fields are shown in solid red and blue, with the shaded region indicating the magnitude of the superposition.

Consider two overlapping laser beams, denoted by 0 and 1. Their mutual electric field is given by

$$\vec{E} = \frac{\left(E_0 e^{i\varphi_0} + E_0^* e^{-i\varphi_0} + E_1 e^{i\varphi_1} + E_1^* e^{-i\varphi_1}\right)}{2}\vec{e}, \tag{3.31}$$

where $\varphi_{0,1} = \vec{k}_{0,1}\cdot\vec{r} - \omega_{0,1}t$ is the phase, $\vec{k}$ and ω are the field wavenumber and frequency, respectively, and $\vec{e}$ is a unit vector. The intensity of the field is given by

$$I = \varepsilon_0 c E^2 = I_h + I_b + I_f + \mathrm{cc}, \tag{3.32}$$

where

$$I_h = \varepsilon_0 c \frac{\left(\omega_0^2 |A_0|^2 + \omega_1^2 |A_1|^2\right)}{4}, \tag{3.33}$$

$$I_b = \varepsilon_0 c \frac{\omega_0 \omega_1 A_0^* A_1 e^{-i(\varphi_0 - \varphi_1)}}{2}, \tag{3.34}$$

$$I_f = -\varepsilon_0 c \frac{\left(\omega_0^2 A_0^2 e^{2i\varphi_0} + \omega_1^2 A_1^2 e^{2i\varphi_1} + 2\omega_0\omega_1 A_0 A_1 e^{i(\varphi_0+\varphi_1)}\right)}{4}, \tag{3.35}$$

and cc denotes the complex conjugate. I_h depends weakly on time and space, I_b depends weakly on time but strongly on space, and I_f represents fast oscillations. By assuming that I_f contributes negligibly to the ionisation dynamics, the modulated part of the electron number density evolves as

$$\frac{\partial n_b}{\partial t} = \eta I_b + \mathrm{cc}, \tag{3.36}$$

where η is a constant determined by the rate of ionisation, which depends on the ionisation mechanism (multiphoton, tunnelling, etc.) and the species being ionised. By taking $t = 0$ as the time at which ionisation begins and assuming that the initial wave amplitudes do not vary, the electron spatial profile is given by

$$n_b(\vec{r}, t) = i\eta \frac{\left(I_b(\vec{r}, t) - I_b(\vec{r}, 0)\right)}{\omega_1 - \omega_0} + \mathrm{cc}. \tag{3.37}$$

3.2.2 Scattering of laser pulses from ionisation-induced gratings

Free electrons are accelerated by the beat wave field, thus driving a current density

$$j_b = \frac{-e^2 n_b A}{m_e}. \tag{3.38}$$

To determine the self-consistent effect of this current on the fields driving the ionisation, consider the field denoted 1 to be a 'probe'.[6] The phase values with wavevector $\vec{k} = \vec{k}_1$ are $\varphi = \varphi_1$ and $\varphi = \varphi_{1,0} + \varphi_{0,0} - \mathrm{i}\varphi_0 = \varphi_1 + (\omega_1 - \omega_0)\,t$, where $\varphi_{0,0}$ and $\varphi_{1,0}$ are the vacuum phases of the pump and probe, respectively. The corresponding current density is

$$j_1 = \frac{-\mathrm{i}\eta e^2 \omega_0 \omega_1 \left|A_0\right|^2 A_{1,0}\left(1 - \mathrm{e}^{\mathrm{i}(\omega_1 - \omega_0)t}\right)}{4 m_e \left(\omega_1 - \omega_0\right)}. \tag{3.39}$$

The probe amplitude therefore evolves according to

$$\frac{\mathrm{d}A_1}{\mathrm{d}t} = \frac{\mathrm{i} j_1}{2\varepsilon_0 \omega_1}, \tag{3.40}$$

and the intensity follows

$$\frac{\mathrm{d}\left|A_1\right|^2}{\mathrm{d}t} \approx \frac{\eta e^2 \omega_0 \left|A_{0,0} A_{1,0}\right|^2 \left(1 - \mathrm{e}^{\mathrm{i}(\omega_1 - \omega_0)t}\right)}{8\varepsilon_0 m_e \left(\omega_1 - \omega_0\right)} + \mathrm{cc}. \tag{3.41}$$

The temporal evolution of the rate of change of the probe intensity is shown in Fig. 3.14 for various values of frequency with Hartree atomic units ($\varepsilon_0 = e = m_e = 1$) and $\eta = 1$, $A_{0,0} = 1$, $A_{1,0} = 0.1$ and $\omega_0 = 1$. The energy in the probe can be seen to change in a step-wise fashion. The less detuned the probe frequency is from that of the pump, the slower the rate of change of intensity but the greater the energy transfer. The $\omega_1 = 0.95$ line shows energy transfer from the probe to the pump in the case where the probe frequency is lower than the pump frequency.

This is a similar mechanism to Raman scattering, but with several key differences. Most notably, scattering occurs $\pi/2$ out of phase with Raman, which results in energy flowing *from* the lower frequency wave instead of into it. The model neglects any

[6] Often called the 'seed' in Raman or Brillouin amplification studies.

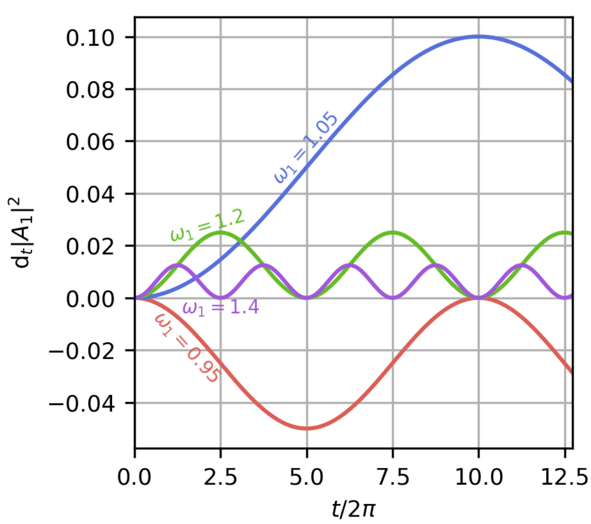

Figure 3.14: Evolution of the rate of change of probe intensity during scattering from an evolving ionisation grating for varying values of probe frequency.

contribution to the currents driven by restoring forces that are present at the edges of the grating planes, but these effects are thought to be relatively small compared to the current due to charge creation at the edges.

The Raman process occurs *ad infinitum* in theory, whilst this scattering process ceases at saturation, i.e. when the medium is totally ionised. This occurs when the ionisation front of the expanding side of the grating planes reaches the neighbouring static boundary between ionised and unionised gas. Spatial number density gratings will exist beyond saturation if the driving fields persist, but in this case these density gratings are not by ionisation, but by the ponderomotive force of the beat wave. The number density will therefore peak at the nodes of the beat wave, which is $\pi/2$ out of phase with the ionisation grating.

For degenerate frequencies,

$$\frac{\mathrm{d}A_1}{\mathrm{d}t} \approx \frac{-\mathrm{i}\eta e^2\omega_0 \left|A_{0,0}\right|^2 A_{1,0}}{8\varepsilon_0 m_e}. \tag{3.42}$$

In this case, the phase of the probe pulse is altered but negligible energy transfer occurs between electromagnetic fields.

3.2.3 Numerical investigation of the ionisation grating

A reduced 2-dimensional particle-in-cell simulation model has been devised to investigate the ionisation grating and associated scattering processes, for use with the EPOCH code. A schematic of the model is shown in Fig. 3.15. A slab of neutral hydrogen gas with $10\,\mu\text{m} \times 10\,\mu\text{m}$ spatial extent and homogeneous number density $n_0 = 6 \times 10^{19}\,\text{cm}^{-3}$ is placed in the simulation window. A pair of counterpropagating, degenerate pump pulses (denoted by the subscript 0) are launched from the x-boundaries. They have quasi-flat-top spatial field envelope profiles given by a super-Gaussian function:

$$\mathcal{E}(y) = \mathcal{E}_0 \exp\left(-\left(\frac{y - y_{0,0}}{w_0}\right)^{10}\right), \tag{3.43}$$

where $y_{0,0}$ is equal to the y-coordinate of the centre of the gas slab and w_0 is 0.6 times the y-directional length of the gas slab. Both pumps are linearly polarised with electric fields in the z-direction and are continuous in time. A probe pulse that spans the width of the simulation window in x is launched from the lower y-boundary. It is timed to reach the closest edge of the gas slab as the pump fronts reach the opposite edge of the gas slab. The probe is linearly polarised with equal electric field components in the x- and z-directions[7] and has a quasi-flat-top temporal field envelope given by

$$\mathcal{E}(t) = \mathcal{E}_0 \exp\left(-\left(\frac{t - t_{1,0}}{\tau_{w,1}}\right)^{20}\right), \tag{3.44}$$

where $\tau_{w,1} = 25\,\text{fs}$. After passing through the gas, the probe enters a region of vacuum where its fields can be diagnosed. Two regions of interest, A and B, are defined within this diagnostic space. Region A encompasses the space occupied by the probe in the case where there is no scattered trailing radiation and is used to diagnose any change to the probe fields by the interaction. Region B is the space behind the probe reaching to the edge of the gas slab and is used to measure any fields scattered into the probe direction after the probe itself has passed.

Two pump pulses are used to remain consistent with the three-beam pump-probe

[7] To be comparable to the experiment configuration described in Ch. 4.

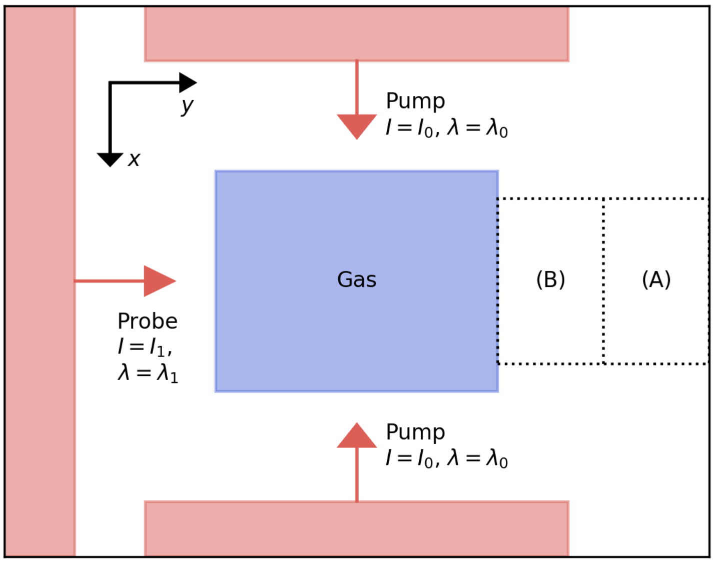

Figure 3.15: Schematic of the reduced ionisation grating simulation model. After passing through the gas/plasma, the probe enters a region of vacuum for diagnosis. Regions (A) and (B) are described in the main text.

set up described in Sec. 3.1 and the experiment described in Ch. 4. Results from a single-pump layout are not fundamentally different.

A parameter scan is performed to investigate the effect of varying pump pulse wavelength and intensity on the scattering process. The probe intensity and wavelength are fixed at $1 \times 10^{13}\,\mathrm{W\,cm^{-2}}$ and 800 nm, respectively. A 5500-point grid scan over the pump intensity and wavelength is performed in the range $1 \times 10^{13} - 5 \times 10^{15}\,\mathrm{W\,cm^{-2}}$ and 740-860 nm, respectively, with 100 logarithmically spaced points in intensity and 55 linearly spaced points in wavelength. Each simulation employs a cell size of 20 nm with initially 32 macroparticles per cell. A simulation file for one of the coordinates of the parameter scan is given in Appx. C.3.

The electron number density 50 fs after the probe front reaches the lower boundary of the gas is shown in the left column of plots in Fig. 3.16 for simulations with $\lambda_0 =$ 780 nm (upper), 800 nm (middle), and 820 nm (lower) and $I_1 = 5.13 \times 10^{13}\,\mathrm{W\,cm^{-2}}$. A $\sim$45° grating formed by the beat of the probe with both pump beams is faintly visible in each case, superimposed on the grating with planes in the y-direction due to the interaction of the pumps. The column of plots on the right of Fig. 3.16 shows the absolute value of the logarithm of the 2-dimensional Fourier transform of the corresponding electron number density profile as a function of wavenumber. The $\lambda_1 k_{x,y} = 1$ lines are also shown in each plot. The signal due to the grating formed by the overlapping pump beams at $\lambda_1 k_x \approx 2$, $\lambda_1 k_y = 0$ has the greatest amplitude due to the strength of the pump pulses. The $\sim 45^\circ$ signal due to the grating created by the probe beat with the pumps is clearly visible at $\lambda_1 k_x \simeq \lambda_1 k_y \approx 1$. The location of the harmonic is slightly detuned from $\lambda_1 k_x = \lambda_1 k_y = 1$ for two reasons. Firstly, the normalisation of the wavenumber is to the wavelength of the probe in vacuum ($\lambda_1 = 800\,\mathrm{nm}$). However, the wavelength of the fields in the plasma is modified by the refractive index. This effect is expected to be small due to the relatively low plasma density and complicated by the inhomogeneity of the electron number density. The dominant effect contributing to the detuning is the wavelength of the pump beams. This can be clearly seen in the shifting of the signal near $\lambda_1 k_x \approx 2$, $\lambda_1 k_y = 0$.

Measuring the probe electric fields after the interaction is particularly elucidating. Such measurements are presented in Figs. 3.17-3.19 for $I_0 = 5.11 \times 10^{13}\,\mathrm{W\,cm^{-2}}$ and $\lambda_0 = 780$, 800, 820 nm, respectively. The units of the spatial axes are shown relative to the lower edge of region B, $y_{b,0}$. Panel **a** of each figure shows the x-directional electric field of the probe, which has no common component with the pump beams. The electric field envelope, found by taking the absolute value of the Hilbert transformed signal [256],[8] is also shown. Regardless of the pump wavelength and intensity, the probe E_x fields remain unmodified by the interaction. Panels **b** show the z-directional electric field of the probe – which is in the common vector direction with the pump beams – and its envelope. Here, the effects of the ionisation grating are evident. In region A (see Fig. 3.15), which is on the right of the dividing line in Figs. 3.17-3.19 **a&b**, the electric fields of the probe can be seen to be modified by the interaction depending on the detuning between the pump and probe wavelengths. For $\lambda_0 = 780\,\mathrm{nm}$ (Fig. 3.17) energy is drained from the probe while for $\lambda_0 = 820\,\mathrm{nm}$ (Fig. 3.19) energy is transferred from the pump beams to the probe, in line with predictions of the model laid out in Sec. 3.2.2. No net energy is transferred when the frequencies are the same (Fig. 3.18).

[8]The Hilbert transform was calculated using the 'hilbert' function [257] of the signal module of SciPy version 1.7.1.

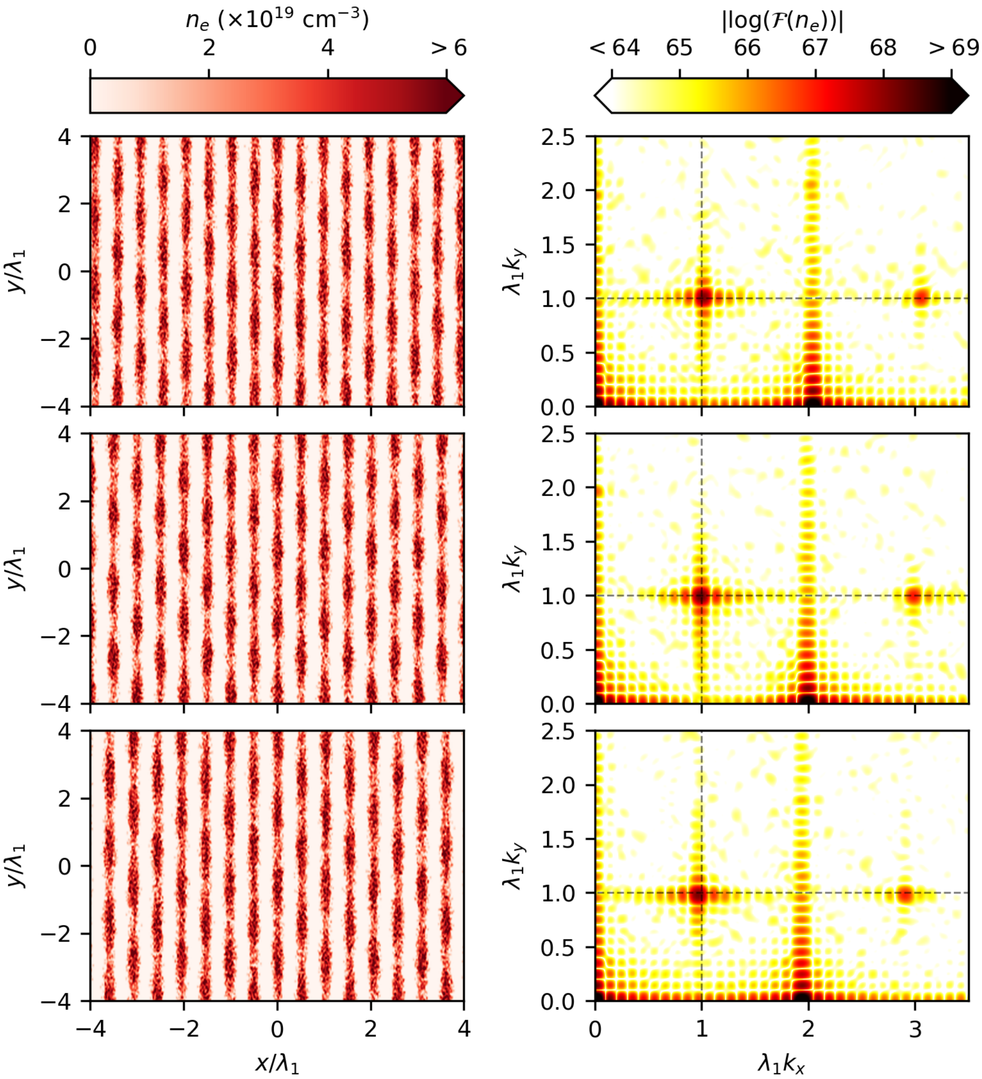

Figure 3.16: Electron number density profile (left) and its Fourier transform (right) during a three-beam ionisation grating interaction. The first, second and third row has $\lambda_0 = 780\,\text{nm}$, $800\,\text{nm}$, $820\,\text{nm}$, respectively.

The fields in region B (left of the dividing line) are those of the pump specularly scattered into the probe propagation direction by the quasi-static[9] ionisation grating left behind after the probe ceases interacting with the gas/plasma. The power spectrum of the fields in regions A and B are shown in panels **d** and **c**, respectively, for the z-(solid red) and x-directional (dashed blue, where present) field components, calculated using the Fourier transform of the signal. Panels **c** show clearly that the spectrum of the signal in region B is centred around the wavelength of the pump beams, indicating that the signal is indeed due to scattering of the pumps by the residual ionisation grating. The power spectrum of the signal in region A, shown in panels **d**, reveal very little modification of the probe spectrum by the interaction in either the x- or z-directional fields. The exception is slight blueshifting of the z-directional electric field in the degenerate frequency case (Fig. 3.18**d**), while the x-directional field remains unmodified.

Eqn. (3.41) predicts oscillating rates of change of the intensity of the probe during interaction with an evolving ionisation grating, which is also shown in Fig. 3.14. This behaviour is reproduced in the simulations and shown in Fig. 3.20, where the magnitudes of the analytic signals of the z-component of the probe electric field (i.e., the field envelopes), $|E_{a,z}|$, in region A are shown for various values of λ_0, normalised to the initial values, $|E_{a,z,0}|$. Panel **a** shows the envelope for simulations where $\lambda_0 < \lambda_1$ and **b** where $\lambda_0 > \lambda_1$. In all cases energy flows from the wave with lower frequency to the wave with higher frequency, which results in depletion of the probe for $\lambda_0 < \lambda_1$ and amplification of the probe for $\lambda_0 > \lambda_1$. The oscillatory nature of the scattering process is also evident, with the greater detuning of frequency between the two waves resulting in a higher frequency of the modulated probe envelope. Greater detuning dampens the peak modulation. For instance, when $\lambda_0 = 1.025\lambda_1$, the peak amplitude of the probe electric field envelope is $\sim 1.35|E_{a,1,0}|$, whereas it is only $\sim 1.25|E_{a,1,0}|$ when $\lambda_0 = 1.075\lambda_1$. All of these effects are qualitatively corroborated by the model described in Sec. 3.2.2.

[9] In this fixed pump intensity parameter regime, the ionisation grating is fluctuant predominantly when all three beams are interacting in the gas/plasma. Once the probe exits the interaction region, the grating evolves only slowly as the regions of gas near the pump beat wave nodes are slowly ionised and the free plasma particles evolve in space.

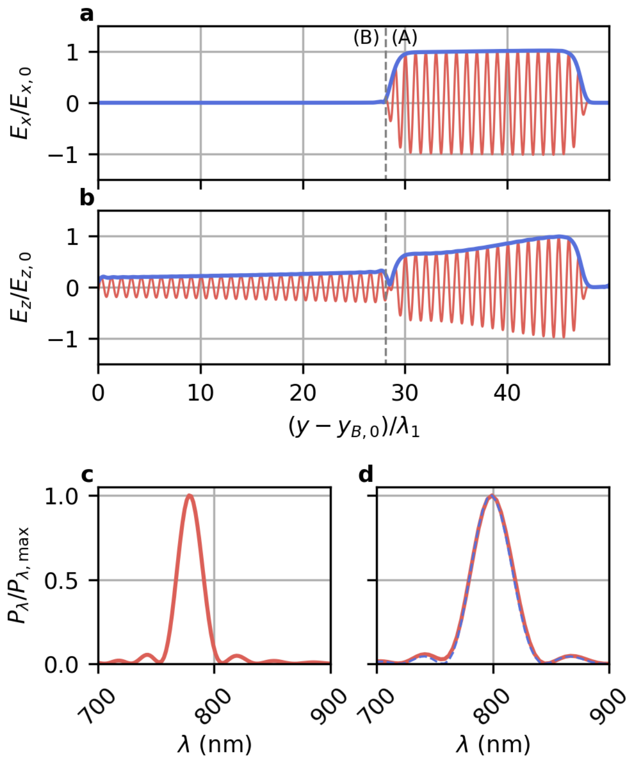

Figure 3.17: Electric fields and power spectra of the probe after interaction with an ionisation grating formed by 780 nm pumps. **a**&**b**, Electric fields and envelope in the x-(**a**) and z-direction (**b**) in the vacuum diagnostic region. Regions A and B are divided by the dashed line. **c**&**d**, Power spectra in region B (**c**) and A (**d**) of the x- and z-directional electric fields (solid red and dashed blue, respectively). The power spectrum of the E_x field is not shown for region B as there is no signal.

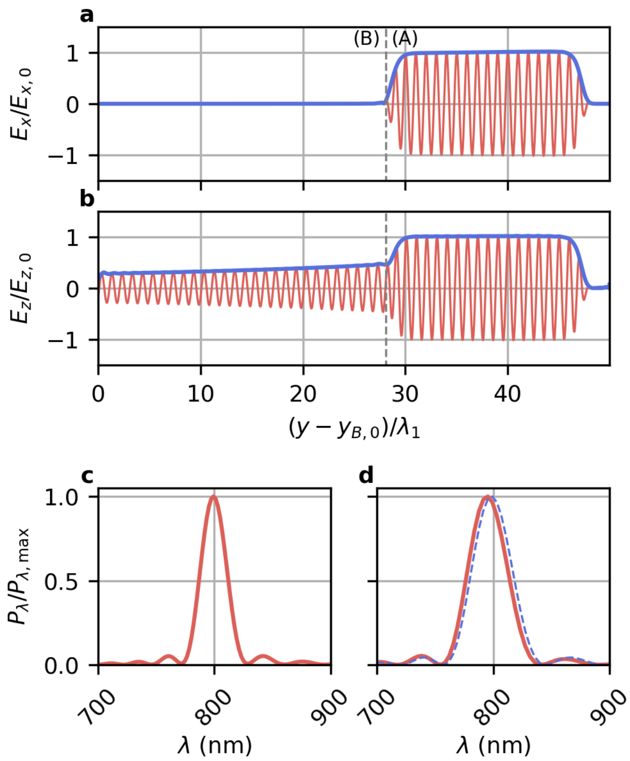

Figure 3.18: As Fig. 3.17, but for 800 nm pumps.

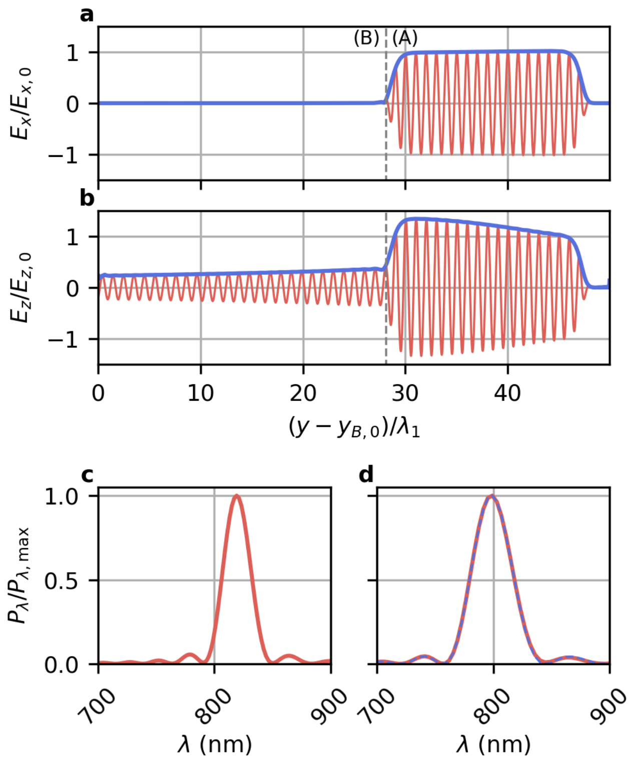

Figure 3.19: As Fig. 3.17, but for 820 nm pumps.

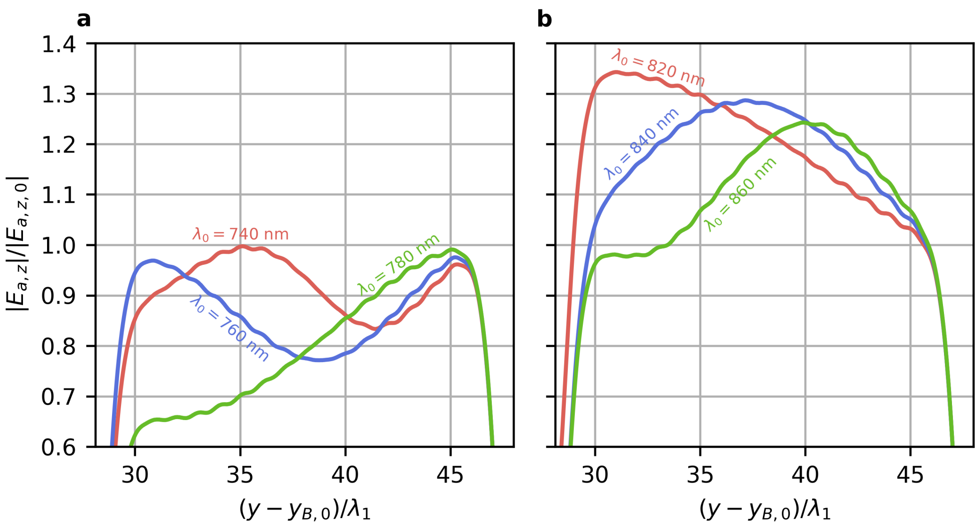

Figure 3.20: Probe z-directional electric field envelopes for values of pump wavelength $\lambda_0 < \lambda_1$ (left) and $\lambda_0 > \lambda_1$ (right).

The modification of the probe energy and scattering of the pump beams in the direction of the probe are investigated as a function of both pump intensity and pump wavelength. The energy is determined by summing the absolute values of the field energy at each grid point within the region of interest (A or B). The energy measurements in region A are normalised to the null measurement (i.e., when no pump pulses are present and the probe freely passes through the gas slab without causing any ionisation). The energy measurements in region B are arbitrary, because the quasi-static residual ionisation grating (if present) continues to scatter the pump radiation at roughly the same rate. Therefore, the energy measurement value depends on the size of the region of interest in which the fields are diagnosed. For that reason, these energy measurements are normalised to the maximum measured field sum in any individual simulation of the parameter scan.

Fig. 3.21**a** shows the variation in normalised energy in region A, U_A, with varying pump intensity, I_0, and pump wavelength, λ_0. For values of I_0 below a threshold (here, around $3 \times 10^{13}\,\mathrm{W\,cm^{-2}}$) the probe is unmodified by the interaction as the combined field strength when the pumps and probe overlap is insufficient to cause ionisation of the gas. Beyond this value, for $I_0 \lesssim 2 \times 10^{14}\,\mathrm{W\,cm^{-2}}$, the combined fields of the pumps and probe are in the range sufficient to produce a $\sim 45°$ ionisation grating. The probe is attenuated for $\lambda_0 < \lambda_1$ and amplified for $\lambda_0 > \lambda_1$, as demonstrated previously. The greatest attenuation/amplification occurs at $I_0 = 5.11 \times 10^{13}\,\mathrm{W\,cm^{-2}}$. Below this intensity the combined fields are not sufficiently high to drive a fully-formed ionisation grating for the duration of the probe. For higher intensities, the pumps are so strong that they ionise a significant fraction of the gas in the troughs of the beat wave. Indeed, for $I_0 \gtrsim 2 \times 10^{14}\,\mathrm{W\,cm^{-2}}$ the gas is fully ionised and the ionisation grating is washed out so the processes described above cannot occur. No net change in the probe energy occurs for degenerate pump-probe frequencies in the ionisation grating regime. However, after the probe has passed, the pump beams will scatter if a grating has been formed.

The energy measurements in region B, U_B, for the same parameter scan are shown in Fig. 3.21**b**. For $I_0 \lesssim 3 \times 10^{13}\,\mathrm{W\,cm^{-2}}$ there is no change in the field energy measured

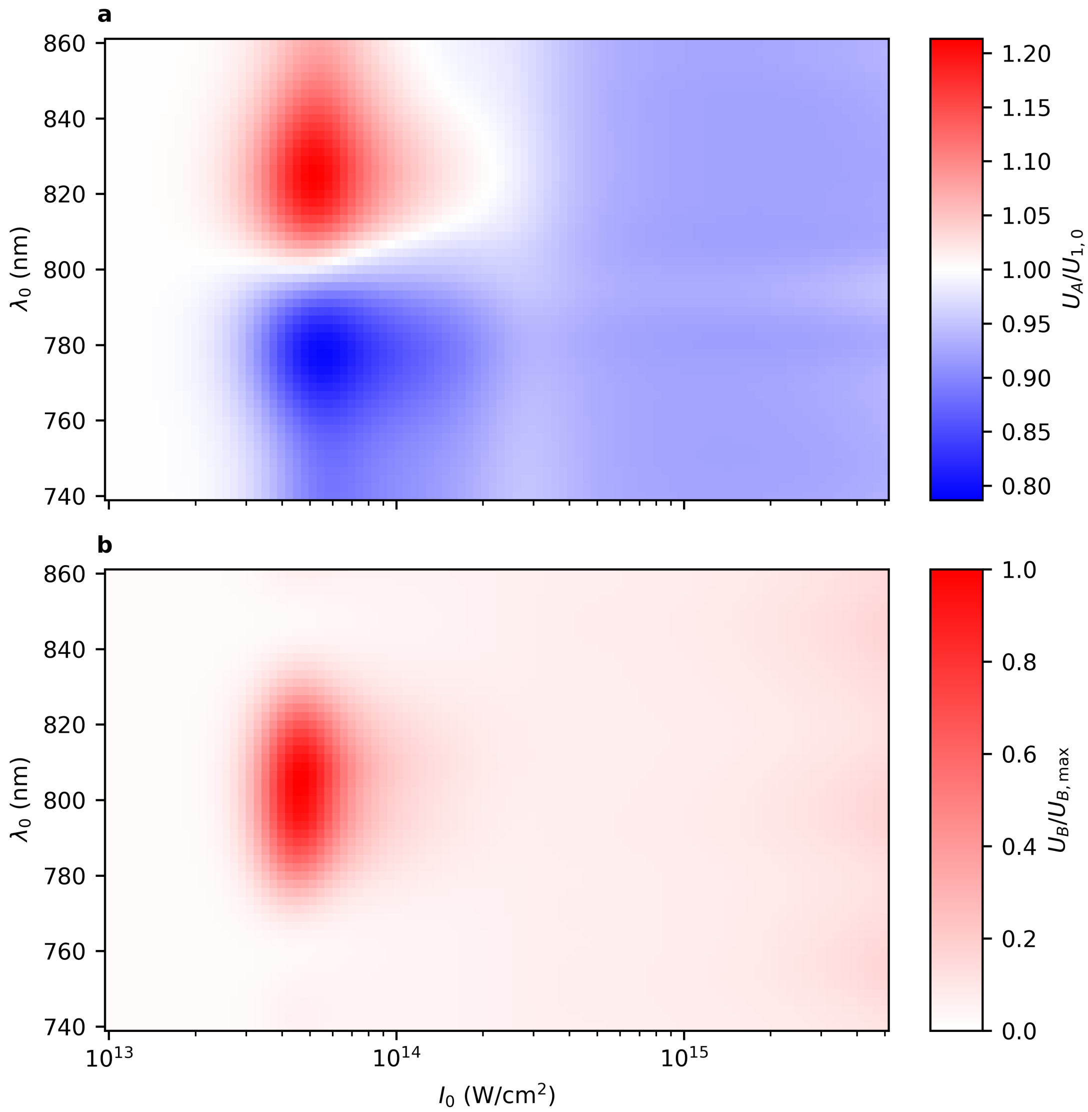

Figure 3.21: Energy in the probe electric fields and scattered pump energy into the probe direction as a function of pump intensity and wavelength. **a**, Energy measured in region A normalised to the initial probe energy. **b**, Energy measured in region B normalised to the maximum measured energy in the region in the parameter scan.

in region B. This is again due to the pump-probe field strengths being insufficient to cause ionisation and therefore no scattering of the probe occurs. Centred around $I_0 \sim 5.11 \times 10^{13}\,\mathrm{W\,cm^{-2}}$, $\lambda_0 = 800\,\mathrm{nm}$ is a signal showing scattering of the pump fields into the probe direction by the quasi-stationary residual $\sim 45°$ ionisation grating. For higher values of intensity ($\gtrsim 8 \times 10^{13}\,\mathrm{W\,cm^{-2}}$), the grating is again 'filled in' in the x-direction by the ionisation action of the pump beams and no residual grating is left to scatter the pumps. When the pump wavelengths are detuned from that of the probe, the ionisation front due to the moving beat wave fills in the grating in the y-direction. For pump and probe wavelengths detuned by $\gtrsim 30\,\mathrm{nm}$, the velocity of the beat wave is such that neighbouring y-directional grating planes meet during the evolution of the ionisation grating (i.e. during overlap of the pumps and probe). In this case, there is no $\sim 45°$ residual grating and there is again no resulting pump scattering behind the probe. In this parameter space, this occurs for $|\lambda_0 - \lambda_1| \gtrsim 30\,\mathrm{nm}$.

3.3 Interaction with both ionisation and ponderomotive gratings

Having identified and analysed the core mechanisms of structure formation, evolution and interaction with pump and probe pulses for both the ionisation and ponderomotive grating schemes, both phenomena can now be considered simultaneously. This occurs if, for example, the same pulses that are used to drive the formation of an inertial grating are also used to ionise the gas that is intended ultimately as the plasma target, while simultaneously probing with a third laser pulse.[10]

3.3.1 Description of the simulations

Particle-in-cell simulations to investigate this interaction are performed with EPOCH. A homogeneous hydrogen gas target with density $n_0 = 6 \times 10^{19}\,\mathrm{cm^{-3}}$ and spatial extent $40\,\mathrm{\mu m} \times 96\,\mathrm{\mu m}$ in $x \times y$ is initialised in the centre of the simulation window in x and with its lower edge at $y = 0$. A pump pulse with $\tau_0 = 1\,\mathrm{ps}$ full-width at half-maximum

[10] Such a configuration is explored experimentally in Ch. 4.

Gaussian temporal intensity profiles and $w_0 = 16\,\mu\text{m}$ field envelope Gaussian waist spatial profiles is sent from each x-boundary. The pump spectra are centred on $\lambda_0 = 800\,\text{nm}$ and have positive frequency chirps with bandwidth $\Delta\lambda_0 = 25\,\text{nm}$.[11] Each pump has peak intensity $I_0 = 5 \times 10^{15}\,\text{W}\,\text{cm}^{-2}$, propagates in the $\pm x$-direction and has electric fields linearly polarised in the z-direction. The pump pulses collide at the centre of the gas volume. A Gaussian spatiotemporal profile probe laser pulse with $\tau_1 = 100\,\text{fs}$ full-width at half-maximum intensity duration and $w_1 = 6.6\,\mu\text{m}$ field envelope waist is directed into the centre of the gas volume after initialisation at the lower y-boundary. The probe is unchirped, has wavelength $\lambda_1 = 800\,\text{nm}$ and is linearly polarised with equal electric field components in the x- and z-directions, i.e., it shares a common polarisation component with the pump pulses and has an orthogonal component with equal initial amplitude. It has a peak intensity $I_1 = 1 \times 10^{13}\,\text{W}\,\text{cm}^{-2}$. The simulations use $13.\dot{3}\,\text{nm}$ square cells with 8 particles per cell. The simulation parameters and notation are summarised in Table 3.2 and the input deck for one of the probe delay values can be found in Appx. C.4.

After passing through the gas/plasma, the probe enters a long region of vacuum so that its fields can be diagnosed. The simulation is terminated when the temporal centre of the probe is $75\,\mu\text{m}$ from the upper y-boundary to allow the full fields to be observed.

Several simulations are conducted, identical in every aspect except for the timing of the probe pulse. The relative delay between the temporal centres of the pump pulses reaching the spatial centre of the gas target and the temporal centre of the probe arrival at the same point is denoted $t_{1,d}$. For instance, a probe with relative delay $t_{1,d} = -1\,\text{ps}$ has an electric field envelope whose peak arrives at the centre of the gas 1 ps before the pumps. The values of probe delay simulated are $t_{1,d} \in [-1.7\,\text{ps}, 1.4\,\text{ps}]$ in steps of 0.1 ps, giving a total of 32 simulations.

[11] See Appx. A for details of the chirped Gaussian pulse definition used here.

Parameter	**Symbol**	**Value**
Plasma		
Initial density	n_0	$6 \times 10^{19}\,\mathrm{cm}^{-3}$
Species		Hydrogen
Extent		$40\,\mu\mathrm{m} \times 96\,\mu\mathrm{m}$ $(x \times y)$
Pump lasers		
Intensity	I_0	$5 \times 10^{15}\,\mathrm{W\,cm}^{-2}$
FWHM duration	τ_0	$1\,\mathrm{ps}$
Envelope waist	w_0	$16\,\mu\mathrm{m}$
Central wavelength	λ_0	$800\,\mathrm{nm}$
Bandwidth	$\Delta\lambda_0$	$25\,\mathrm{nm}$
Polarisation		Linear
E-field direction		z
Boundary		x-minimum and -maximum
Direction		$\pm x$
Probe laser		
Intensity	I_1	$1 \times 10^{13}\,\mathrm{W\,cm}^{-2}$
FWHM duration	τ_1	$100\,\mathrm{fs}$
Envelope waist	w_1	$6.6\,\mu\mathrm{m}$
Central wavelength	λ_1	$800\,\mathrm{nm}$
Polarisation		Linear
E-field direction		$\angle 45^\circ$ to $\hat{x}$ and $\hat{z}$
Boundary		y-minimum
Direction		$+y$
Simulation		
Cell size		$13.\dot{3}\,\mathrm{nm} \times 13.\dot{3}\,\mathrm{nm}$
Initial particles per cell		8
Domain size		$50\,\mu\mathrm{m} \times 316\,\mu\mathrm{m}$ $(x \times y)$

Table 3.2: Simulation parameters for the ionisation and inertial grating study.

3.3.2 Energy in the probe

The integral of the probe electric field amplitude is measured following the interaction as a way of determining the energy gain.

Simulations with probe delay values in the range $t_{1,d} \in [-0.5\,\text{ps}, 0.4\,\text{ps}]$ contained electric fields in the probe vacuum diagnostic region that extends from the gas/plasma. In these cases, the simulation is restarted after the diagnostic snapshot described above and these fields are allowed to evolve for a time sufficient for light to propagate from the edge of the gas to the upper y-boundary of the simulation window. This allows the total energy in the probe-directed fields to be measured. Fig. 3.22 shows a lineout of the x- and z-directional electric field envelopes through $x = 0$ for $t_{1,d} = -0.4\,\text{ps}$. The amplitude of the signal calculated from the data in the second simulation output dump has been concatenated onto the first, with the join indicated by the vertical dashed line. In this case, ∼9.6% of the energy in the z-directional fields is contained in the region that would have been missed if the simulation restart and field concatenation had not been performed.

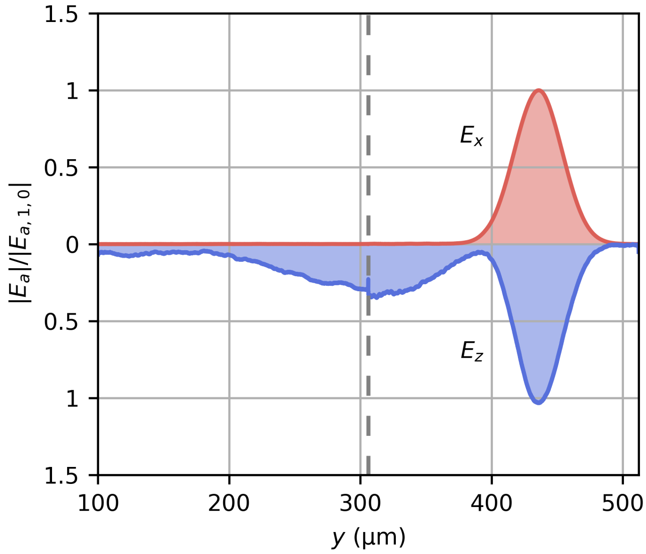

Figure 3.22: Probe x- and z-directional electric field envelopes after the interaction at $t_{1,d} = -0.4\,\text{ps}$. Field amplitude values are normalised to the initial peak amplitude in one component. Note the symmetric vertical axes. The dashed line indicates the join between the fields of the two simulation dumps.

Fig. 3.23 shows the electric field energy in the x- and z-directional components in the diagnostic region normalised to the initial electric field energy in each orthogonal component. If the probe arrives early ($t_{1,d} \lesssim -1.4\,\mathrm{ps}$) there is no change in the measured energy following the interaction due to the probe having a peak intensity below the ionisation threshold and arriving before the pumps have ramped up to an intensity beyond the same threshold. For $-1.4\,\mathrm{ps} \lesssim t_{1,d} \lesssim 0.1\,\mathrm{ps}$, the energy in the z-directional electric field component in the vacuum diagnostic region is enhanced due to interaction with the ionisation grating.[12] Scattering of the pump beams from the evolving ionisation grating (described in Secs. 3.2.1 & 3.2.2) and the static ionisation grating make contributions to varying degrees, depending on the probe delay. The x-directional electric field energy is relatively unchanged for all values of $t_{1,d}$.

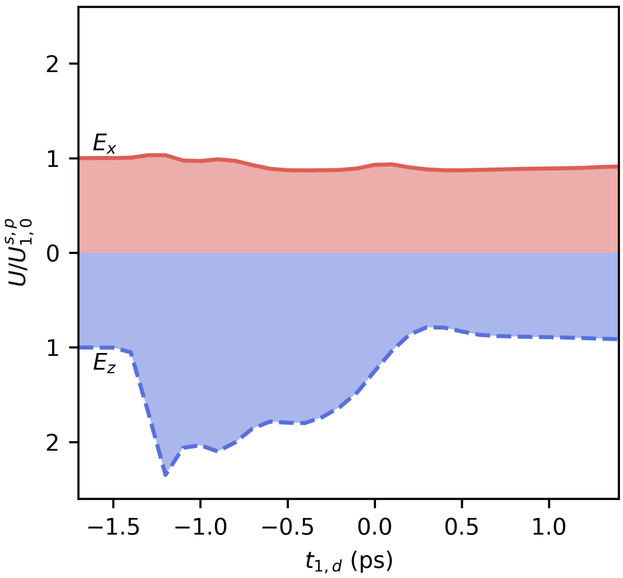

Figure 3.23: Energy in the electric fields in the vacuum diagnostic region as a function of probe delay, normalised to the initial probe energy in each orthogonal field component, $U_{1,0}^{s,p}$. The solid red line shows the energy in the x-component fields and the dashed blue line the energy in the z-component fields. The vertical axis is symmetric about zero.

Insight into which processes occur can be established from measurements of the pulse duration and peak value of the probe electric field envelope. Such measurements

[12]Further evidence of this is shown in Fig. 3.25

are shown in Fig. 3.24**a**&**b**, respectively. Both sets of measurements are determined from lineouts of the z-component of the electric field. Panel **a** shows the (weighted standard deviation) pulse duration, defined as

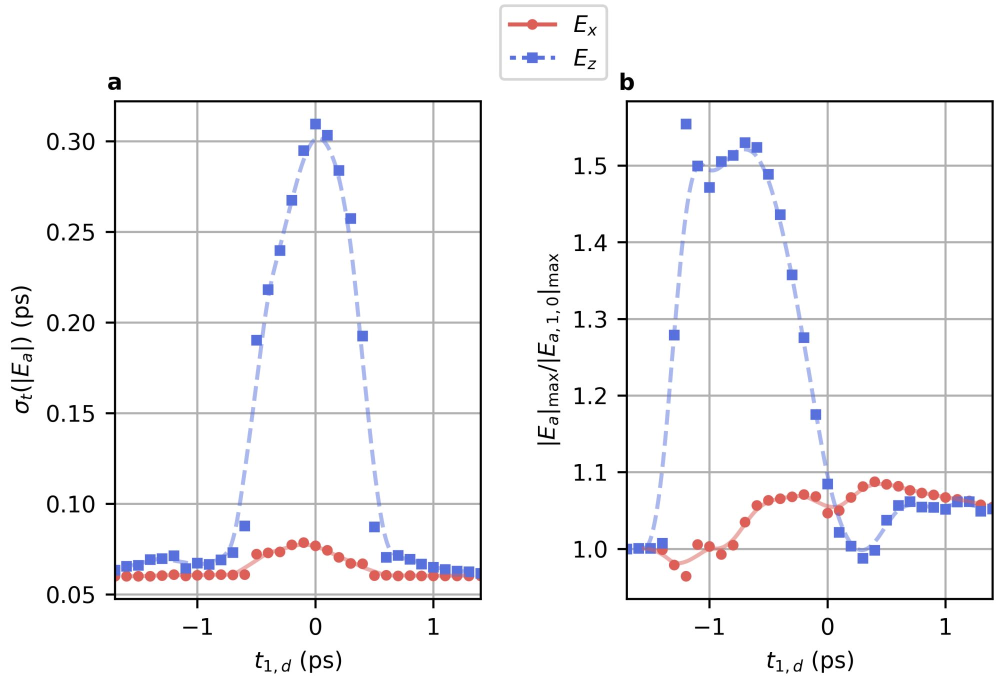

Figure 3.24: Temporal standard deviation (**a**) and peak value (**b**) of the x- (solid red line and circular markers) and z-directional (dashed blue line and square markers) electric field component envelopes in the vacuum diagnostic region as a function of probe delay.

$$\sigma_t(|E_a|) = \sqrt{\frac{\sum_{i=1}^{N} |E_a|_i \left(t_{y,i} - \bar{t_y}\right)^2}{\sum_{i=1}^{N} |E_a|_i}}, \tag{3.45}$$

where i denotes the discrete simulation grid with a total of N points, $t_{y,i} = (y_i - y_1)/c$ is the discrete spatial coordinate converted to time, and $\bar{t_y}$ is its weighted average,

$$\bar{t_y} = \frac{\sum_{i=1}^{N} \left(|E_a|_i \, t_{y,i}\right)}{\sum_{i=1}^{N} |E_a|_i}. \tag{3.46}$$

This method of measurement of the duration discards any information relating to the pulse shape but accounts for fields trailing the main part of the pulse (see, for example, Fig. 3.22), in addition to reductions in the group velocity. The peak electric field envelope values shown in panel **b** are normalised to the initial probe peak electric field value, $|E_{a,1,0}|_{\max}$. Both panels show the measurements for the x- and z-component of the electric fields with red circles and blue squares, respectively. All sets of measurements include a line (dashed for z- and solid for x-component of the fields) showing the convolution of the data with a kernel of ones after up-sampling by a factor of 100 by linear interpolation,[13] to guide the eye. The pulse duration is maximal at $t_{1,d} = 0$ and returns to unperturbed values for $t_{1,d} \approx \pm 0.6\,\text{ps}$. The peak at $t_{1,d} = 0$ is due to the pump pulses having the greatest amplitude when the probe interacts with them at this value of delay, resulting in a 45° grating forming in the wings of the pump pulses, which persists for much of the remainder of the interaction. For values of $-0.6\,\text{ps} \lesssim t_{1,d} < 0\,\text{ps}$, the 45° grating is formed but is also washed out by the pump pulses that continue to ramp up. In this case, the limiting factor of the scattered radiation (and therefore the measured pulse duration) is the amount of pump radiation that is scattered before the 45° grating is washed out and the probe pulse has passed, thus preventing further formation of a 45° grating. For $0\,\text{ps} < t_{1,d} \lesssim 0.6\,\text{ps}$, any 45° scatterer formed by the three-beam interaction persists as the pumps are diminishing in amplitude. However, the amount of scattered pump radiation also decreases with increasing $t_{1,d}$ as the pump pulses have lower amplitude when interacting with a formed grating.

Amplification of the probe fields during interaction with the pump pulses by the process described in Sec. 3.2.2 leads to the higher values of $|E_a|_{\max}$ shown in panel **b** of Fig. 3.24 for $-1.4\,\text{ps} \lesssim t_{1,d} < 0\,\text{ps}$, due to the pumps having a negatively detuned frequency relative to the probe at the time of interaction when the probe arrives before the peak of the pumps.

A profile of the envelope of the z-components of the electric field through $x = 0$ in the vacuum diagnostic region is shown by the solid line and shaded region in Fig. 3.25 for $t_{1,d} \in [-0.4\,\text{ps}, 0.4\,\text{ps}]$ and a 0.1 ps step size. Scattering of the pump pulses by the static 45° grating into the region behind the probe pulse is evident in each snapshot, with the greatest amount of field scattering occurring for $t_{1,d} = 0\,\text{ps}$. The noisy red line shows the instantaneous wavelength of the z-directional electric field determined by the angle

[13] This is equivalent to a moving average.

of the analytic signal (determined using the Hilbert transform) from the real axis on the complex plane. These values are calculated when the field amplitude envelope exceeds $0.05\,|E_{a,1,0}|$, indicated by the dotted black line. The signal to noise ratio is deemed too low to give a meaningful wavelength measurement below this threshold. In the region behind the probe the instantaneous wavelength exhibits positive linear frequency chirp and shows good agreement with the corresponding value of the instantaneous wavelength of the pump pulses calculated analytically from the initial conditions and shown in dashed purple. This is further evidence of the signal trailing the main part of the pulse due to scattered pump pulse radiation from the static residual 45° grating.

3.3.3 Determining the phase shift

As discussed in Sec. 3.1.2, plasma density gratings are able to induce a relative phase shift between orthogonal electric field components of probing laser pulses with a component of its vector propagation perpendicular to that of the pump pulses. In a scenario ideal for the use of a plasma density grating as a waveplate for the manipulation of the phase of an intense, ultrashort laser pulse, the probe encounters a 'clean' plasma grating that can be well described by the model presented in Sec. 3.1.2. This is not the case for the interaction discussed in these sections due to the presence of ionisation gratings (at various degrees of formation) and the quasi-one-dimensional shape of the plasma grating structure. Furthermore, the probe pulse has a finite bandwidth and each spectral component will be modified differently. Thus, numerical methods are required to determine the phase shift at each simulated value of probe delay.

The phase shift between the two perpendicular electric field components of the probe pulse induced by the interaction is calculated by measuring the fields in the vacuum diagnostic region. For each delay value, a profile is taken through the x- and z-components of the electric field propagating in the y-direction at $x = 0$. The fast Fourier transform of the signal is calculated using the `fft` method [258] of NumPy [259] version 1.21 and its complex phase determined for each frequency bin. Linear interpolation is performed to find the spectral phase of each wave at a given wavelength (750 nm, 800 nm, and 850 nm). The phase shift is calculated by subtracting the inter-

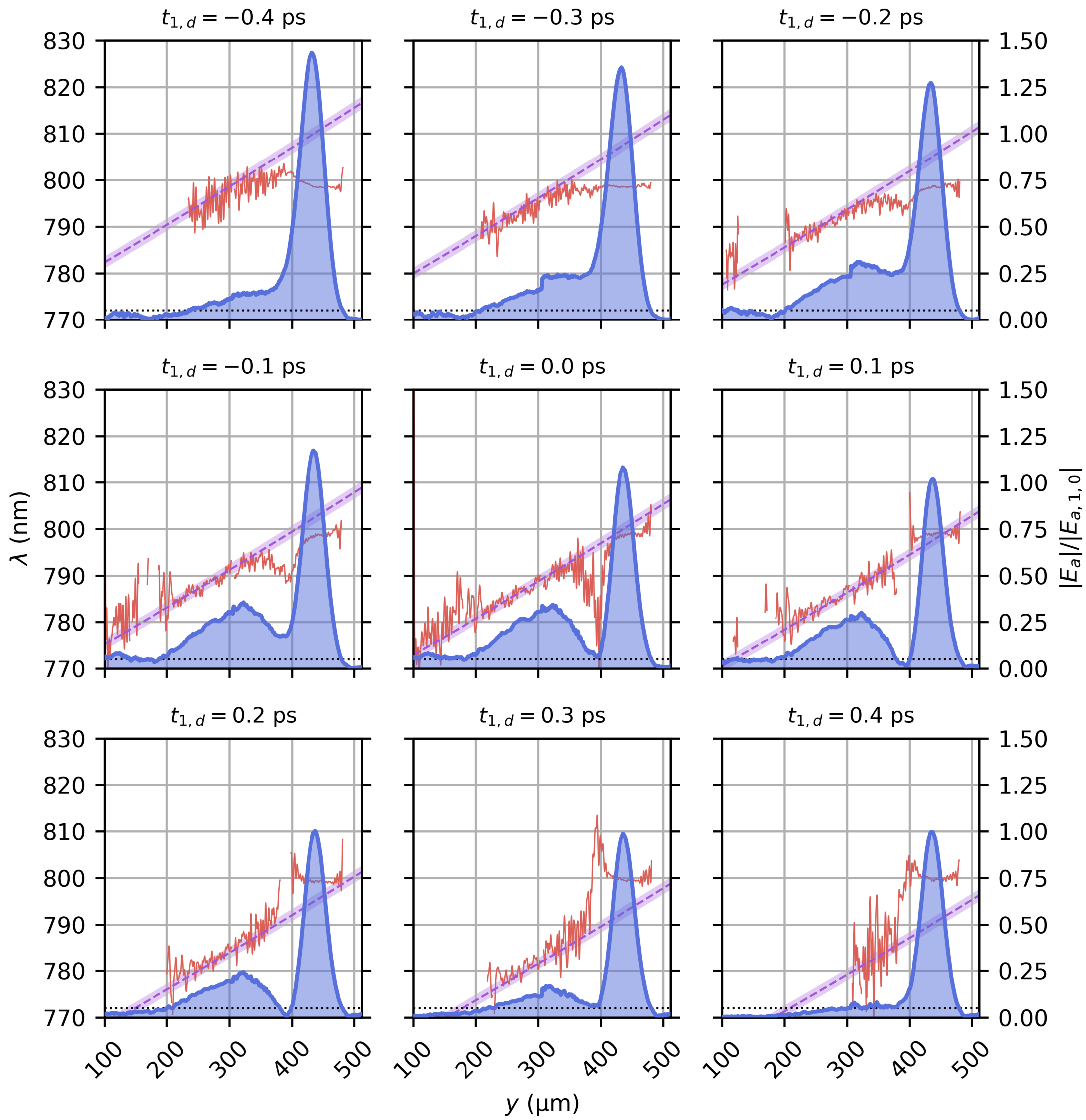

Figure 3.25: Snapshots of z-components of the electric field data in the diagnostic region showing the dependence on the probe delay. The solid blue shaded region shows the electric field envelope and corresponds to the right axis of each panel. The solid red line shows the instantaneous wavelength of the electric fields, with values indicated on the left axes. The purple dashed line is the instantaneous wavelength of the pumps in the centre of the gas at the time corresponding to the probe position. The surrounding shaded area is the instantaneous wavelength at $\pm w_0$. The dotted black line indicates the threshold below which the signal to noise ratio was too low to give a meaningful instantaneous wavelength measurement.

polated phase of the x-directional wave at a given wavelength from the phase of the corresponding z-directional wave,

$$\Gamma|_\lambda = \phi_z|_\lambda - \phi_x|_\lambda. \tag{3.47}$$

The phase shift of the probe is shown as a function of delay in Fig. 3.26 for the three values of wavelength discussed. A moving average line accompanies each set of data, which is calculated using the method described in Sec. 3.3.2. The positive phase shift for $t_{1,d} \gtrsim 0\,\mathrm{ps}$ is due to the inertial grating. The phase shift builds up rapidly as the charged plasma species particles bunch inertially in the ponderomotive troughs and decreases once the structure begins to decay. The negative phase shift in the range $-1.4\,\mathrm{ps} \lesssim t_{1,d} \lesssim -0.1\,\mathrm{ps}$ is predominantly due to the interaction with the ionisation grating.[14] Longer wavelength waves experience a greater phase shift than the shorter wavelength waves in both cases.

3.3.4 Predictions of experimentally observed measurements

The method for predicting experimentally observable quantities is more involved than those described thus far and must account for the phase shift between the orthogonal field components, any increase in the probe field amplitude during interaction with an evolving ionisation grating, any scattering of the pump pulses behind the probe due to a 45° grating, and the experimental apparatus used to measure the state of the radiation after the interaction.

A common method for measuring the polarisation of light is through the use of a polarising beam splitter such as a Wollaston prism, Rochon prism, Glan-Foucault prism, etc. Such beam splitters are composed of birefringent materials and produce two orthogonally polarised beams. The energy in each orthogonal field component can be measured by, for instance, summing the pixel values of an image of each beam formed on a suitable camera chip.

Jones calculus [260] is used to analyse the polarisation form of laser light as it

[14]This can be understood by considering the refractive index, η, of the layers in the stratified media (see Fig. 3.10) – in a ponderomotive grating $\eta_a < \eta_b < 1$, while in an ionisation grating $\eta_b < 1 < \eta_a$.

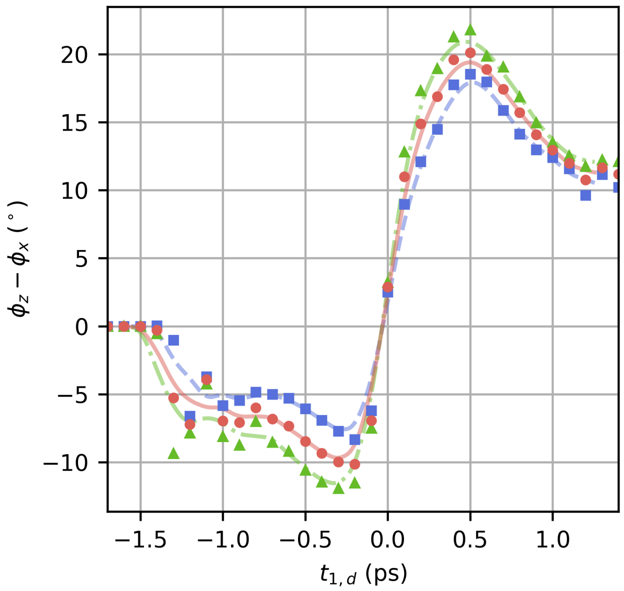

Figure 3.26: Phase shift of the probe in degrees as a function of delay for 800 nm (red circles and solid line), 750 nm (blue squares and dashed line) and 850 nm (green triangles and dot-dashed line) light.

propagates through a model experimental system. First, the power spectra of the orthogonal fields after the interaction is determined by taking

$$P_{\lambda,x} = |\mathcal{F}(E_x)|^2$$
$$P_{\lambda,z} = |\mathcal{F}(E_z)|^2 , \tag{3.48}$$

where $\mathcal{F}$ denotes the Fourier transform. The total power spectrum is

$$P_\lambda = P_{\lambda,x} + P_{\lambda,z}. \tag{3.49}$$

For these measurements, the probe is considered initially linearly polarised with Jones vector

$$I = \begin{pmatrix} 0 \\ 1 \end{pmatrix} , \tag{3.50}$$

conventionally referred to as vertical polarisation. The probe then passes through a quarter-wave plate with fast axis azimuth $\theta = 45°$, which has a Jones matrix given by [261]

$$Q = \mathrm{e}^{-\frac{\mathrm{i}\pi}{4}} \begin{pmatrix} \cos^2\theta + \mathrm{i}\sin^2\theta & (1-\mathrm{i})\sin\theta\cos\theta \\ (1-\mathrm{i})\sin\theta\cos\theta & \sin^2\theta + \mathrm{i}\cos^2\theta \end{pmatrix}. \tag{3.51}$$

The probe may gain or lose energy within the plasma. This is accounted for by the Jones matrix

$$A = \begin{pmatrix} G_x^{1/2} & 0 \\ 0 & G_z^{1/2} \end{pmatrix}, \tag{3.52}$$

where G_x and G_z are the energy gain factors in the x- and z-directional electric field components of the probe, respectively, for energy in each probe field component, $U_{A,x}$ and $U_{A,z}$, calculated using the method in Appx. B. The phase shift due to interaction with a plasma structure is described by

$$R_\lambda = \begin{bmatrix} \exp\left(\frac{\mathrm{i}\Gamma_\lambda}{2}\right) & 0 \\ 0 & \exp\left(\frac{-\mathrm{i}\Gamma_\lambda}{2}\right) \end{bmatrix}, \tag{3.53}$$

where Γ_λ is the relative phase imparted by the interaction measured using the Fourier transform method described in Sec. 3.3.3 (see in particular Eqn. (3.47)), which varies with wavelength. The probe then passes through another quarter-wave plate with the same fast axis azimuth as the first. The final polarisation form of each spectral component of the field resulting from the interaction with this beamline is given by

$$\begin{aligned} F_\lambda &= QR_\lambda AQI \\ &= T_\lambda I, \end{aligned} \tag{3.54}$$

where $T_\lambda = QR_\lambda AQ$ is the transform matrix.

The calculation using Eqn. (3.54) is performed for every discrete spectral component, where all elements forming T_λ are identical except for R_λ, which varies with wavelength. A single spectrally-weighted Jones vector is found by taking the average of the vectors F_λ weighted by P_λ, i.e.,

$$F = \frac{\sum_{i=1}^{N} P_{\lambda,i} F_{\lambda,i}}{\sum_{i=1}^{N} P_{\lambda,i}}, \tag{3.55}$$

for the N discrete spectral bins. Neglecting any fields trailing the probe pulse (e.g., due to scattering of the pumps from a static 45° ionisation grating), a prediction of the ratio of pixel counts on the diagnostic described above can be made:

$$\mathcal{R} = \frac{F_1}{F_0 + F_1}. \tag{3.56}$$

To account for scattering of fields behind the probe, the z-directional electric field energy in this region, $U_{B,z}$, is calculated. The ratio $\mathcal{R}$ is then corrected by

$$\mathcal{R}_c = \mathcal{R}\frac{U_{A,x} + U_{A,z}}{U_{A,x} + U_{A,z} + U_{B,z}} + \frac{1}{2}\frac{U_{B,z}}{U_{A,x} + U_{A,z} + U_{B,z}}, \tag{3.57}$$

as the z-components of the electric field is divided equally between the polarisation components when passing through the final quarter-wave plate.

The corrected ratio R_c is shown as a function of probe delay $t_{1,d}$ in Fig. 3.27. The initial steep rise is mostly due to the amplification of the probe by the interaction with the evolving ionisation grating (cf. Figs. 3.23 & 3.24**b**) as well as the negative phase shift induced by interaction with the ionisation grating (cf. Fig. 3.26). The peak around $t_{1,d} = 0\,\mathrm{ps}$ is predominantly attributable to the scattering of pump radiation into the probe direction (cf. Fig. 3.24**a**), and the signal at $t_{1,d} \gtrapprox 0.2\,\mathrm{ps}$ is due to the phase shift induced by the ponderomotive grating (cf. Fig. 3.26).

3.4 Conclusions

Two methods of forming volume plasma density gratings have been discussed – the first by intersecting counterpropagating laser pulses in pre-formed plasma to drive a ponderomotive grating, and the second by crossing laser pulses in a gas to form an ionisation grating.

In idealised slab geometry, the effect of a ponderomotive grating on a probing laser

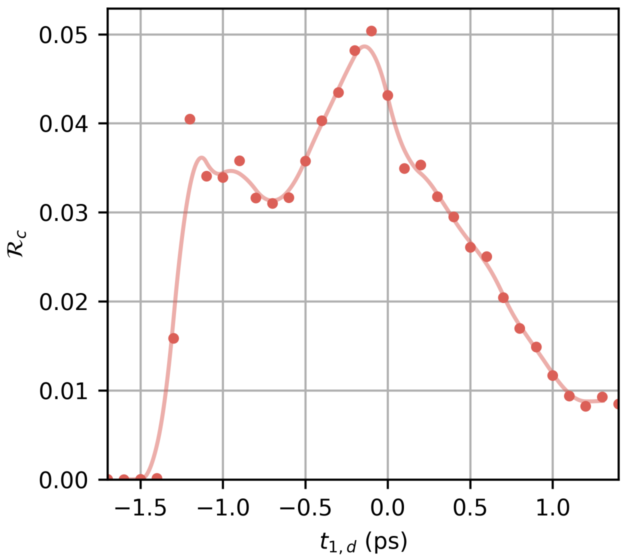

Figure 3.27: The simulated ratio R_c (see Eqn. (3.57)) as a function of delay.

pulse can be predicted by the matrix method of identifying dispersion relations of a stratified medium. These calculations may be used as a basis for designing an optical device based on a plasma density grating, although the effects of using pump pulses with more realistic far field spatial profiles (e.g. Gaussian) must be accounted for.

Ionisation gratings are also able to manipulate the fields of probing laser pulses. The two strongest effects are – transient modification of the probe electric field amplitude by an evolving grating, and scattering of pump fields into the probe direction by a residual, non-evolving grating.

Particle-in-cell simulations are performed in a realistic configuration reminiscent of the experiment described in Ch. 4, in which the pump pulses used to form a ponderomotive grating are also used to ionise the gas medium, and therefore ionisation gratings are present at certain times and degrees of pump-probe overlap. The arrangement is chosen to investigate the waveplate-like qualities of a ponderomotive plasma density grating. The ionisation grating is found to be potentially deleterious to the quality of the probe following the interaction by lengthening the pulse duration. A method, based on Jones calculus, of determining the effect of the interaction on a probing laser pulse by using existing diagnostic equipment is also introduced.

To be most useful, a future device based on this plasma optic scheme must carefully account for the effects of scattering due to ionisation gratings, or use a pre-formed plasma as the medium in which a ponderomotive grating is produced as this would eliminate all ionisation grating effects at the cost of experimental configuration complexity. Alternatively, a probe with no spectral components common to the pumps may be considered. If timed to arrive after the pump pulses have passed (which requires pump pulse durations significantly shorter than the saturation time of the ponderomotive grating if the probe is to interact with a fully-formed structure), any residual scattering of the pump pulse light into the probe direction may be filtered using common optical components. Finally, the pump pulses may be polarised such that their electric field components are orthogonal to those of the probe. Although directly-counterpropagating beam geometries are usually experimentally excluded to avoid damage to the upstream optical components, minimisation of the common pump-probe field components will reduce scattering and result in a cleaner interaction.

Chapter 4

Experimental measurements of volume plasma density gratings

This chapter describes an experiment performed using the Gemini laser system at the Rutherford Appleton Laboratory (RAL) Central Laser Facility (CLF) in September to October 2019. The goals of the experiment were to investigate the formation of a volume plasma density grating by the intersection of two nearly-counterpropagating pump laser pulses in underdense plasma, and probe it using an independent, ultrashort laser pulse, as described theoretically and investigated numerically in Sec. 3.1. The unexpected change in the energy collected by the probe diagnostics (which are presented later in the chapter) prompted a line of inquiry that ultimately led to the discovery of the novel process described in Sec. 3.2.

The experimental facilities, configuration and diagnostics are described in Sec. 4.1, and the results of a probe arrival time scan are presented and discussed in Sec. 4.2.

4.1 Methods

The equipment and facilities used for the experiment are described in the following sections. Briefly, the experiment comprises colliding two nearly-counterpropagating, almost-identical, picosecond laser pulses in a gas jet formed by a bespoke nozzle, which readily ionise the gas to form plasma and create a volume plasma density grating.

The interaction is probed by a third independent, ultrashort laser pulse. Analysis of the far field profile, spectrum, energy and polarisation enables the interaction to be comprehensively studied.

4.1.1 Gas target

A gas nozzle has been designed for use in experimental studies, which consists of a base with a hole to which a hypodermic needle is securely attached. The base, shown in Fig. 4.1, has a 5 mm chimney with a 0.82 mm cylindrical upper tube, which reduced to a 0.5 mm tube. A gauge 20 needle is inserted into the upper tube until contact is made with the lower tube and secured in place using resin filled in a conical wedge at the top of the upper chimney. The needle is trimmed to allow 5 mm extrusion from the top of the chimney. The base was originally designed to accommodate a gauge 21 needle, but machining tolerance meant a slightly larger needle has been used. The base is attached to a PeterPaul series 20 model EH22 valve and connected to a compressed gas line. Gas targets of a similar design have also been used for ion acceleration studies [262]. The valve can be pressurised with up to 100 bar of gas. CAD drawings and images of the nozzle are shown in Fig. 4.1.

The gas plume is simulated using Ansys Fluent version 18.2. In the simulation, the needle is backed with 60 bar of hydrogen or helium gas. Fig. 4.2**a** shows a slice through the hydrogen plasma plume (assuming total ionisation of the gas) 0.75 mm above the top of the needle. A measure of the width of the plume at a given height is given by

$$\sigma(r) = \left(\frac{\sum n_i \left(r_i - \mu_r\right)^2}{\sum n_i} \right), \tag{4.1}$$

where r is the radial position, $n = n(r)$ is the number density, $\mu_r = \sum n_i r_i / \sum n_i$ is the mean position weighted by number density, and the subscript i denotes the discrete nature of the data. There are very steep density gradients and a large peak number density up to $1.4 \times 10^{21}\,\mathrm{cm}^{-3}$ at 0.1 mm from the chimney opening. The profile is radially symmetric and parabolic. Fig. 4.2**b** shows the peak axial number density and plume width at varying distance from the tip of the needle. The continuous lines

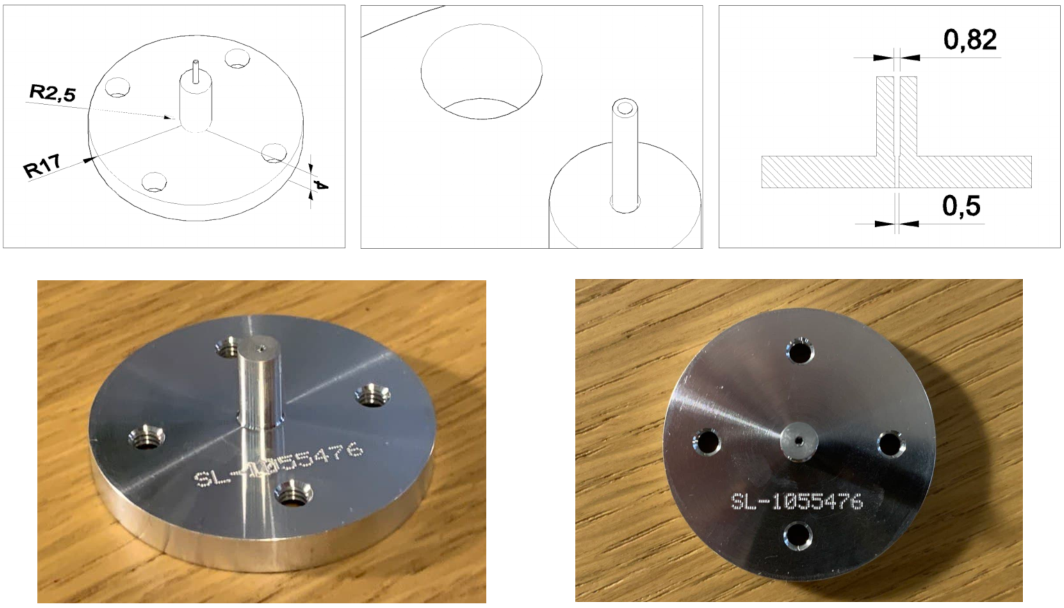

Figure 4.1: CAD drawings and images of the nozzle designed for transient plasma grating experiments. The needle is shown in the CAD drawings but not in the photographic images. Units are in mm.

through the data points are determined by cubic interpolation. The gas density is maximal at the exit of the nozzle and falls off very rapidly with distance.

The density of the plasma produced by irradiating the gas target with a high-intensity laser pulse is characterised by Raman side scattering (RSS) [12, 263, 264]. The three-wave Raman scattering interaction is described by

$$\omega_0 \simeq \omega_1 + \omega_p \tag{4.2}$$

$$\vec{k}_0 \simeq \vec{k}_1 + \vec{k}_p, \tag{4.3}$$

where ω_0 and $\vec{k}_0$ are the incident electromagnetic wave frequency and wavevector, respectively, which interacts with a plasma wave with ω_p, $\vec{k}_p$ and scatters into another electromagnetic wave with ω_1, $\vec{k}_1$. The plasma frequency (and therefore number density by Eqn. (2.55)) can be determined by measuring the scattered spectrum. The laser and Raman scattered spectrum are measured using an Ocean Optics Maya 2000Pro spectrometer, with an example spectrum shown in Fig. 4.3**a**. The laser spectrum peak

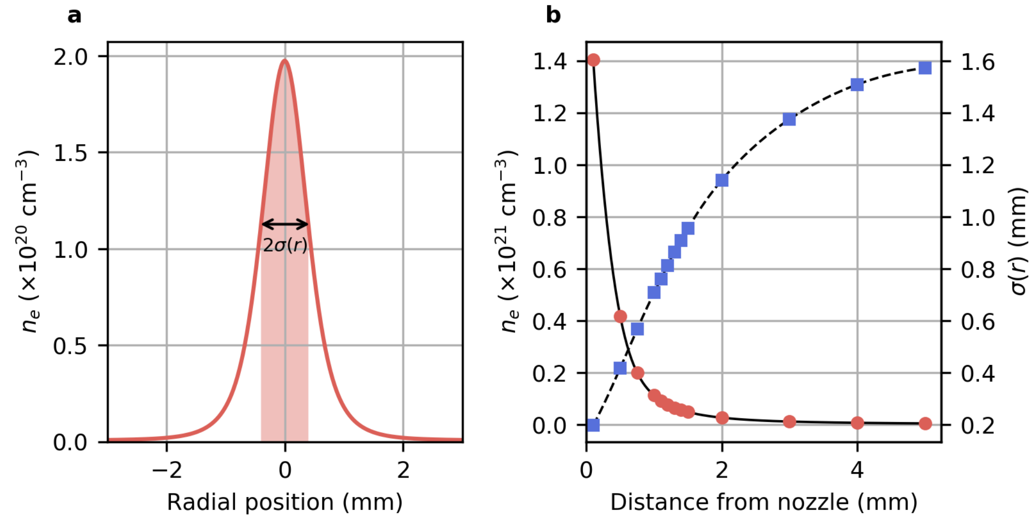

Figure 4.2: Fluid simulation results of the gas nozzle designed for plasma density grating experiments. **a**, Radial plasma density profile (assuming complete ionisation of hydrogen) of the gas plume 0.75 mm above the nozzle. **b**, Peak plasma density, which always occurs on the nozzle axis of symmetry (red circles), and plume width (defined in the text, blue squares) with varying height above the nozzle.

is close to 800 nm and the Stokes and anti-Stokes spectral components are visible. Three shots with varying backing pressure are taken to calibrate the plasma density variation. A linear response intercepting $n_e = 0$ when no gas is present is assumed, which gives the relation

$$n_e \ [\mathrm{cm}^{-3}] = 8.9 \times 10^{17} P_b \ [\mathrm{bar}] \tag{4.4}$$

for backing pressure P_b.

4.1.2 The Gemini laser facility

The experiment has been performed using the Gemini laser system [265] at the Central Laser Facility at the Rutherford Appleton Laboratory in the United Kingdom. Gemini is a dual Ti:sapphire-based system operating with 800 nm central wavelength and can provide up to 15 J laser pulses with durations down to 30 fs in two synchronised beams.

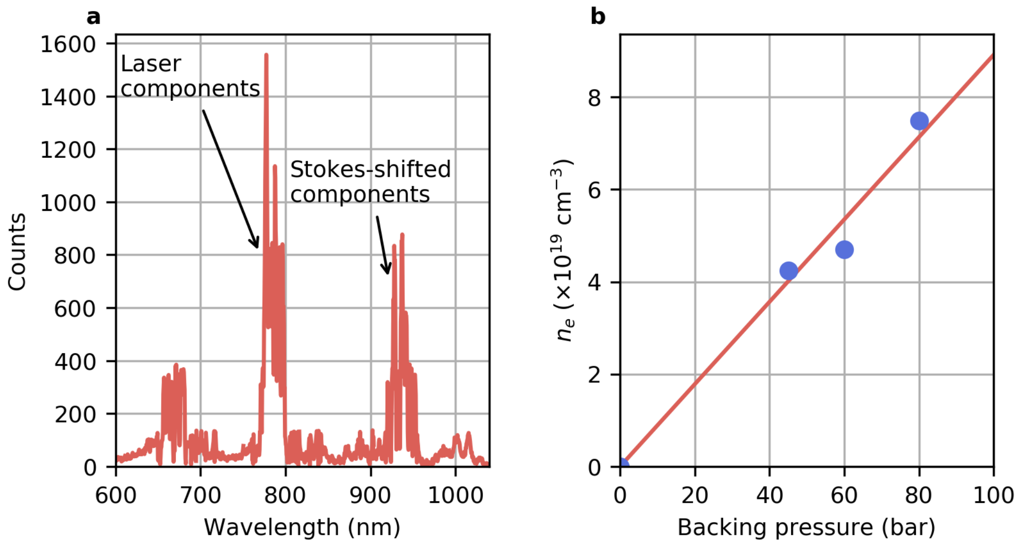

Figure 4.3: Calibration of the gas target by Raman side scattering. **a**, An example of the data produced by the spectrometer used for the calibration. The backing pressure for this shot was 60 bar and the laser beams were positioned 750 µm above the nozzle throat. The main laser spectral components are near 800 nm, and the Stokes and anti-Stokes lines are visible. **b**, The four-point calibration of the plasma density variation with backing pressure.

Pump beams

For this study, both of the beams of Gemini have been used as pump beams to create the plasma density grating. The final CPA compressor gratings in each beam arm are separated by greater than the distance for optimal compression, which introduces a positive frequency chirp to the beams and increases their pulse durations to $\tau \simeq 1\,\text{ps}$. The pulse duration and temporal shape of one of the pump beams is measured using an Amplitude Sequoia third-order cross-correlator. Raw data from the instrument is shown in dashed blue in Figs. 4.4**a**&**b**. To retrieve the shape of the pulse, the difference between the signal and a Gaussian function of one of the following two forms was minimised using the residual sum of squares method:

$$F_1 = \exp\left(\frac{-4\ln(2)t^2}{\tau_1^2}\right) \tag{4.5}$$

$$F_2 = \exp\left(\frac{-4\ln(2)t^2}{\tau_{2,1}^2}\right) + r\exp\left(\frac{-4\ln(2)(t-s)^2}{\tau_{2,2}^2}\right), \tag{4.6}$$

where the subscript 1 denotes a single-Gaussian function and 2 a double-Gaussian function, and r and s are the relative amplitude and separation between the primary and secondary Gaussian signals in the double-Gaussian function, respectively. Either function appears to describe the signal reasonably well. Higher order summations of Gaussian functions over-fit the signal.

The spectrum of each pump is measured using an Ocean Optics Maya 2000Pro spectrometer. The spectra are shown in Figs. 4.4**c**&**d** averaged over several calibration shots. The weighted mean wavelength and full-width at half-maximum wavelength (assuming a Gaussian distribution, also shown in the plots) are found to be $\lambda = (788.1 \pm 23.2)\,\text{nm}$ and $\lambda = (793.2 \pm 26.0)\,\text{nm}$.

The beams are transported to the interaction area after compression and focused by off-axis parabolic mirrors (OAPs) with 3 m focal length (f-number 37.5) to $w \simeq 25\,\mu\text{m}$ spots. They interact at the target in nearly-counterpropagating geometry at an angle of 2.5°. They are linearly polarised with electric fields in the z-direction (see Fig. 4.6 for a description of the geometry). The beams are cleaned by soft apertures [266] before

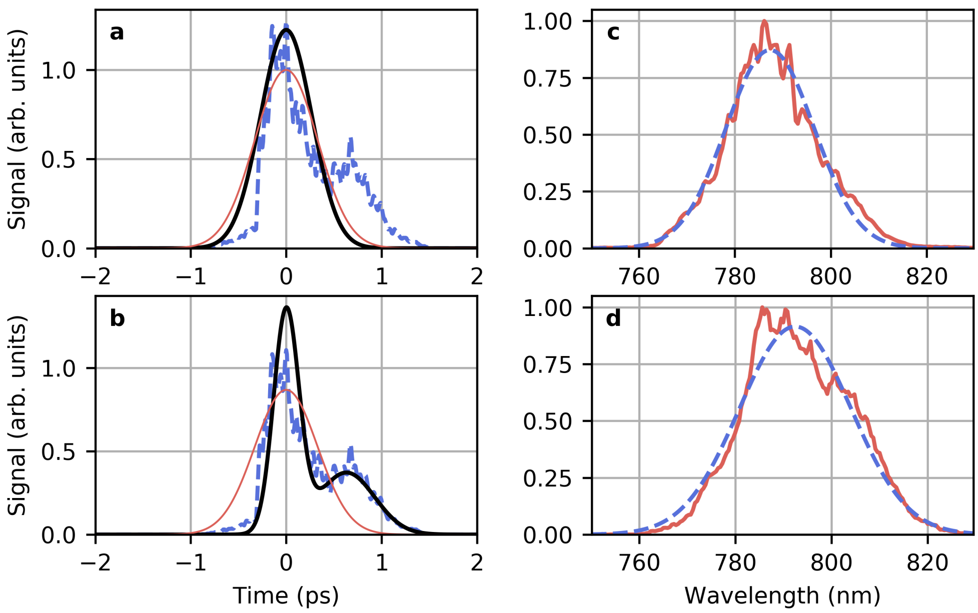

Figure 4.4: Temporal and spectral measurements of the Gemini pump beams. **a**, Sequoia data of one of the pump beams (dashed blue), the fitted cross correlation (thin red) and inferred Gaussian pulse (thick black). **b**, As **a** but with a double-Gaussian pulse. **c**&**d**, Average spectrum of each pump beam and fitted Gaussian function.

focusing, which halves their beam diameter to ~80 mm and improves the focal spot quality. A pair of deformable mirrors (one for each beam) is used along with wavefront sensors to further minimise aberrations in the focal plane. Each beam contains 50-200 mJ energy, which gives peak intensities in the range 1-5 $\times 10^{15}$ W cm^{-2}.

Probe beam

A third beam is derived from one of the pump beams by collecting the transmitted beam from a partially transmitting mirror before the compressor, which is used to probe the interaction. It is compressed in air in the target area to $\tau \simeq 100$ fs, as measured by a GRENOUILLE[1] device [267], and an aperture is used to reduce its diameter to 12 mm. A quarter-wave plate is placed in the beam to change its polarisation from linear to circular to allow for measurements of the birefringent plasma grating properties. A plano-convex lens with 500 mm focal length is used to focus the beam to a spot at the interaction point, an image of which is shown in Fig. 4.5. The image is formed by a 4X magnification achromat microscope objective on an Andor Neo vacuum cooled sCMOS camera. The spatial calibration of the focal spot camera is performed using the shadow of a 50 µm-diameter wire. Two methods for calculating the size of the focal spot are used – a 'sum-averaged' method (Fig. 4.5**a**) and a 'lineout' method (Fig. 4.5**b**&**c**). The first involves summing the pixel values in the horizontal and vertical directions separately to average over any aberrations and small-scale fluctuations. The second involves taking profile lines through the focal spot using 1$^{\mathrm{st}}$-order spline interpolation. A Gaussian function of the form

$$I = A \exp\left(\frac{-2\,(x - x_0)^2}{w^2}\right) \tag{4.7}$$

is fit to the data in each case, where I is the intensity profile varying in spatial coordinate x, and A, x_0 and w are the peak amplitude, centre coordinate and $1/\mathrm{e}^2$ waist radius of the fitted signal, respectively. The sum-averaged method gives a focal spot of size 47 µm × 43 µm, while the lineout method gives 45 µm × 30 µm.

[1] Grating-eliminated no-nonsense observation of ultrafast incident laser light E-fields

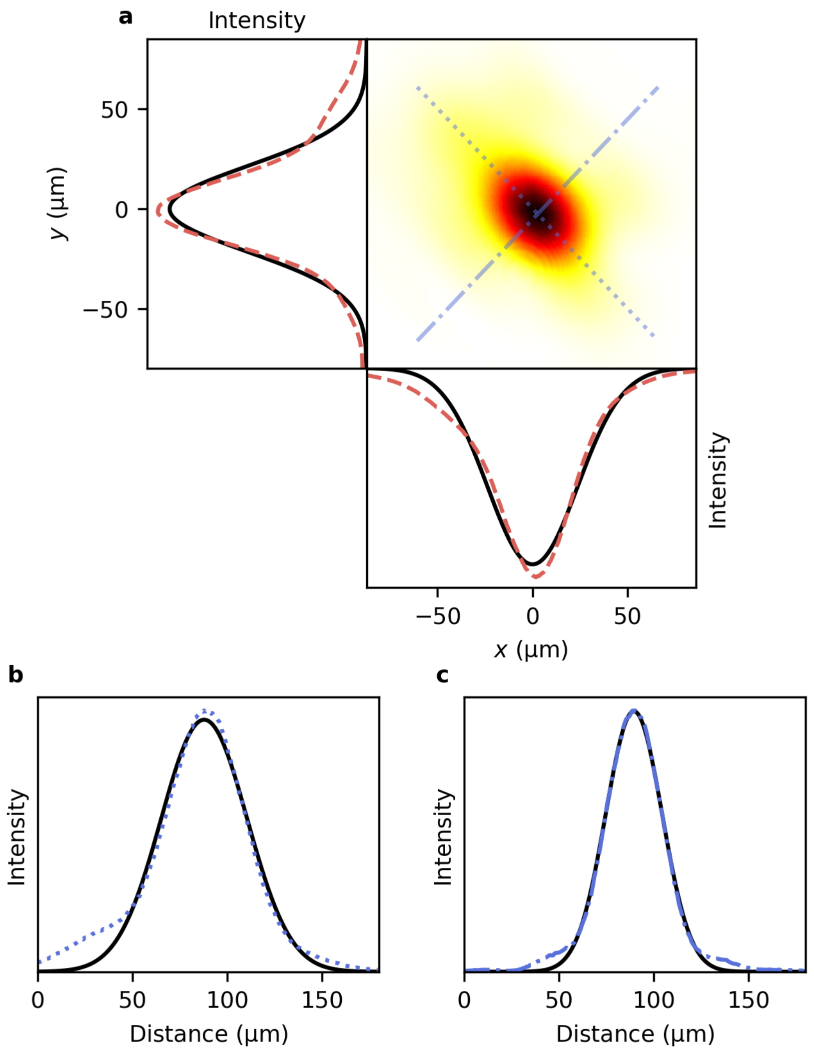

Figure 4.5: Focal spot of the Gemini probe beam. **a**, An image of the focal spot with sum-averaged profiles (dashed red) and Gaussian fits (solid black). **b**&**c**, Lineouts of the focal spot matching the lines in **a** (dotted and dot-dashed blue) and Gaussian fits (solid black).

The beam path is configured such that the probe pulse propagates perpendicular to the pump beams and has a common polarisation (see. Fig. 4.6). Following the interaction, the probe beam is collimated by a 250 mm-focal length, plano-convex lens and passes through a second quarter-wave plate at the same rotation to the first to change its polarisation to linear in the null case, i.e., when it is not altered by the interaction (see Fig. 4.7). This allows for easier determination of any polarisation changes due to the plasma, which presents as a second focal spot image appearing on the diagnostic camera (described in the following section).

4.1.3 Experiment layout and diagnostics

A schematic of the interaction geometry is shown in Fig. 4.6. After passing through the second quarter-wave plate, the probe is transported to a diagnostic area, as shown in Fig. 4.7. A 500 mm-focal length, plano-convex lens is used to focus the beam and its energy is optionally reduced by neutral-density (ND) filters. A turning periscope based on wedged windows simultaneously splits and attenuates the beam. The turning periscope configuration is chosen to attenuate orthogonal polarisation components to an equal degree. The beam transmitted through the first reflector of the turning periscope enters an integrating sphere, which acts as a depolariser [268], and is coupled to a spectrometer[2] via a multi-mode optical fibre. The beam reflected from the turning periscope passes through a quartz Wollaston prism with a 1° separation angle. The Wollaston prism, focal spot imaging system and camera are referred to as the probe 'polarisation diagnostic'.

The focal spots of the beams following separation by the Wollaston prism are imaged onto the same 16-bit Andor Neo sCMOS camera chip by a 4× microscope objective. Fig. 4.8 shows an example of data recorded by the probe polarisation diagnostic when neither of the pump beams are fired. The camera chip is significantly larger than the focal spot images so the regions around each spot are concatenated, with the join indicated by the vertical dashed line. Greater than 95% of the energy is contained in the left panel component, indicating linear horizontal polarisation, i.e., the beam is

[2] Ocean Optics Maya2000 Pro.

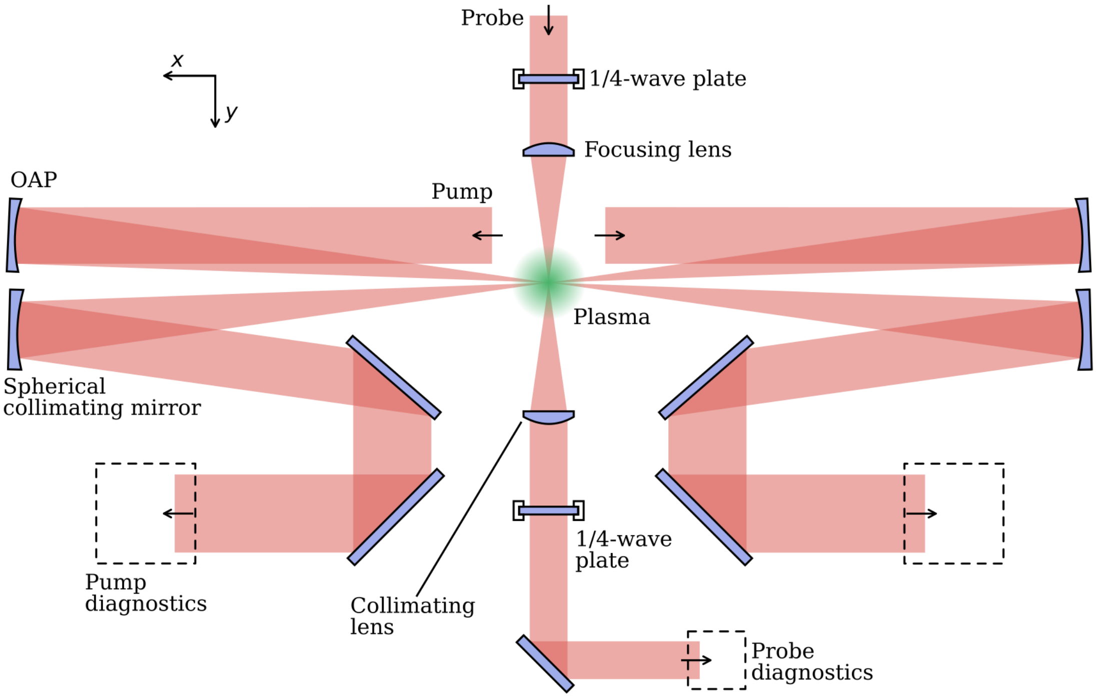

Figure 4.6: Pump-probe schematic layout of the Gemini experiment. The beam paths have been significantly simplified for clarity.

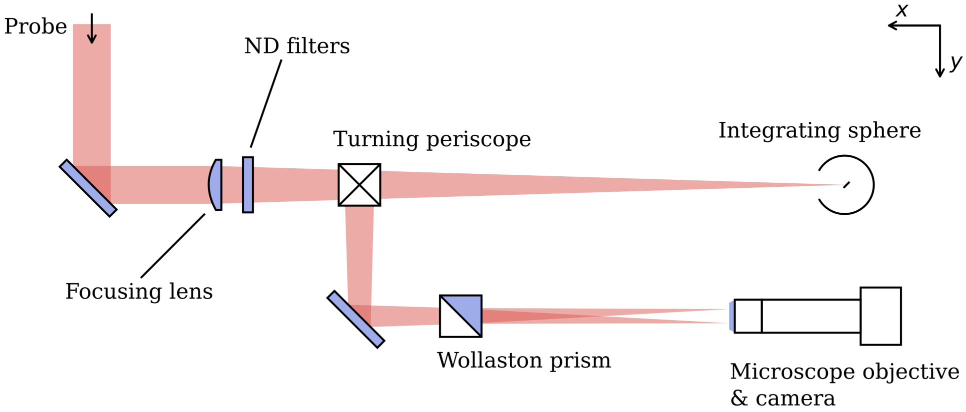

Figure 4.7: Probe beam diagnostics schematic layout for the Gemini experiment.

initially vertically polarised, transformed to circular by the first quarter-wave plate and then to horizontal by the second quarter-wave plate.

Figure 4.8: An example baseline measurement of the probe polarisation diagnostic. Each panel shows the region around the orthogonally-polarised focal spot images produced on the sCMOS camera by the Wollaston prism and imaging lens.

To measure the polarisation, the ratio of energy contained in the orthogonal field components must be calculated, which can be done by summing up individual pixel values. The pixel values in a region comprising $\sim$5% of the area of the chip in one of the corners of the image (well away from any signal due to the probe) are averaged to give a background noise value, which is subtracted from all pixels in the image. Any negative values are set to zero. The image is then split horizontally into two portions with equal dimensions. Each far field image is well separated from the divide. The centre-of-mass coordinate in each panel is found and a square region with dimension 400 pixels is selected around it. The pixel values are then summed in each of these regions and the value

$$\mathcal{R} = \frac{\sum p_1}{\sum p_1 + \sum p_0} \tag{4.8}$$

is calculated (cf. Eqn. (3.56)), where p_1 and p_0 are the pixel values in each region of interest. For the shot shown in Fig. 4.8, $\mathcal{R} = 0.05$, which indicates a very slight baseline ellipticity in the polarisation of the probe. An image of the focal spot in the right-hand side of the figure is only observable on very close inspection.

4.2 Probe delay scan

The probe beamline and one of the pump beamlines include delay stages. The valve opening time is adjusted until a clear plasma channel is formed by one of the pump beams with fixed delay. The timing of the probe is then adjusted by first ensuring it arrives before the pump beam, then gradually adding to its arrival time by adjusting the delay stage until distortions are observed in its far-field profile, caused by interaction with the plasma. The probe delay value is then fixed and the timing of the second pump beam adjusted by the same method. The relative delay between the two pump beams is then fixed and the probe arrival time varied to scan the evolution of the interaction.

The following sections present data recorded by the probe polarisation diagnostic and probe integrating spectrometer, which are discussed in Sec. 4.2.4.

4.2.1 Probe polarisation and far field profile measurements

After some adjustment of the probe arrival time, the probe polarisation is observed to be altered. Example data from the probe polarisation diagnostic in this case is shown in Fig. 4.9. For this shot, the gas jet backing pressure is set to 60 bar, giving $n_0 \simeq 5 \times 10^{19}\,\mathrm{cm}^{-3}$.

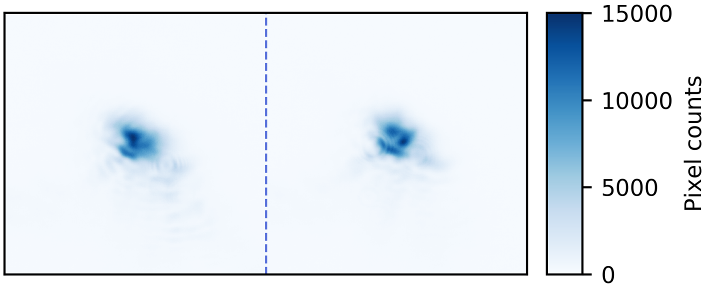

Figure 4.9: An example of probe polarisation diagnostic data after optimisation of the delay between the pump pulses and the probe.

Once a suitable timing is identified to give a phase shift in the probe, the arrival time of the probe is incrementally scanned on either side of the optimum until the ratio in energy between the components measured by the polarisation diagnostic returns to close to the unperturbed levels. This is performed while maintaining a constant backing pressure of the gas jet to give $n_0 \simeq 5 \times 10^{19}\,\mathrm{cm}^{-3}$. The spacing between each delay stage position gives time coordinates for the probe arrival separated by 330 fs. Between 3 and 14 shots are taken at each setting.[3] Results of the delay scan are shown in Fig. 4.10 as red circles. Associated error bars are the 90% confidence interval of the mean derived from the Student's t-distribution. The green triangle data point in Fig. 4.10 shows the measurement of $\mathcal{R}$ when no gas jet was present and therefore represents the unperturbed ratio. Three shots were taken where only a single pump beam fired (blue square in Fig. 4.10), which resulted in a probe polarisation form that is almost completely unperturbed.

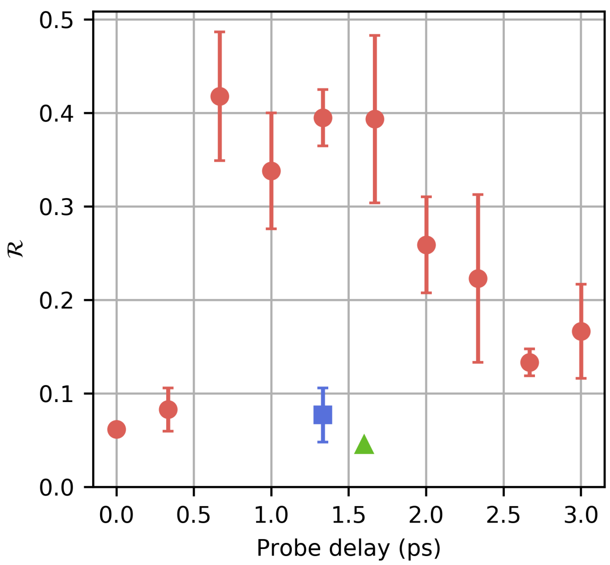

Figure 4.10: Probe polarisation energy ratio measurement with delay (red circles). The green triangle indicates a measurement where the gas jet was not present and the blue square shows shots where only a single pump beam was fired. Time values are relative to the earliest arrival time of the probe in this scan.

Two shots in the delay scan data set of Fig. 4.10 comprise saturated images from the probe polarisation diagnostic. The saturated pixel values are reconstructed by fitting Gaussian functions to each row and column of pixels (independently) that contain at

[3] A higher number of shots were taken when the probe diagnostic measurements exhibited greater variability. For instance, the probe polarisation form was relatively stable at either extrema of the delay stage setting relative to the position that gave a maximal phase shift, so fewer sample shots were taken.

least one saturated pixel. The row- or column-fit pixel values are chosen to replace the saturated pixels depending on which method gave a lower sum of square differences between each unsaturated pixel measurement and prediction.

4.2.2 Probe energy measurements

The total energy in the fields measured by the polarisation diagnostic is calculated by the same method as that detailed in Sec. 4.2.1, except the total field pixels are summed instead of calculating $\mathcal{R}$. The energy in the components on the polarisation diagnostic at each discrete delay stage setting is shown in Fig. 4.11. The two components are separated and presented as stacked bars. The error bars again show the 90% confidence interval of the mean calculated from the Student's t-distribution.

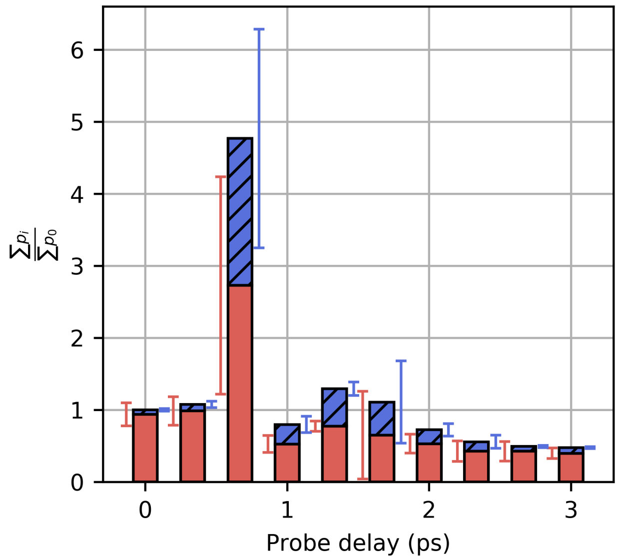

Figure 4.11: Mean probe energy with delay normalised to the initial energy. Solid red bars and left error bars relate to region of interest 0 (see Eqn. (4.8)) and hatched blue bars and right error bars to region of interest 1. Regions of interest are the left- and right-hand side of the composite images, examples of which are shown in Figs. 4.8 and 4.9. Error bars indicate the 90% confidence interval of the mean calculated from the Student's t-distribution.

4.2.3 Probe spectral measurements

The probe spectrum has been measured using the integrating spectrometer. The unperturbed spectrum is measured when no gas is expressed by the nozzle. The upper-left panel of Fig. 4.12 shows the average unperturbed spectrum from eight consecutive shots, where each spectrum is first normalised to its maximum before the mean signal in each bin is calculated. The weighted mean wavelength and standard deviation of the average of the normalised signals is $\lambda_1 = 803\,\mathrm{nm} \pm 9\,\mathrm{nm}$, which, for a Gaussian distribution, gives a full-width at half-maximum value of 15 nm.

The upper-right and lower two rows of Fig. 4.12 show sample integrated probe spectra at various values of delay, which are indicated above each panel. The average unperturbed spectrum has been normalised and reproduced in each panel for comparison. The vertical axis on each plot is independently scaled as the amplitude of the signal varied shot-to-shot by up to two orders of magnitude. The spectrometer is saturated for the shot with data presented at 0.67 ps, which corresponds to one of the probe far field polarisation diagnostic shots that also exhibited saturation, as described in Sec. 4.2.1. The spectral data for the delay scan presented in Fig. 4.12 are individual samples, but are indicative of all other data from the same diagnostic, which all exhibit similar features (namely, a 'spiky' spectrum due to interference, and asymmetrical broadening and blueshifting).

4.2.4 Discussion and plasma-induced wave retardance calculation

The single-pump data points (blue square) of Fig. 4.10 shows that, at that particular probe delay value ($t_{1,d} \sim 1.3\,\mathrm{ps}$), the modification of the probe polarisation only occurs when both pump beams fire, otherwise the probe polarisation is roughly equal to its unperturbed state (green triangle data point). This indicates the formation of an inertial plasma grating that is initiated earlier in time by the colliding pump beams arriving before the probe, which leads to modification of the probe polarisation state to give $\mathcal{R} = 0.4$. The subsequent decay of the $\mathcal{R}$ measurement with increasing probe delay is therefore likely to be due to the probe polarisation rotation diminishing due to the decay of the structure. Conversely, the preceding data points do not necessarily

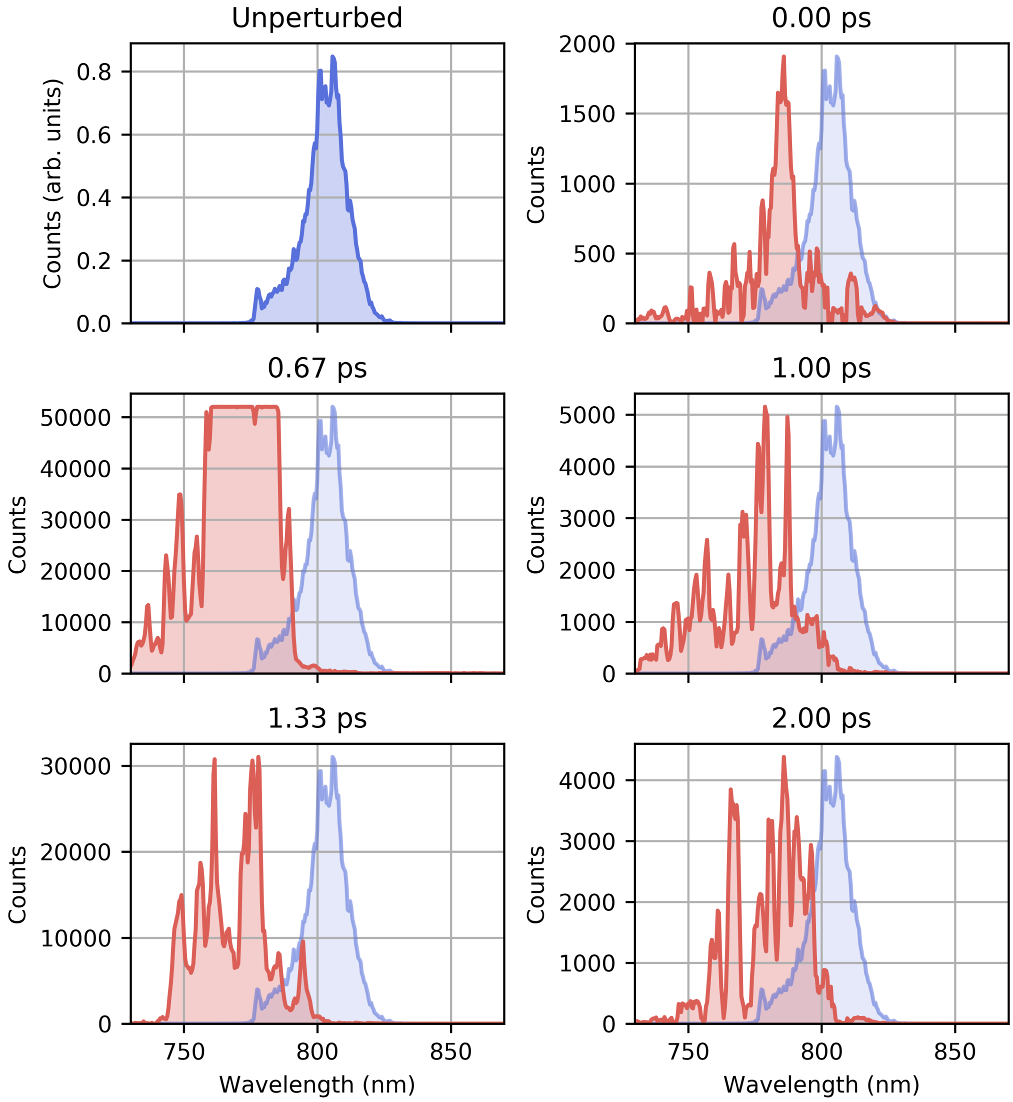

Figure 4.12: Sample probe integrating spectrometer measurements for various delay values. The upper-left panel shows the average unperturbed probe spectrum in arbitrary units, which is scaled and reproduced for comparison in the other panels. The shot at 0.67 ps exhibits signal saturation.

indicate the evolving formation of the plasma structure because the probe polarisation diagnostic cannot directly distinguish between polarisation alteration due to interaction with an inertial grating and amplification and/or delayed scattering due to an ionisation grating. The overall lifetime of the structure (on the order of a picosecond) is consistent with a scaling law derived from the nonlinear plasma fluid equations: [269]

$$t \sim \frac{(m_i/2Zm_e)^{1/2}}{ka_0c}, \tag{4.9}$$

where m_i/m_e is the ion-electron mass ratio and the electrons oscillate in a laser field with wavevector k and dimensionless strength a_0.

However, evidence of interaction with an ionisation grating can be seen in the polarisation diagnostic, when the data is used to determine the energy in the probe-directional fields, as shown in Fig. 4.11. There is significantly more energy collected by the diagnostic when the probe delay is set to $t_{1,d} \sim 0.6\,\mathrm{ps}$. This is due to amplification and scattering that results from interaction of the probe and pump beams, which creates a 45° ionisation grating (cf. Fig. 3.23). Saturation of the probe spectrum diagnostic is further evidence of scattering from the ionisation grating resulting in increased energy in the fields component common to the pumps. The reduction in the total energy for longer probe delays is also reproduced in simulations.

For probe delay values less than 0.6 ps, the probe arrives sufficiently early so as not to interact with the pumps and generate a 45° ionisation grating. It also arrives significantly before an inertial grating forms, and therefore no change in the polarisation or energy in the probe occurs.

The probe spectrum is significantly modified by the interaction. For low values of delay (typically $< 0.6\,\mathrm{ps}$, e.g. the upper-right panel of Fig. 4.12), the probe spectrum is blueshifted but the spectral shape remains qualitatively similar. For the remaining delay values (e.g. middle and lower rows of panels of Fig. 4.12), the probe spectrum exhibits oscillatory modulations, blueshifting and spectral broadening. These features may be due to the probe witnessing a rapidly changing refractive index of the medium in which it propagates as the gas is ionised by the pump pulses [270].

For a delay setting that results in a change in the probe's polarisation and little or no change in the measured energy, Jones calculus may be used to infer the phase shift between the two orthogonal field components due to an inertial grating, in a similar way to that discussed in Sec. 3.3.4. The unperturbed polarisation of the probe is determined first by measuring the fraction of energy in each polarisation component for a baseline shot, as shown in Fig. 4.8, which shows that around 95% of the energy is in one of the components and 5% in the other, making the probe initially nearly horizontally polarised when it encounters the polarisation diagnostic. The initial polarisation of the probe is

$$I = \begin{pmatrix} 0.05^{1/2} \\ (1-0.05)^{1/2} \end{pmatrix}. \tag{4.10}$$

The probe then passes through a quarter-wave plate with Jones matrix

$$Q = \mathrm{e}^{-\frac{\mathrm{i}}{4}} \begin{pmatrix} \cos^2\theta + \mathrm{i}\sin^2\theta & (1-\mathrm{i})\sin\theta\cos\theta \\ (1-\mathrm{i})\sin\theta\cos\theta & \sin^2\theta + \mathrm{i}\cos^2\theta \end{pmatrix}, \tag{4.11}$$

where $\theta = 45^\circ$ is the fast axis azimuth of the optical device. The probe then encounters the plasma, which imparts a phase shift Γ and has the associated Jones matrix[4]

$$R = \begin{bmatrix} \exp\left(\frac{\mathrm{i}\Gamma}{2}\right) & 0 \\ 0 & \exp\left(\frac{-\mathrm{i}\Gamma}{2}\right) \end{bmatrix}. \tag{4.12}$$

The probe then passes through another quarter-wave plate with a Jones matrix equal to the first, before being transported to the diagnostics. The final polarisation of the probe is then given by

$$\begin{aligned} F &= QRQI \\ &= TI, \end{aligned} \tag{4.13}$$

[4]Cf. Eqn. (3.53) where the spectrally dependent phase shift, Γ_λ, is accounted for. In the experiment there was no way of determining the phase shift of the spectral components.

where $T = QRQ$ is the transfer matrix of the beamline and

$$R = \frac{F_1}{F_0 + F_1}. \tag{4.14}$$

The relationship between Γ and $\mathcal{R}$ may be determined by solving Eqn. (4.13) for values of $\Gamma \in [0, 2\pi]$. This is shown in Fig. 4.13, where the dashed blue line shows the solutions to Eqn. (4.13) in terms of $\mathcal{R}$ for a beam with initially vertical polarisation, i.e., if one spot in the unperturbed probe polarisation measurement contained all of the energy. The solid red line shows the response to varying Γ when I is given by Eqn. (4.10).

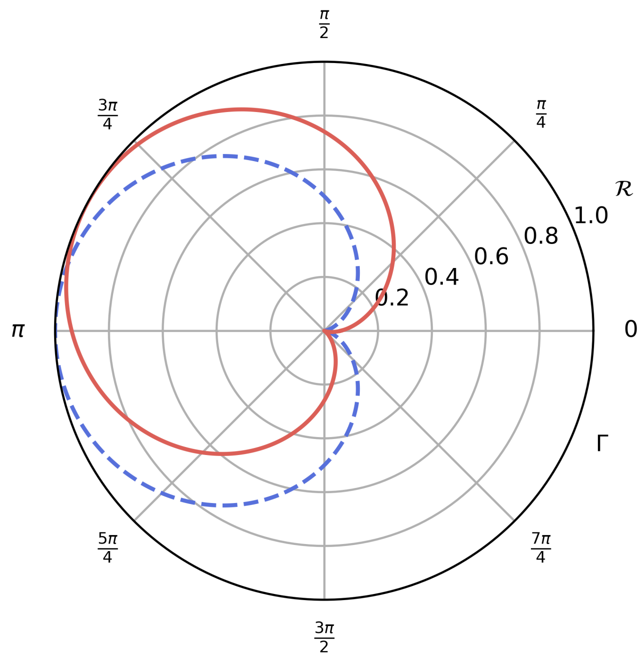

Figure 4.13: Proportion of energy in one of the spots measured by the probe polarisation diagnostic as a function of plasma retardance. The dashed blue line shows the relationship for an initially perfectly vertically polarised beam, while the solid red line accounts for the slight initial ellipticity measured during calibration of the diagnostic.

For a given value of $\mathcal{R}$ measured using the polarisation diagnostic, the retardance in the probe induced by the plasma, Γ, may be predicted by solving Eqn. (4.13), which has been performed by numerical interpolation. The largest measured ratio is $\mathcal{R} = 0.4$, which occurs at a delay of 1.3 ps and corresponds to a phase shift of around $\pi/4$. This value has a large uncertainty, which is difficult to quantify. The main contributor to the uncertainty arises from the method of measuring the energy in each polarisation component. As the probe spatial extent is larger than that of the pump beams, the wings of the probe focal spot in the interaction region do not interact with the ponderomotively produced grating. Furthermore, the largest phase shift occurs in the region of the probe that passes through the centre of the grating (i.e., through the optical axis of the pump beams) as the grating is most strongly driven there.[5] The phase shift is therefore a function of radial distance from the spatial centre of the probe (assuming good alignment), which is not accounted for when summing the pixels to determine the energy in each component when analysing the probe polarisation diagnostic data using the method described in Sec. 4.2.1 above. Due to the relatively low pump beam intensity requirement for formation of an inertial plasma grating, future experiments may benefit from using pump beams with significantly larger focal spot waists than the probe beam, so that any radial variation in the grating encountered by the probe can be neglected when measuring the phase shift induced by the structure.

4.3 Conclusions

The results described above present the first demonstration of the control of the polarisation of a probe laser pulse using a volume plasma density grating that is formed by intersecting pump laser pulses in underdense plasma. The findings also include evidence of scattering due to an ionisation grating, which, in this configuration, enhances the energy in the probe-directed electric fields. It is unclear whether this is due to amplitude amplification of the original probe fields by interaction with an evolving ionisation grating, scattering of the pump pulses from a residual static ionisation grating, or a combination of both processes. However, these results are also the first measurements of the processes described in Sec. 3.2.

While this proof-of-concept experiment constitutes a necessary step for the realisation of volume plasma density grating-based optical devices, the development of a future device must overcome significant hurdles. Principally, the deleterious effects on the probe fields due to interaction with an ionisation grating must be addressed. The

[5]Refer to Sec. 3.1.1 for a discussion of non-slab ponderomotive gratings.

strategies proposed in Sec. 3.4 (using a preformed plasma, choosing a geometry that allows for orthogonally polarised pump and probe beams, and spectral detuning and filtering) are also valid here, and further experiments should be performed to investigate their effectiveness. Secondly, the configuration of the experiment described above is highly complex, because of the general purpose nature of the facility at which it was conducted. Clearly, a device requiring national-scale facility equipment is impractical, expensive and difficult to scale. However, a bespoke design would allow for a significantly reduced footprint and complexity of the device, which would decrease the risk of failure, increase its robustness, and make it simpler to use.

Having demonstrated relative phase control using a volume plasma density grating, further proof-of-principle studies may investigate one or more of the other proposed schemes of probe pulse manipulation, which are namely reflection [32], polarisation-dependent absorption [31], and holographic focusing and mode conversion [271]. The different regimes of plasma grating growth and persistence could also be investigated [269, 272].

Chapter 5

Plasma density gratings as electron injectors for the laser wakefield accelerator

This chapter presents the first preliminary numerical study of the use of inertial plasma gratings in laser wakefield accelerators (LWFAs). Plasma gratings are potentially suitable for controlling the properties of a plasma wake and may therefore be useful for influencing the process of injection of electrons from the background plasma into the LWFA structure. The properties of the resulting accelerated electron beam may be modified by manipulating the plasma grating parameters, resulting in a laser wakefield accelerator with a tuneable, all-optical injection mechanism.

The plasma gratings discussed herein are formed by colliding two counterpropagating pump laser pulses in a preformed, underdense plasma. The plasma grating pump pulses propagate collinear with the laser wakefield driver. A homogeneous plasma slab with sinusoidal coupling ramps is used and the plasma grating (also referred to as the 'injection structure' in this context) and accelerating region were formed in the initially-homogeneous plasma volume. This configuration is chosen for simplicity, although it is unlikely that the optimal plasma conditions for injecting electron bunches and accelerating them are identical. Only the geometric configuration in which pump beams of the plasma grating and the laser wakefield driver are collinear has been considered in the present work.

The methods for forming the plasma grating and laser wakefield accelerator target are presented in Sec. 5.1. The electron bunch injection dynamics and resulting beam properties are discussed in Sec. 5.2, and a parametric scan of plasma grating amplitude and position is presented in Sec. 5.3.

5.1 Forming the plasma grating and LWFA target

Two counterpropagating pump beams are set to collide in underdense plasma to produce an inertial plasma grating. The pump beams have Gaussian temporal profiles and are assumed to be spatially infinite. They have a peak intensity of $I_0 = 9 \times 10^{14}\,\mathrm{W\,cm^{-2}}$, a full-width at half-maximum intensity duration of $\tau_0 = 330\,\mathrm{fs}$, and are unchirped with wavelength $\lambda_0 = 800\,\mathrm{nm}$. The background plasma density is $1.75 \times 10^{18}\,\mathrm{cm^{-3}}$, which is chosen as it is typical in laser wakefield acceleration experiments [4].

Simulation of the formation of the plasma grating is carried out using the 1-dimensional version of EPOCH. The simulation employs 128 macroparticles-per-cell and 40 cells-per-laser-wavelength. A 400 µm-long plasma slab is initialised in the centre of the simulation window. The pump pulses collide in the centre of the plasma slab and the simulation is set to evolve until the structure reaches its maximum amplitude. The simulation file is given in Appx. C.5.

With the above laser and plasma parameters, the plasma structure is nearly 100% modulated, without depletion of electrons in the grating troughs.

The saturated structure is then inserted into a plasma target for use in laser wakefield injection studies. The target, whose profile is shown in Fig. 5.1, consists of 100 µm-long sinusoidal coupling ramps (Fig. 5.1**d**) and the injection structure (Fig. 5.1**c**) located at $x_i = 300\,\mu\mathrm{m}$ in a plasma plateau with unperturbed density $n_0 = 1.75 \times 10^{18}\,\mathrm{cm^{-3}}$, where x_i corresponds to the centre of the grating. The geometry is chosen such that the plasma grating pump pulses are colinear with the laser wakefield drive pulse.

Noise, due to numerical sampling of the continuous electron phase space distribution [226, 273], appears in the 1-dimensional simulation used for the injection structure

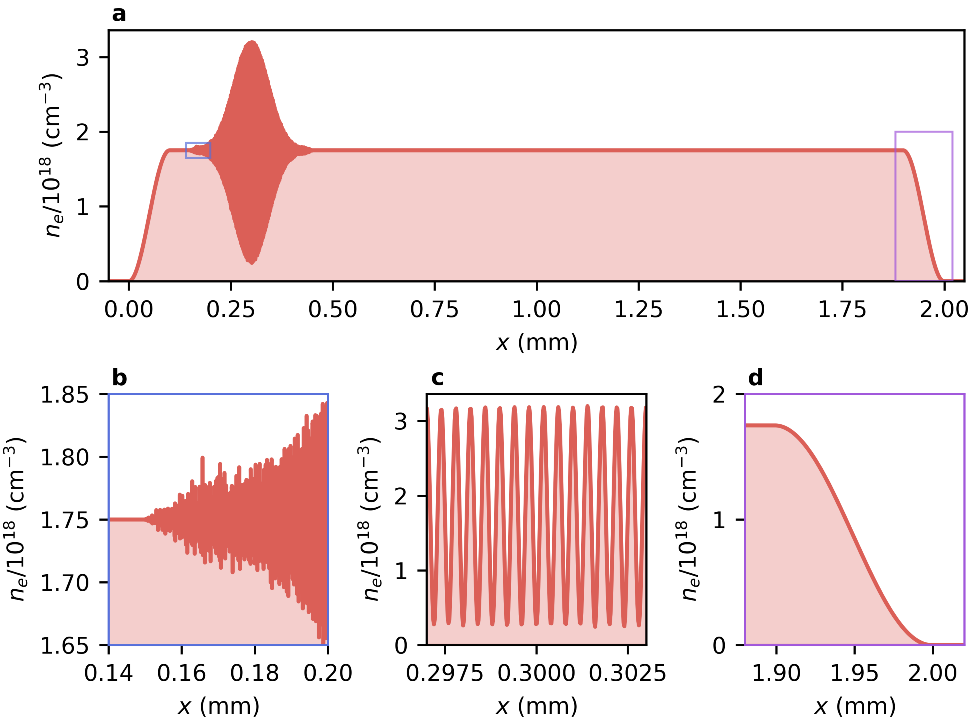

Figure 5.1: Number density profile used for laser wakefield acceleration in the parallel geometry. **a**, The complete number density profile, with region of interest boxes indicating the zoomed axes for the interface between the template and plateau (**b**), fine modulations of the injection structure (**c**, region centred on $x = 0.3\,\text{mm}$), and sinusoidal exit ramp (**d**).

template. To mitigate spurious interaction of the drive beam with the noise boundary at the interface of the injection structure template and plateau, the number density is linearly blended between the plateau and template simulation data over a distance $n_b = 15\,\mu\text{m}$. Fig. 5.1**b** shows the number density in this blending region.

5.2 Electron beam injection and acceleration

Particle-in-cell simulations are performed with FBPIC to investigate the effect of a plasma grating on the injection of electron bunches into laser wakefield accelerators and the properties of the subsequent electron beams.

5.2.1 Simulation parameters

In this first set of simulations, a laser with $a_1 = 3.5$ (the subscript 1 refers to the drive beam) and Gaussian spatiotemporal shape with matched spot size (see Sec. 2.3.4, in particular Eqn. 2.70 and Fig. 2.8) $w_1 = 15.3\,\mu\text{m}$ and full-width at half-maximum intensity duration $\tau_1 = 17.7\,\text{fs}$ travelling in the $+x$-direction is focused into the target shown in Fig. 5.1 at the top of the transition ramp. The simulations have a cell size of 40 nm in the direction parallel to the drive beam propagation (x) and $70\,\mu\text{m}$ radially. They employed 3 azimuthal modes and had 3, 2 and 8 macroparticles per cell along the longitudinal, radial and azimuthal directions, respectively. Another simulation identical to this, except for the plasma target, consisting of a continuous plateau instead of a plateau with injection structure is also performed for comparison. The simulation file for the case with a plasma grating is given in Appx. C.6.

5.2.2 Control of the laser wakefield bubble

The effect of the plasma grating on the velocity of the back of the bubble is determined, which is key to controlling injection of electrons into the accelerating bubble structure [189]. The position of the back of the bubble, x_b, is defined as the point behind the drive beam at which the longitudinal electric field gradient is negative and its value is zero (see Fig. 2.7**a**). This position is determined at each output dump, which occurs with a periodicity of $t_d = 33.4\,\text{fs}$. The velocity of the back of the bubble is then

$$v_b = \frac{\Delta(x_b)}{t_d}, \tag{5.1}$$

where Δ is the first-order discrete difference function. The evolution of the velocity of the back of the bubble is shown in Fig. 5.2, both with and without the plasma grating present. The raw data is shown by the dashed lines, which exhibits noise due to the discrete nature of the grid. A 1-dimensional uniform filter[1] is applied to reduce this noise, and the resulting data represented by the solid lines. The vertical dotted line indicates the time at which the point one plasma wavelength behind the temporal centre of the drive beam interacts with the centre of the plasma grating, calculated assuming the laser pulse is non-evolving and travels constantly at c. The surrounding grey shaded area indicates the temporal intensity FWHM duration of the plasma grating pump pulses. The actual time that the back of the bubble interacts with the plasma grating is delayed for two reasons: the back of the bubble is further than one plasma wavelength behind the peak of the electric field envelope of the laser due to the relativistic mass increase of the plasma electrons; and the group velocity of the laser pulse in the plasma is less than c (see Eqn. (2.50)). However, this difference is expected to be slight.

The bubble velocity is modified by the presence of the plasma grating – it is enhanced, relative to the null case, when the gradient of the plasma grating amplitude envelope is positive and reduced when the gradient is negative. Once the wakefield bubble has passed the plasma grating, its velocity returns to closely match the unperturbed bubble velocity. There is no difference in the group velocity of the drive laser between the two simulations over the course of either, suggesting that the change in the bubble velocity is due to the interaction with the plasma structure and not as a secondary consequence of manipulation of the drive beam velocity.

[1]The `uniform_filter1d` function [274] of SciPy's ndimage module was used.

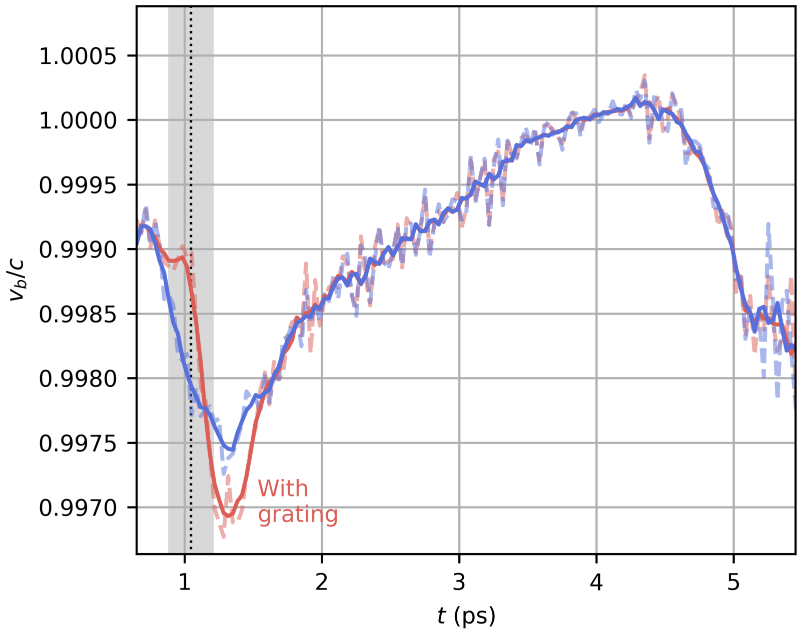

Figure 5.2: Evolution of the velocity of the back of the bubble with (red, labelled) and without (blue, unlabelled) a plasma grating present. Dashed lines show the raw data and solid lines after application of a uniform filter. The vertical dotted line shows the location of the plasma grating and the surrounding shaded region shows the temporal intensity full-width at half-maximum of the plasma grating pump pulses.

5.2.3 Electron energy spectrum measurements

The controlled modification of the velocity of the back of the bubble leads to a change in the dynamics of electron injection into the accelerating structure. This can be seen prominently in the energy spectrum of the accelerated electrons, the evolution of which is shown in Fig. 5.3 for both simulations. The null case exhibits spontaneous self-injection of 1.07 pC of electronic charge with 3.30% RMS spread, while the simulation with a plasma grating injected 1.64 pC with 2.80% RMS spread. These charge measurements are given for electrons that are accelerated to $\gamma > 850$ at 5.5 ps (see Fig. 5.4**c**).

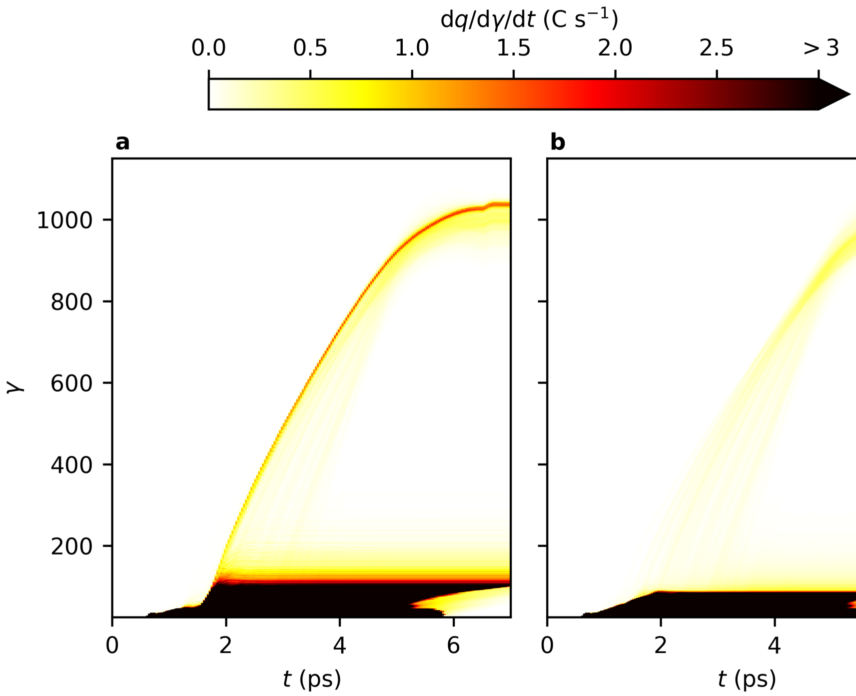

Figure 5.3: Evolution of the electron energy spectrum with (**a**) and without (**b**) a plasma grating present.

Fig. 5.4 shows the electron energy spectrum at $t = 5.5$ ps for each simulation, near the end of the acceleration stage. Panel **b** shows the spectrum in the region $56 \leq \gamma \leq 210$ and panel **c** shows the region $851 \leq \gamma \leq 1070$. The lower-energy regions contain 12.5 pC and 4.4 pC of electronic charge with and without the plasma grating, respectively. By tracking the positions of individual macroparticles through the simulation, the particles forming the lower-energy pedestal of the electron energy spectrum (which are particularly evident in Fig. 5.3) are found to form the wide-angle electron beam present in laser wakefield accelerators [156, 275, 276]. The charge values cited above therefore only encapsulate macroparticles that have not yet left the simulation window at the time of measurement and are thus not indicative of the total amount of wide-angle charge produced. While this measurement is beyond the scope of the present work, it is interesting to note that the plasma grating-assisted scheme appears to produce a wide-angle electron beam with significantly more charge, despite the total number of plasma particles in both cases being identical.

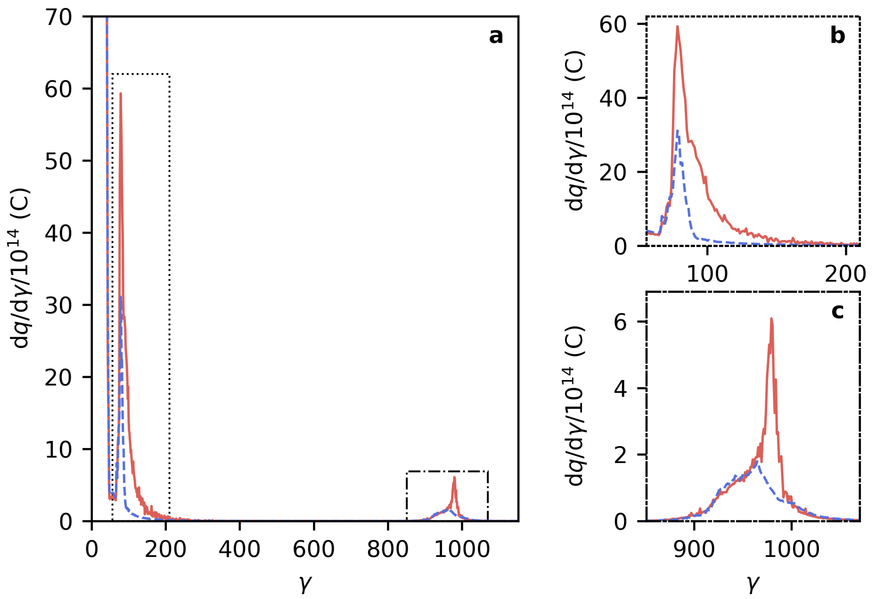

Figure 5.4: **a**, Comparison of the energy spectra of the accelerated electrons with (solid red) and without (dashed blue) the plasma grating. Two regions of interest with low (dotted box, **b**) and high (dot-dashed box, **c**) electron energy are also shown.

The same particle trajectory tracking technique is applied to the high-energy electron subspecies, which are found to be injected into the bubble close to the laser propagation axis and stay within ~1.5 µm of the radial centre of the bubble during the accelerating stage (see Figs. 5.5 & 5.6).

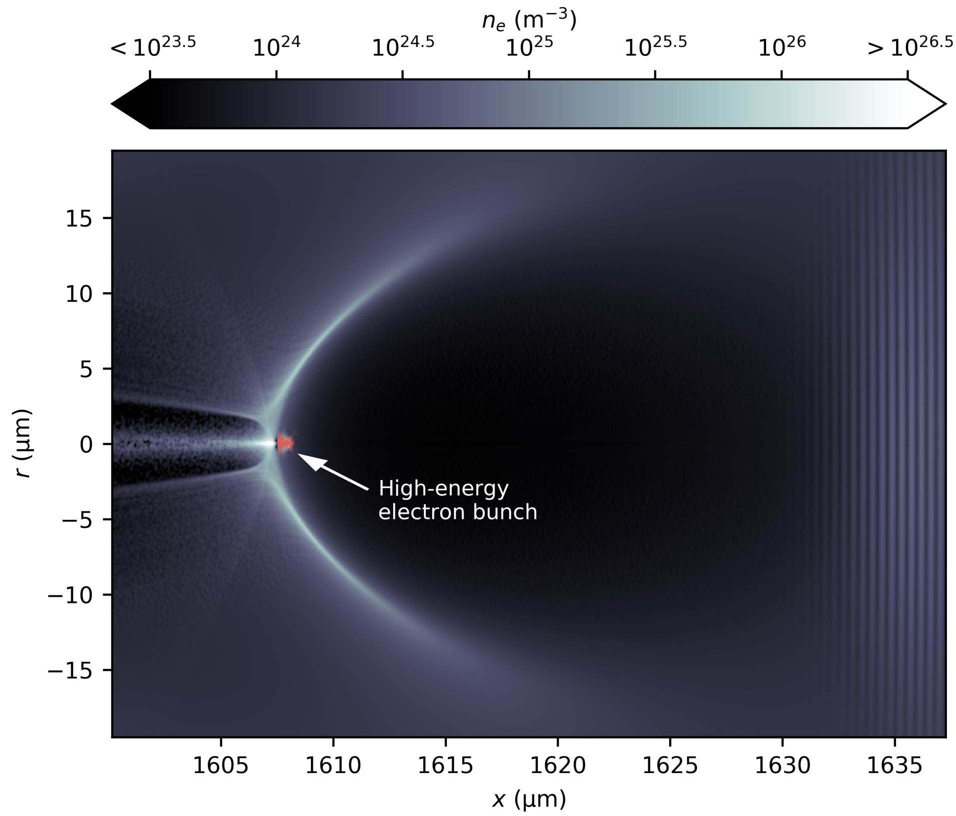

Figure 5.5: Electron number density of the plasma grating-assisted laser wakefield accelerator towards the end of the acceleration stage. A random subsample of 10,000 electron macroparticles in the high-energy bunch are shown in red.

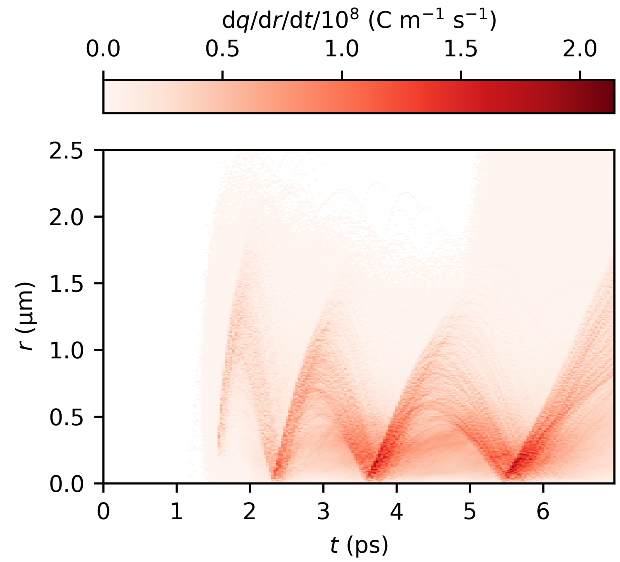

Figure 5.6: Evolution of the radial position of the electrons injected into the accelerating structure. The macroparticles forming these data are selected from those reaching $\gamma > 851$ at 5.5 ps.

5.2.4 Electron charge distribution and current measurements

Fig. 5.7 shows the injected electron bunch, situated near the back of the bubble, and its longitudinal charge distribution with and without the plasma grating in the left and right column of panels, respectively. Panels **a** and **b** show the electron number density spatial distribution on a logarithmic colour axis, and panels **c** and **d** show the charge per unit length in the same spatial region, for electrons with $\gamma > 850$, i.e., those comprising the high-energy bunch. The inset to panel **c** shows the current in a longitudinal region of interest. The shape of the injected bunch is almost identical in both simulations, with the exception of a sharp peak of high current towards the head of the bunch in the plasma grating case, which reaches a maximum of 4.5 kA. This suggests that a localised event unique to the plasma grating case causes the injection of this short bunch superimposed on the 'background' electrons, which are spontaneously self-injected and are relatively unmodified by the presence of the grating. The plasma grating-assisted and null bunches have similar RMS durations of 533 as and 631 as, respectively. However, the full-width at half-maximum duration of the plasma grating-assisted bunch is 133 as, which is more than an order of magnitude shorter than the null case at 1.43 fs.

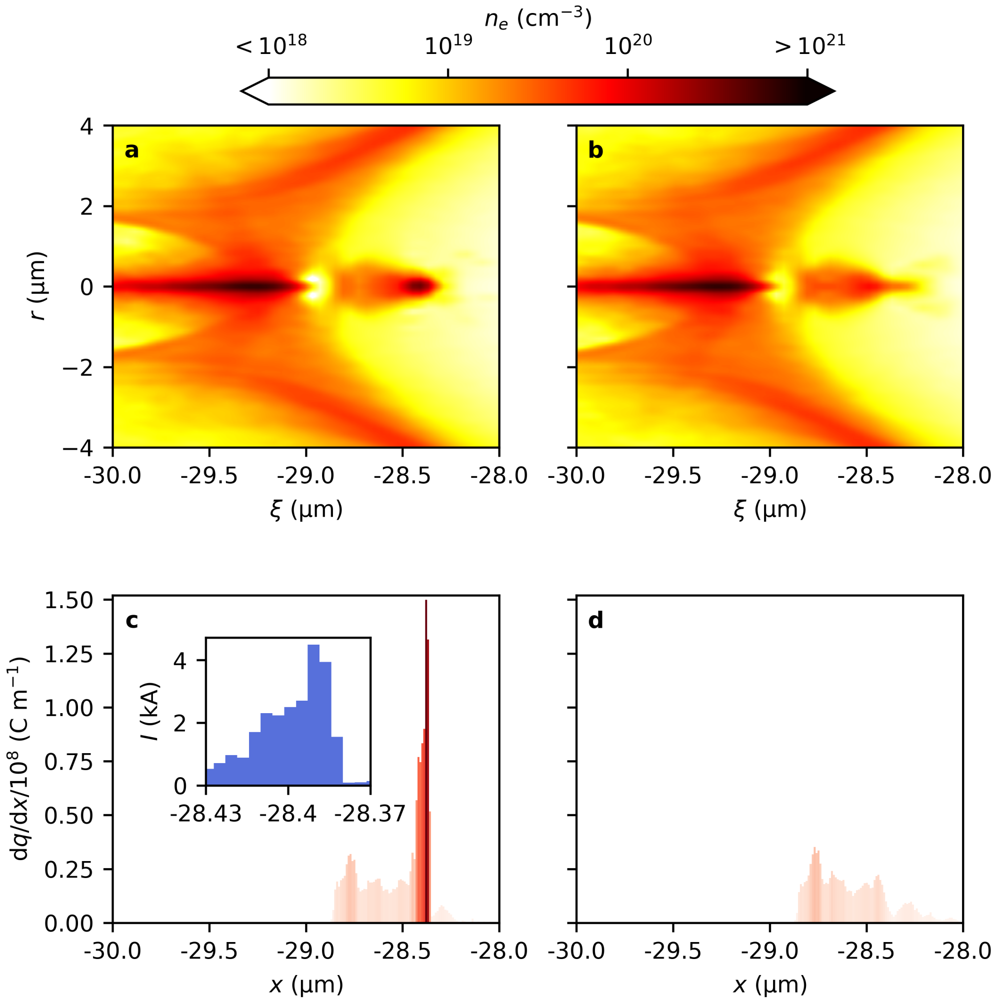

Figure 5.7: **a**&**b**, Log-scaled electron number density around the back of the bubble with (**a**) and without (**b**) the plasma grating. **c**&**d**, Longitudinal charge distribution of the high-energy injected electron bunch with (**c**) and without (**d**) the plasma grating. The inset to panel **c** shows the instantaneous electronic current in a region of interest in the bunch.

The x- and y-directional projected emittances [277] of the plasma grating-assisted beam at 5.5 ps are $\varepsilon_x = 506\,\pi\,\mathrm{nm\,nrad}$, $\varepsilon_y = 514\,\pi\,\mathrm{nm\,nrad}$, respectively. As the electron beam is injected and remains close to the propagation axis, it undergoes only relatively small betatron oscillations and is therefore resistant to emittance growth [278].

5.3 Varying the plasma grating amplitude and position

A set of simulations forming a multiparametric scan have been performed to investigate the effect of positioning and amplitude of the grating on the resulting electron beam properties. The plasma grating for each case is again formed using the 1-dimensional EPOCH code and the grating at maximum is used as a template and placed in the same plasma plateau as pictured in Fig. 5.1 for use in an FBPIC simulation. The plasma gratings are formed in hydrogen plasma with number density $n_0 = 1.75 \times 10^{18}\,\mathrm{cm}^{-3}$ by pump pulses with wavelength $\lambda_0 = 800\,\mathrm{nm}$ and temporal intensity full-width at half-maximum duration $\tau_0 = 330\,\mathrm{fs}$. The pump pulse peak dimensionless field strengths (intensities) lay in the range $0.0153 \leq a_0 \leq 0.0265$ ($5 \times 10^{14}\,\mathrm{W\,cm}^{-2} \leq I_0 \leq 1.5 \times 10^{15}\,\mathrm{W\,cm}^{-2}$). The plasma gratings are placed in the range $300\,\mathrm{\mu m} \leq x_i \leq 1100\,\mathrm{\mu m}$ in the plasma. Six equally spaced values of a_0 and nine equally spaced values of x_i form the 54 points of the parameter scan. The other simulation parameters are identical to those presented previously in this section.

Figs. 5.8 & 5.9 present simulations of the electron beams across the parameter space. All measurements are performed on the electron subspecies with $\gamma > 500$ after the beam exits the plasma. The total charge, q, charge-weighted average Lorentz factor, $\bar{\gamma}$, and charge-weighted RMS spread of the Lorentz factor, σ_γ, are shown in Fig. 5.8, and the x- and y-directional divergence, $\Theta_{x,y}$, and projected emittance, $\varepsilon_{x,y}$, in Fig. 5.9. Where values are weighted by charge, this weighting is chosen to give a value representative of the beam as a whole. Each measurement of the grating-assisted electron beam is normalised to the same measurement of the beam resulting from the equivalent case with no plasma grating. The upper and lower rows of panels in both figures present the same data, but use diverging and continuous colour schemes, respectively, to show both comparative and continuous trends. The diverging maps are centred on unity, such that red, blue, and white regions indicate poorer, improved, and similar electron beam parameters relative to the equivalent null case, respectively. The colour maps are directed assuming a higher charge, higher average energy, lower energy spread, lower divergence, lower emittance beam is of higher quality. While there is no immediately apparent trend in the relationship between the plasma grating parameters and the resulting electron beam quality, there are evidently regimes of the plasma grating-assisted laser wakefield accelerator that produce a higher quality beam than when using a drive laser alone. For instance, when the plasma grating pump pulses are set to $a_0 = 0.0275$ and the grating is placed at $x_i = 600\,\mu\text{m}$, the injected charge is enhanced by a factor of 11, the energy spread is reduced by a factor of 2, and the divergence and emittance are improved in both transverse directions.

5.4 Conclusions

The progress made in the field of laser wakefield acceleration since the seminal 1979 paper by Tajima & Dawson [112] has been enormous, but several challenges remain if the technology is to attain the grand goals proposed during early research. In particular, for LWFAs to provide state-of-the-art energetic particle beams and drive next-generation light sources, they must demonstrate an increase in beam charge from the several-pC regime whilst simultaneously reducing the energy spread to the sub-percent level and the emittance to the $\pi\,\mu\text{m}\,\mu\text{rad}$ level. Attosecond-scale (sub-femtosecond) bunch durations are also desirable as drivers of free electron lasers. So far, the simultaneous achievement of these parameters has been elusive.

Very fine control of every aspect of a plasma-based accelerator is necessary to attain optimal electron beam parameters. Several schemes (discussed previously) exist that enable the manipulation of the dynamics of electron bunch injection into the accelerator, which plays a key role in determining the resulting beam quality. The method of plasma grating-assisted electron bunch injection detailed in this chapter presents another set of tuneable parameters that can be used to control and improve the quality of electron beams from an LWFA. For instance, modification of the bubble velocity at the time of electron injection can lead to capturing of an order of magnitude more charge in the accelerating fields. Fine control of the bubble velocity can also be used to trigger electron injection that is very temporally localised, leading to ultrashort (sub-femtosecond) electron bunches.

The power required to produce plasma grating pump pulses is modest and readily

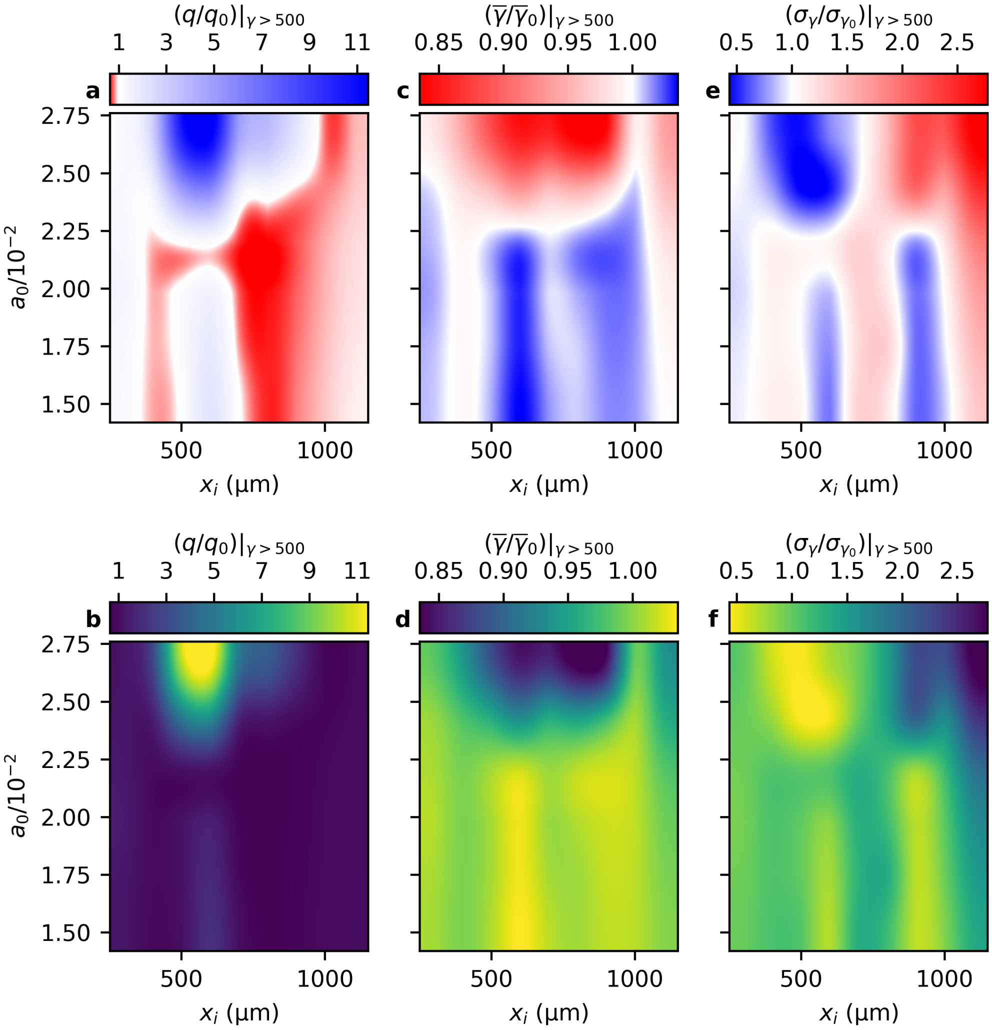

Figure 5.8: High-energy electron beam charge (**a**&**b**), charge-weighted average Lorentz factor (**c**&**d**), and charge-weighted Lorentz factor RMS spread (**e**&**f**) measurements from the plasma grating position and amplitude parameter scan. The upper and lower rows of panels show the same data presented with different colour scales. All values are normalised to the corresponding measurements when no plasma grating is present.

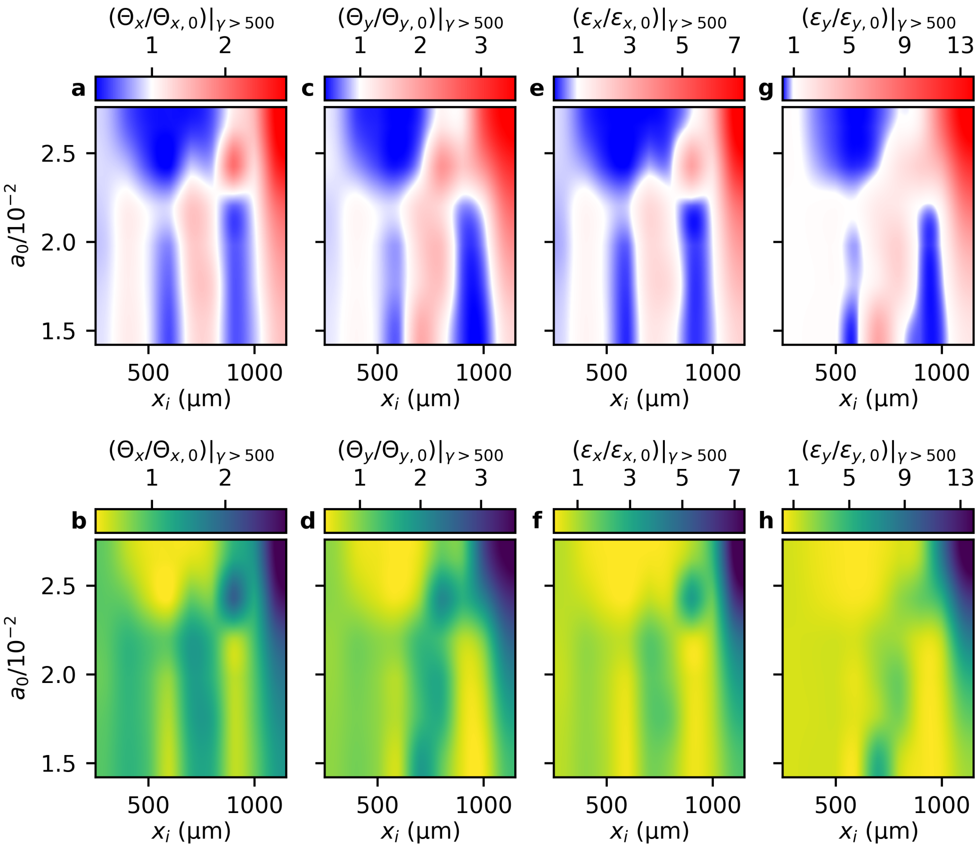

Figure 5.9: As Fig. 5.8 but showing the x- and y-directional divergence (**a**&**b** and **c**&**d**, respectively), and x- and y-directional projected emittance (**e**&**f** and **g**&**h**, respectively).

available from small-footprint, turnkey, commerical laser systems and therefore could be implemented in existing or bespoke systems.

The parameter space for plasma grating-assisted LWFAs is vast and the mechanism appears to be sensitive to the chosen configuration. Further study would therefore benefit from substantial compute to run high-throughput screening simulations so that promising parameter regions can be identified. Following this, high repetition rate experiments are desirable to rapidly converge on the optimal configuration identified by simulations.

Further lines of inquiry could investigate the mechanism by which the bubble velocity is altered by the plasma grating, which leads to injection, and thus predicts regimes of significant electron beam parameter improvement over the baseline case with no plasma grating. Other laser geometries could also be explored as well as more complex plasma density configurations to enable optimal bunch injection and acceleration. Based on the parameter scan results, it is likely that the plasma grating-assisted injection scheme is sensitive to laser noise and jitter. Therefore, future investigations to determine the required level of control over laser parameters to achieve reliable and reproducible enhancement of electron beams is required.

Chapter 6

Conclusions and future work

High-power lasers have driven significant scientific, technological, medical and industrial advancements since the invention of chirped-pulse amplification in the mid-1980s. Many innovative techniques have been developed to improve laser systems, enabling steady increases in available peak power, repetition rate and beam quality and decreases in pulse length. The per-unit-power footprint and cost of high-power laser systems has decreased, and a corresponding increase in usability has led to significant increases in the number of these devices in use worldwide.

The work described in this thesis is concerned with transient plasma density structures created by two or more intersecting high-power laser pulses in gas and plasma. Two kinds of structures are considered – (i) those produced in a plasma by the ponderomotive force associated with the beat wave of intersecting laser pulses, and (ii) those produced by ionisation of a neutral gas by overlapping laser pulses. In one dimension, the structures present as density gratings. Thus, those of type (i) are referred to as 'ponderomotive' or 'inertial gratings', while those of type (ii) are referred to as 'ionisation gratings'.

The dynamics of inertial gratings are investigated numerically using particle-in-cell simulations. It is shown that the formation time and maximum number density of one-dimensional plasma gratings depends on the intensity and duration of the pump beams. Through simulations with highly-resolved particle phase spaces, it is shown that collisions play a negligible role in the evolution of one-dimensional inertial gratings when compared with other parameters such as the laser intensity and pulse duration.

The creation of higher-dimensional plasma structures is made possible by departing from finite-duration plane wave pump pulses, or by intersecting more than two pump pulses. The spatial profiles of high-power laser pulses at focus often closely resemble Gaussian functions. It is shown through two-dimensional particle-in-cell simulations that inertial gratings formed by colliding two pump pulses with realistic far field profiles have properties dependent on the radial distance from the axis of propagation of the pump pulses. A three-dimensional 'egg box' inertial plasma structure is demonstrated by colliding six identical pump pulses.

The beat of two laser pulses colliding in neutral gas can give rise to an ionisation grating when the frequencies of the beams are degenerate or near-degenerate, and neither of the pulses is intense enough to ionise the gas by itself. If the resulting beat wave has an intensity peak that exceeds the ionisation threshold of the medium, plasma is formed in the antinodes of the wave and the gas remains un-ionised in the nodes. It is shown theoretically and demonstrated numerically that the medium undergoing ionisation facilitates the transfer of energy from the laser pulse with higher frequency to the pulse with lower frequency. This novel amplification mechanism sees energy flowing in the opposite direction to that of the Raman and Brillouin mechanisms. It is also shown that a residual non-evolving grating can persist after the laser-matter interaction. The residual grating can continue to scatter impinging laser light.

Inertial plasma gratings have been shown theoretically to have optical properties suitable for manipulating short-pulse, high-intensity lasers. This is advantageous compared with optical devices based on conventional solid state technology due to the higher damage thresholds and replenishable nature of plasma-based optical devices. One such proposed use is as a waveplate for manipulating the phase of a laser pulse. Through comprehensive two-dimensional particle-in-cell simulations, the effect of ionisation gratings in a single-shot plasma grating (in which the pump pulses are used both to ionise the neutral gas and drive the formation of an inertial plasma grating) are shown to be significant. The pulse duration, energy, phase and spectrum of a probe laser pulse are found to be modified by its interaction with an evolving ionisation grating. A parameter relating to the energy ratio between orthogonal field components of the probe laser measured by a polarisation diagnostic is identified. Through the use of Jones calculus, a model is developed to simulate its value for various arrival times, accounting for the change in phase and energy due to both the inertial and ionisation gratings.

An experimental investigation into transient plasma gratings is reported on. The experiment, performed at the Rutherford Appleton Laboratory's Central Laser Facility, consists of two identical, nearly-counterpropagating, picosecond-duration, high-power laser pulses colliding in a hydrogen gas target. The noses of the pulses ionise the gas and create an ionisation grating when they collide. A persistent ionisation grating also occurs in the wings of the interaction. The strong pump pulses eventually totally ionise the gas close to the axis of propagation, and drive the formation of an inertial plasma grating. A probe beam is derived from a leaky mirror before the final compression of one of the pump beams and separately compressed to 100 fs-duration. The beam's polarisation is changed to circular by a conventional waveplate and used to orthogonally probe the laser-matter interaction with varying arrival time. After the interaction, the probe polarisation and energy is measured using a device based on a Wollaston prism. Its integrated spectrum is also measured. The probe energy is found to vary with arrival time, peaking strongly at the early stages of the interaction before falling to unperturbed values. This corresponds to theoretical and numerical predictions of the probe being amplified due to its interaction with an evolving ionisation grating. The probe spectrum exhibits blue-shifting, which is also observed in simulation. The polarisation of the probe is also modified by the plasma grating to a degree dependent on its arrival time. In regimes where negligible amplification of the probe occurs, the previously-developed model based on Jones calculus can be used to calculate the relative phase shift between two orthogonal field components induced by the grating. The maximum phase shift observed is $\pi/4$.

Several lessons may be learned from the experiment above for the future development of a useful volume plasma grating-based waveplate for the manipulation of ultra-short, high-intensity laser pulses. The timing between the three beams is of paramount importance. The effect on the probe pulse due to its interaction with an ionisation grating (either evolving or residual) is also highly important. Several modifications to the configuration may be made in future experiments that are likely to reduce the deleterious effects[1] of the ionisation grating. For instance, shorter-duration pump pulses may be employed to temporally separate the initial momentum 'kick' provided to the plasma electrons and the eventual maximum of the grating. The structure may then be probed without the presence of the pump pulses and no energy transfer will take place between the pumps and probe. The pumps may also be polarised orthogonally to the probe pulse to prevent a beat wave forming between the pumps and probe. A combination of these and other techniques should be investigated in future experiments to improve the performance of the plasma grating waveplate.

The use of non-evolving, one-dimensional plasma gratings to control the behaviour of laser wakefield accelerators (LWFAs) is investigated with FBPIC, a quasi-three-dimensional particle-in-cell code. It is found that the presence of a large amplitude plasma grating in the path of an LWFA operating in the bubble regime can modify the velocity of the back of the bubble. Specifically, the velocity is suppressed in the density envelope up-ramp and enhanced in the down-ramp. The suppression can enable enhanced trapping of electrons in the accelerating bubble structure. Further investigations are required to determine the cause of the modification of the bubble velocity by the plasma grating. A multi-parametric scan of plasma grating pump pulse peak intensity and position in the LWFA target is performed. Several measurements are made of the resulting electron beam, including charge, average energy, energy spread, divergence, and emittance. All quantities are found to be controllable by the position and amplitude of the plasma grating, which can lead to enhanced tuneability of LWFAs. Computational resources limited investigation of non-cylindrically symmetric configurations. However, it is envisaged that a plasma grating formed by pump pulses that propagate perpendicularly to the accelerator axis may be suitable for controlling the phase velocity of the laser wakefield drive beam. This, in turn, may be a control mechanism for the bubble velocity and electron injection dynamics. Full three-dimensional

[1] Such effects include amplification, lengthening and blueshifting of the pulse and are detrimental to the beam quality in the context of the use of the plasma structure as a waveplate.

particle-in-cell simulations are necessary to follow this line of inquiry.

Appendix A

Gaussian pulse time-bandwidth product and chirp factor

A typical description of the temporal profile of a short laser pulse with linear frequency chirp is that of fast electric field oscillation enveloped by a Gaussian function [256]:

$$E(t) = \exp\left(\frac{-t^2}{\sigma^2}\right)\exp\left(\mathrm{i}\omega_0 t + \mathrm{i}\frac{\alpha t^2}{2}\right), \tag{A.1}$$

where σ is the standard deviation duration, ω_0 is the central angular frequency and α is the chirp factor. The instantaneous frequency is

$$\begin{aligned} \omega(t) &= \frac{\mathrm{d}}{\mathrm{d}t}\left(\omega_0 t + \frac{\alpha t^2}{2}\right) \\ &= \omega_0 t + \alpha t, \end{aligned} \tag{A.2}$$

and the intensity is given by

$$\begin{aligned} I(t) &= EE^* \\ &= \exp\left(\frac{-2t^2}{\sigma^2}\right), \end{aligned} \tag{A.3}$$

which drops to half of the maximum value when

$$\exp\left(\frac{-2t^2}{\sigma^2}\right) = \frac{1}{2} \tag{A.4}$$

and therefore the half-width at half-maximum time is

$$t_h = \sigma\left(\frac{1}{2}\ln(2)\right)^{\frac{1}{2}}. \tag{A.5}$$

The full-width at half-maximum duration is thus

$$\Delta t = \sigma\left(2\ln(2)\right)^{\frac{1}{2}}. \tag{A.6}$$

The Fourier transform of the electric field signal is

$$\begin{aligned}
\tilde{E}(\omega) &= \mathcal{F}(E) \\
&= \int_{-\infty}^{\infty} E(t)\exp(-\mathrm{i}\omega t)\,\mathrm{d}t \\
&= \left(\frac{-\pi\sigma^2}{\mathrm{i}\alpha\sigma^2/2-1}\right)^{\frac{1}{2}}\exp\left(\frac{\sigma^2\left(\omega-\omega_0\right)^2}{4}\right),
\end{aligned} \tag{A.7}$$

where the identity

$$\int_{-\infty}^{\infty}\exp\left(-\left(ax^2+bx\right)\right)\mathrm{d}x = \left(\frac{\pi}{a}\right)^{\frac{1}{2}}\frac{b^2}{4a} \tag{A.8}$$

has been used.

The power spectrum is

$$\tilde{E}\tilde{E}^* = \mathcal{A}\exp\left(\frac{-2\sigma^2\left(\omega-\omega_0\right)^2}{\alpha^2\sigma^4+4}\right), \tag{A.9}$$

where

$$\mathcal{A} = \left(\frac{-\pi\sigma^2}{\mathrm{i}\alpha\sigma^2/2-1}\right)^{\frac{1}{2}}\left(\frac{\pi\sigma^2}{\mathrm{i}\alpha\sigma^2/2+1}\right)^{\frac{1}{2}}. \tag{A.10}$$

Similarly to Eqn. (A.5), the half-width at half-maximum of the power spectrum occurs when

$$\exp\left(\frac{-2\sigma^2\omega^2}{\alpha^2\sigma^4+4}\right) = \frac{1}{2}, \tag{A.11}$$

so

$$\omega_h = \frac{1}{\sqrt{2}\sigma}\left(\ln(2)\left(\alpha^2\sigma^4+4\right)\right)^{\frac{1}{2}}, \tag{A.12}$$

and it follows that the full-width at half-maximum of the power spectrum is

$$\Delta\omega = \frac{1}{\sigma}\left(2\ln(2)\left(\alpha^2\sigma^4+4\right)\right)^{\frac{1}{2}}. \tag{A.13}$$

The time-bandwidth product can now be written as

$$\Delta\omega\Delta t = \left(4\ln(2)^2\left(\alpha^2\sigma^4+4\right)\right)^{\frac{1}{2}}. \tag{A.14}$$

Substituting $\sigma = \Delta t/\sqrt{2\ln(2)}$ gives

$$\Delta\omega\Delta t = \left(16\ln(2)^2+\alpha^2\Delta t^4\right)^{\frac{1}{2}}. \tag{A.15}$$

For a bandwidth-limited Gaussian pulse, this gives the well known result $\Delta\omega\Delta t \approx 2.77$.

Rearranging Eqn. (A.15) for α yields

$$\alpha = \frac{\left((\Delta\omega\Delta t)^2 - 16\ln(2)^2\right)}{\Delta t^2}. \tag{A.16}$$

Finally, consider a laser pulse with wavelength bandwidth $\Delta\lambda = \lambda_1 - \lambda_2$ (which is often an experimentally measurable quantity). The corresponding frequency bandwidth is

$$\begin{aligned}\Delta\nu &= \nu_2 - \nu_1 \\ &= \frac{c}{\lambda_2} - \frac{c}{\lambda_1} \\ &= \frac{-c\Delta\lambda}{\lambda_1\lambda_2}.\end{aligned} \tag{A.17}$$

Assuming $\Delta\lambda \ll \lambda$ (and therefore that $\lambda_1 \approx \lambda_2 \approx \lambda_0$, where λ_0 is the central wavelength),

$$\Delta\nu = \frac{c}{\lambda_0^2}\Delta\lambda. \tag{A.18}$$

The relation $\omega = 2\pi\nu$ may then be used along with Eqn. (A.16) to determine α.

Appendix B

Energy in a laser pulse

The energy contained in the fields of a laser pulse, $\mathcal{E}$, is related to the power P, by

$$\mathcal{E} = \int_{-\infty}^{\infty} P(t)\,\mathrm{d}t = \int_{-\infty}^{\infty} \mathrm{d}t \int \mathrm{d}A_{\perp} \vec{I}(t, \vec{x}), \tag{B.1}$$

where $\mathrm{d}A_{\perp}$ is the area derivative in the direction perpendicular to the pulse propagation and $\vec{I}(t, \vec{x})$ is the spatiotemporal intensity profile, which is related to the electric field by

$$\vec{I}(t, \vec{x}) = c\varepsilon_0 \left| \vec{E}(t, \vec{x}) \right|^2 . \tag{B.2}$$

The field strength defined in Eqn. (2.22) can also be written

$$\vec{a} = \frac{e\lambda}{2\pi m_e c^2} \vec{E} = \lambda \left(\frac{c\varepsilon_0}{\mathcal{B}} \right)^{\frac{1}{2}} \vec{E}, \tag{B.3}$$

where $\mathcal{B} = c\varepsilon_0 \left(2\pi m_e c^2 / e \right)^2 \simeq 2.74 \times 10^{10}\,\mathrm{W}$. The intensity is then

$$\vec{I}(t, \vec{x}) = \mathcal{B} \left| \frac{\vec{a}(t, \vec{x})}{\lambda} \right|^2 , \tag{B.4}$$

and Eqn. (B.1) can be rewritten as

$$\begin{aligned} \mathcal{E} &= c\varepsilon_0 \int_{-\infty}^{\infty} \mathrm{d}t \int \mathrm{d}A_{\perp} |\vec{E}(t, \vec{x})|^2 \\ &= \frac{a}{\lambda^2} \int_{-\infty}^{\infty} \mathrm{d}t \int \mathrm{d}A_{\perp} |\vec{a}(t, \vec{x})^2 , \end{aligned} \tag{B.5}$$

where $\mathrm{d}A_\perp = \mathrm{d}^2\vec{x}_\perp$ in Cartesian coordinates and $\mathrm{d}A_\perp = r\,\mathrm{d}r\,\mathrm{d}\theta$ in polar coordinates. In discrete 2-dimensional Cartesian geometry (such as in the 2-dimension particle-in-cell simulation method), the energy can be found by assuming cylindrical symmetry of the pulse.

Appendix C

Simulation input files

The following sections contain EPOCH and FBPIC simulation steering files used in the various studies presented in this thesis.

C.1 Laser wakefield accelerator in the bubble regime

Following is the steering file for an FBPIC simulation of a laser wakefield accelerator in the bubble regime driven by a matched laser pulse.

```python
# -------
# Imports
# -------
import numba
import math
import numpy as np
from scipy.constants import c, m_e, m_p, e, epsilon_0, pi

from fbpic.main import Simulation
from fbpic.lpa_utils.laser import add_laser, GaussianLaser
from fbpic.openpmd_diag import (FieldDiagnostic, ParticleDiagnostic,
                                set_periodic_checkpoint,
                                restart_from_checkpoint)

# ----------
# Parameters
# ----------

# Whether to use the GPU
use_cuda = True

# Scaling factors
fwhm_I_to_F = np.sqrt(2)
fwhm_to_width = 1./(2*np.sqrt(np.log(2)))

# Plasma parameters
n0 = 1.0e24                                 # Density
wp = e * np.sqrt(n0 / (epsilon_0 * m_e))   # Frequency
lp = 2 * pi * c / wp                        # Wavelength
kp = wp / c                                 # Wavenumber

```

```
ramp_length = 100e-6
plateau_length = 2.0e-3

# Laser parameters
a0 = 4.0                                # Dimensionless field strength
w0 = 2 * np.sqrt(a0) / kp               # Waist size
fwhm0_I = w0 / 2 / c                    # Intensity FWHM duration
fwhm0_F = fwhm0_I * fwhm_I_to_F         # Field envelope FWHM duration
ctau0 = c * fwhm0_F * fwhm_to_width
z0 = -3*ctau0
lambda0 = 800e-9                        # Wavelength
zf = ramp_length                        # Focal point

# Grid points and box size
dz_cell = 40e-9                             # Cell size in z
zmax = 0
zmin = -80e-6
Nz = int( (zmax - zmin) / dz_cell ) + 1    # Number of cells along z
zmin = zmax - Nz * dz_cell
Nr = 1000                                   # Number of cells along r
rmax = 70e-6
Nm = 3                                      # Number of azimuthal modes

# The simulation timestep
dt = dz_cell/c    # Timestep (seconds)
N_step = int(round((2*ramp_length + plateau_length + (zmax-zmin))/dz_cell))

# Order of the stencil for z derivatives in the Maxwell solver
# See https://arxiv.org/abs/1611.05712 for more information
n_order = 32

# The particles
p_zmin = 0        # Position of the beginning of the plasma
p_zmax = 2*ramp_length + plateau_length # End of the plasma
p_rmin = 0.       # Minimal radial position of the plasma
p_rmax = 65e-6    # Maximal radial position of the plasma
p_nz = 3          # Number of particles per cell along z
p_nr = 2          # Number of particles per cell along r
p_nt = 8          # Number of particles per cell along theta

# The diagnostics and the checkpoints/restarts
diag_dist = 20e-6  # Window move distance between snapshots
diag_period = int(round(diag_dist/dz_cell))
save_checkpoints = False
checkpoint_period = int( round(1e-3/dz_cell) )
use_restart = False
track_particles = True

def electron_dens_func( z, r ):
    n = np.ones_like(z)
    numba_electron_dens_func( n, z, r )
    return n

@numba.jit
def numba_electron_dens_func( n, z, r ):
    for i in range(len(z)):
        # Vacuum
        if z[i] < 0:
            n[i] = 0
        # Coupling up ramp
        elif z[i] < ramp_length:
            n[i] = 0.5*(1 - np.cos(pi*z[i]/ramp_length))
        # Plateau
        elif z[i] < ramp_length + plateau_length:
            n[i] = 1
        # Coupling down ramp
        elif z[i] < 2*ramp_length + plateau_length:
```

```
            n[i] = 0.5*(1 + np.cos(pi*(z[i] - \
                   (ramp_length + plateau_length))/ramp_length))
        # Vacuum
        else:
            n[i] = 0


# --------------------------
# Simulation
# --------------------------

temperature_eV = 0
u_th = np.sqrt(temperature_eV*e/(m_e*c**2))

if __name__ == '__main__':

    # Initialize the simulation object
    sim = Simulation(
        Nz, zmax, Nr, rmax, Nm, dt,
        zmin=zmin,
        boundaries={'z':'open', 'r':'reflective'},
        initialize_ions=False,
        verbose_level=2,
        n_order=n_order,
        use_cuda=use_cuda,
        particle_shape='cubic',
        n_damp={'r': 100, 'z': 64}
    )

    sim.add_new_species(
        q=-e, m=m_e, n=n0,
        dens_func=electron_dens_func,
        p_nz=p_nz, p_nr=p_nr, p_nt=p_nt,
        p_zmin=p_zmin, p_zmax=p_zmax,
        p_rmin=p_rmin, p_rmax=p_rmax,
        ux_m=0, ux_th=u_th,
        uy_m=0, uy_th=u_th,
        uz_m=0, uz_th=u_th
    )

    if use_restart is False:
        add_laser(
            sim,
            a0=a0,
            w0=w0,
            ctau=ctau0,
            z0=z0,
            zf=zf,
            lambda0=lambda0,
            theta_pol=pi/2
        )
        # Track electrons if required
        if track_particles:
            sim.ptcl[0].track(sim.comm)
    else:
        # Load the fields and particles from the latest checkpoint file
        restart_from_checkpoint(sim)
        N_step -= sim.iteration

    # Set moving window
    sim.set_moving_window(v=c)

    # Add diagnostics
    sim.diags = [
        FieldDiagnostic(diag_period, sim.fld, comm=sim.comm),
        ParticleDiagnostic(
            diag_period,
            {"electrons" : sim.ptcl[0]},
```

```
            select={"gamma" : [100, None]},
            comm=sim.comm
        )
    ]

    # Add checkpoints
    if save_checkpoints:
        set_periodic_checkpoint(sim, checkpoint_period)

    # Run the simulation
    sim.step(N_step)
    print('')
```

C.2 One-dimensional inertial plasma grating

The following EPOCH input deck controls a high-resolution simulation to investigate the formation of a 1-dimensional inertial plasma grating.

```
begin:constant

    # Laser parameters
    # ----------------

        # Central wavelength and frequency
        lambda_0 = 800e-9
        omega_0 = 2.0 * pi * c / lambda_0

        # Peak intensity
        I_0 = 1e15  # W/cm^2

        # Pulse duration
        T_FWHM_I = 250.0 * femto                # Intensity FWHM
        T_FWHM_E = T_FWHM_I * sqrt(2.0)         # Field envelope FWHM
        T_E = T_FWHM_E / 2.0 / sqrt(loge(2.0))  # Field envelope waist
        T_0 = 3.0 * T_E                         # Temporal centre


    # Plasma parameters
    # -----------------

        # Initial plasma density
        n_0 = 0.1 * critical(omega_0)

        # Plateau and ramp lengths
        L_plateau = 4.0 * lambda_0
        L_ramp = 2.0 * lambda_0

        # Ramp gradient
        m_ramp = n_0 / L_ramp

        # Vacuum length
        L_vac = 1.0 * lambda_0

        # Electron and ion temperature
        T_electron = 5.0  # eV
        T_ion = T_electron / 10.0

    # Simulation parameters
    # ---------------------

        # Cells per laser wavelength
        cpw_x = 500

        # Macroparticles per cell
```

```
        ppc = nint(2^11)

        # Simulation end time
        T_end = T_0 + 4.0 * pico

        # Window length
        x_len = L_plateau + 2.0 * L_ramp + 2.0 * L_vac

        # Coordinate of centre of window
        x_centre = x_len / 2

end:constant



begin:control

    stdout_frequency = 100

    nx = ceil((cpw_x * x_len) / lambda_0)

    x_min = 0.0
    x_max = x_len

    t_end = T_end

end:control



begin:boundaries

    bc_x_min = simple_laser
    bc_x_max = simple_laser

end:boundaries



begin:species

    name = electron
    charge = -1.0
    mass = 1.0
    nparticles_per_cell = ppc

    number_density = 0
    number_density = if(x gt L_vac, m_ramp * (x - L_vac), number_density(
    electron))
    number_density = if(x gt L_vac + L_ramp, n_0, number_density(electron))
    number_density = if(x gt L_vac + L_ramp + L_plateau, -m_ramp * (x -
    L_vac - 2.0 * L_ramp - L_plateau), number_density(electron))
    number_density = if(x gt L_vac + 2.0 * L_ramp + L_plateau, 0,
    number_density(electron))

    number_density_min = 0.01 * n_0

    temperature_ev = T_electron

end:species



begin:species

    name = ion
    charge = 1.0
    mass = 1836.0
    nparticles_per_cell = ppc

    number_density = number_density(electron)
```

```

    number_density_min = 0.01 * n_0

    temperature_ev = T_ion

end:species



begin:laser

    boundary = x_min
    intensity_w_cm2 = I_0
    lambda = lambda_0
    t_profile = gauss(time, T_0, T_E)

end:laser



begin:laser

    boundary = x_max
    intensity_w_cm2 = I_0
    lambda = lambda_0
    t_profile = gauss(time, T_0, T_E)

end:laser



begin:dist_fn

    name = px_electron
    ndims = 1
    dumpmask = always
    include_species:electron

    direction1 = dir_px
    range1 = (-5.36e-24, 5.36e-24)
    resolution1 = 2000
    restrict_x = (x_centre - lambda_0, x_centre + lambda_0)

end:dist_fn



begin:dist_fn

    name = px_ion
    ndims = 1
    dumpmask = always
    include_species:ion

    direction1 = dir_px
    range1 = (-1.34e-22, 1.34e-22)
    resolution1 = 2000
    restrict_x = (x_centre - lambda_0, x_centre + lambda_0)

end:dist_fn



begin:subset

    name = electron_sub
    include_species:electron
    dumpmask = always
    x_min = x_centre - lambda_0
    x_max = x_centre + lambda_0

```

```
end:subset


begin:subset

    name = ion_sub
    include_species:ion
    dump = always
    x_min = x_centre - lambda_0
    x_max = x_centre + lambda_0

end:subset


begin:output

    dt_snapshot = t_end / 1000.0

    particles = electron_sub + ion_sub
    id = electron_sub + ion_sub

    grid = always
    ex = always
    jx = always
    number_density = always + species

    distribution_functions = always

end:output
```

C.3 Pump-probe ionisation grating parameter scan template

The below EPOCH input deck defines a simulation that comprises a parameter coordinate in the multiparametric scan investigating the three-beam pump-probe ionisation grating interaction detailed in Sec. 3.2.3. The lines labelled '`AUTO GENERATED`' are generated by a script that controls the parameter scan.

```
begin:constant

    # ##########
    # Simulation

        # Particles per cell per species
        ppc = 32

        # Cells per laser wavelength (800 nm) in each direction
        cpw_x = 40
        cpw_y = 40

        # Boundary coordinates
        xmin = -7 * micro
        xmax = 7 * micro
        ymin = -5 * micro
        ymax = 60 * micro

        xlen = xmax - xmin
        ylen = ymax - ymin
```

```

    # ######
    # Plasma

        # Initial gas density
        n0 = 6e25

        # Gas lengths
        plasma_l_x = 10 * micro
        plasma_l_y = 10 * micro

    # ######
    # Lasers

        ##
        ## Pumps

            # Central wavelength
            lambda_0_pump = 7.4e-07 # AUTO GENERATED

            # Peak intensity, watts per square centimetre
            I_pump = 10000000000000.0 # AUTO GENERATED

        ##
        ## Probe

            # Central wavelength
            lambda_0_probe = 800 * nano

            # Peak intensity, watts per square centimetre
            I_probe = 1e13

            # Relative delay of probe
            # Defined as the time difference between either pump reaching the opposite side of the plasma (e.g. the left pump reaching the right side of the plasma) and the leading edge of the probe reaching the bottom edge of the plasma
            t_delay_probe = 0

            # Pulse duration
            t_probe = 50 * femto

            # Time the probe is switched on
            t_on_probe = (xlen - plasma_l_x) / 2 / c + plasma_l_x / c - abs(y_min) / c + t_delay_probe

            # Time centre of the probe
            t_centre_probe = t_on_probe + t_probe / 2

            # Phase
            phi = 0

end:constant



begin:control

    stdout_frequency = 100

    x_min = xmin
    x_max = xmax
    y_min = ymin
    y_max = ymax

    nx = (cpw_x * (xmax - xmin)) / 800e-9
    ny = (cpw_y * (ymax - ymin)) / 800e-9

    # End simulation when probe reaches 2 um of ymax boundary
    t_end = t_on_probe + (ylen - 2 * micro) / c
```

```

    field_ionisation = T
    use_multiphoton = F

end:control


begin:boundaries

    bc_x_min = simple_laser
    bc_x_max = simple_laser
    bc_y_min = simple_laser
    bc_y_max = simple_outflow

end:boundaries


begin:species

    name = hydrogen
    charge = 0.0
    mass = 1836.0
    nparticles_per_cell = ppc

    ionisation_energies = (13.6 * ev)
    ionisation_electron_species = electron

    number_density = if((abs(x) gt plasma_l_x / 2), 0, n0)
    number_density = if((y gt plasma_l_y), 0, number_density(hydrogen))
    number_density = if((y lt 0), 0, number_density(hydrogen))

    number_density_min = 0.05 * n0

end:species


begin:species

    name = electron
    charge = -1.0
    mass = 1.0
    number_density = 0

end:species


begin:laser

    # Pump from left

    boundary = x_min
    intensity_w_cm2 = I_pump
    lambda = lambda_0_pump
    pol = 90.0

    profile = supergauss(y, plasma_l_y / 2, (plasma_l_y / 2) * 1.2, 10)

end:laser


begin:laser

    # Pump from right

    boundary = x_max
    intensity_w_cm2 = I_pump
```

```
    lambda = lambda_0_pump
    pol = 90.0

    profile = supergauss(y, plasma_l_y / 2, (plasma_l_y / 2) * 1.2, 10)

end:laser



begin:laser

    # Probe from bottom

    boundary = y_min
    intensity_w_cm2 = I_probe
    lambda = lambda_0_probe
    pol = 45
    phase = phi

    profile = supergauss(x, 0, (plasma_l_x / 2) * 1.1, 10)
    t_profile = supergauss(time, t_centre_probe, t_probe/2, 20)

end:laser



begin:output

    particles = never

    grid = always
    ex = always
    ey = never
    ez = always

    poynting_flux = always

end:output
```

C.4 Pump-probe ionisation and ponderomotive grating interaction probe delay scan

The following EPOCH input deck is for a simulation investigating the pump-probe ionisation and ponderomotive grating interaction discussed in Sec. 3.3. The variable T_delay_probe, defined on line 67, was varied to form the delay scan.

```
1  begin:constant
2
3      # ##########
4      # Simulation
5
6          # Particles per species per cell
7          ppc = 8
8
9          # Cells per central laser wavelength in each direction
10         cpw_x = 60
11         cpw_y = 60
12
13         # Boundary coordinates
14         xmin = -25 * micro
15         xmax = 25 * micro
```

```
        ymin = -10 * micro
        ymax = 306 * micro

        xlen = xmax - xmin
        ylen = ymax - ymin

    # ######
    # Plasma

        # Initial plasma density
        n0 = 6e25

        # Plasma lengths
        plasma_l_x = 40 * micro
        plasma_l_y = 96 * micro

    # ######
    # Lasers

        # Central wavelength
        lambda0 = 800 * nano
        # Corresponding angular frequency
        omega0 = 2 * pi * c / lambda0

        ##
        ## Pumps

            ###
            ### Temporal profile

                T_FWHM_pump_I = 1 * pico  # Intensity FWHM
                T_FWHM_pump = T_FWHM_pump_I * sqrt(2)  # Field envelope FWHM
                T_w_pump = T_FWHM_pump / 2 / sqrt(loge(2))  # Field envelope Gaussian waist
                T_w_pump_I = T_FWHM_pump_I / 2 / sqrt(loge(2))  # Intensity Gaussian waist

                # Temporal centre
                T_centre_pump = T_w_pump * 2.5

                # Chirp factor
                alpha = 7.35297e25

            # Spatial profile
            w_pump = 16 * micro  # Field envelope Gaussian waist

        ##
        ## Probe

            # Temporal profile
            T_w_probe = 85 * femto  # Field envelope Gaussian waist radius

            # Temporal delay with respect to colliding all three beams in the centre of the plasma
            T_delay_probe = -1.70 * pico
            T_centre_probe = T_centre_pump + (xlen / 2 / c) - ((plasma_l_y / 2 + abs(ymin)) / c) + T_delay_probe

            # Spatial profile
            w_probe = 6.6 * micro

end:constant



begin:control

    stdout_frequency = 100

    x_min = xmin
```

```
    x_max = xmax
    y_min = ymin
    y_max = ymax

    nx = (cpw_x * (xmax - xmin)) / lambda0
    ny = (cpw_y * (ymax - ymin)) / lambda0

    # Timing end of simulation such that the centre of the probe is 75
    microns from the ymax boundary
    t_end = T_centre_probe + (ylen - 75 * micro) / c

    field_ionisation = T
    use_multiphoton = F

end:control



begin:boundaries

    bc_x_min = simple_laser
    bc_x_max = simple_laser
    bc_y_min = simple_laser
    bc_y_max = simple_outflow

end:boundaries



begin:species

    name = hydrogen
    charge = 0.0
    mass = 1836.0
    nparticles_per_cell = ppc

    ionisation_energies = (13.6 * ev)
    ionisation_electron_species = electron

    number_density = if((abs(x) gt plasma_l_x / 2), 0, n0)
    number_density = if((y gt plasma_l_y), 0, number_density(hydrogen))
    number_density = if((y lt 0), 0, number_density(hydrogen))

end:species



begin:species

    name = electron
    charge = -1.0
    mass = 1.0
    number_density = 0

end:species



begin:laser

    # Pump from left

    boundary = x_min
    intensity_w_cm2 = 5.0e15
    omega = omega0 + alpha * (time - T_centre_pump)
    pol = 90.0

    profile = gauss(y, plasma_l_y / 2, w_pump)
    t_profile = gauss(time, T_centre_pump, T_w_pump)

end:laser
```

```
begin:laser

    # Pump from right

    boundary = x_max
    intensity_w_cm2 = 5.0e15
    omega = omega0 + alpha * (time - T_centre_pump)
    pol = 90

    profile = gauss(y, plasma_l_y / 2, w_pump)
    t_profile = gauss(time, T_centre_pump, T_w_pump)

end:laser



begin:laser

    # Probe from bottom

    boundary = y_min
    intensity_w_cm2 = 1.0e13
    lambda = lambda0
    pol = 45

    profile = gauss(x, 0, w_probe)
    t_profile = gauss(time, T_centre_probe, T_w_probe)

end:laser



begin:output

    particles = never

    grid = always
    ex = always
    ey = always
    ez = always

    number_density = always + species

end:output
```

C.5 One-dimensional inertial plasma grating for use in a laser wakefield accelerator

The following input deck for a 1-dimensional EPOCH simulation generates an inertial plasma grating for use in the parallel geoemtry of the plasma grating-assisted laser wakefield acceleration scheme described in Ch. 5.

```
begin:constant

    # ######
    # Plasma

        # Initial gas density
        n0 = 1.75e+24
```

```

        # Plasma length
        plasma_l_x = 400 * micro

    # ######
    # Lasers

        # Central wavelength
        lambda_0 = 800 * nano

        # Peak intensity, watts per square centimetre
        I_0 = 9e14

        # Pulse duration
        T_FWHM_I = 3.3e-13  # Intensity FWHM
        T_FWHM = T_FWHM_I * sqrt(2)  # Field envelope FWHM
        T_w = T_FWHM / 2 / sqrt(loge(2))  # Field envelope Gaussian waist

        # Temporal centre
        T_centre = T_w * 2.5

    # ##########
    # Simulation

        # Particles per cell per species
        ppc = 128

        # Cells per 800 nm
        cpw_x = 40

        # Boundary coordinates
        xlen = 5 * c * T_FWHM_I
        xmin = -xlen / 2
        xmax = -xmin

begin:control



begin:control

    stdout_frequency = 100

    x_min = xmin
    x_max = xmax

    nx = (cpw_x * xlen) / lambda_0

    # End of simulation timed to be 1 ps after pump pulse overlap
    t_end = T_centre + xlen / 2 / c + 1 * pico

end:control



begin:boundaries

    bc_x_min = simple_laser
    bc_x_max = simple_laser

end:boundaries



begin:species

    name = electron
    charge = -1.0
    mass = 1.0
    nparticles_per_cell = ppc

```

```
    number_density = n0
    number_density = if(abs(x) gt plasma_l_x / 2, 0, n0)
    number_density_min = 0.05 * n0

end:species


begin:species

    name = ion
    charge = 1.0
    mass = 1836.0

    number_density = number_density(electron)

end:species


begin:laser

    # Pump from left

    boundary = x_min
    intensity_w_cm2 = I_0
    lambda = lambda_0
    t_profile = gauss(time, T_centre, T_w)
    t_end = T_centre + 3 * T_w

end:laser


begin:laser

    # Pump from right

    boundary = x_max
    intensity_w_cm2 = I_0
    lambda = lambda_0
    t_profile = gauss(time, T_centre, T_w)
    t_end = T_centre + 3 * T_w

end:laser


begin:output

    dt_snapshot = 50e-15

    particles = never

    grid = always
    ex = never
    ey = never
    ez = never

    number_density = always + species

end:output
```

C.6 Plasma grating-assisted laser wakefield acceleration

The following FBPIC steering file controls a plasma grating-assisted laser wakefield accelerator simulation in the parallel geometry, as described in Sec. 5.2. It takes as input a csv file with position-density pairs to define the plasma grating (see Sec. 5.1 and Appx. C.5). For the equivalent simulation without the plasma grating present, the `numba_electron_dens_func` function is modified to not include the grating and transition regions.

```python
# -------
# Imports
# -------
import numba
import math
import sys
import numpy as np
from scipy.constants import c, m_e, m_p, e, epsilon_0, pi
from scipy.interpolate import interp1d

from fbpic.main import Simulation
from fbpic.lpa_utils.laser import add_laser, GaussianLaser
from fbpic.openpmd_diag import (FieldDiagnostic, ParticleDiagnostic,
                                set_periodic_checkpoint,
                                restart_from_checkpoint)

# ----------
# Parameters
# ----------

# Whether to use the GPU
use_cuda = True

# Plasma profile parameters
bump_centre = 0.3e-3
bump_width = 3e-4
bump_pad = 1.5e-5
ramp_length = 100e-6
plateau_length = 1.799e-3

n0 = 1.75e24                                # Density
wp = e * np.sqrt(n0 / (epsilon_0 * m_e))    # Frequency
lp = 2 * pi * c / wp                        # Wavelength
kp = wp / c                                 # Wavenumber

# Plasma grating profile
profile_data = np.loadtxt(
    sys.argv[1],  # Path to csv data
    skiprows=1,
    delimiter=','
)
z_data = profile_data[:, 0]
n_data = profile_data[:, 1]

n_data_interp = interp1d(z_data, n_data/n0, kind="cubic")

# Scaling
fwhm_I_to_F = np.sqrt(2)
fwhm_to_width = 1. / (2 * np.sqrt(np.log(2)))

# Laser
```

```
a0 = 3.5
w0 = 2 * np.sqrt(a0) / kp
fwhm0_I = w0 / 2 / np.sqrt(2) / c
fwhm0_F = fwhm0_I * fwhm_I_to_F
ctau0 = c * fwhm0_F * fwhm_to_width
z0 = -3 * ctau0
lambda0 = 800e-9
zf = ramp_length

# Grid points, resolution and box size
dz_cell = 40e-9
dr_cell = 70e-9
zmax = 0
zmin = -50e-6
Nz = int( (zmax - zmin) / dz_cell ) + 1
zmin = zmax - Nz * dz_cell
rmax = 3.5 * w0
Nr = int( rmax / dr_cell ) +1
Nm = 3

# The simulation timestep
dt = dz_cell / c
N_step = int(round((2 * ramp_length + plateau_length + \
                    2 * (zmax - zmin)) / dz_cell))

# Order of the stencil for z derivatives in the Maxwell solver
# See https://arxiv.org/abs/1611.05712 for more information
n_order = 32

# Particles
p_zmin = 0   # Position of the beginning of the plasma
p_zmax = 2 * ramp_length + plateau_length    # End of the plasma
p_rmin = 0.           # Minimal radial position of the plasma
p_rmax = 0.95 * rmax  # Maximal radial position of the plasma
p_nz = 3              # Number of particles per cell along z
p_nr = 2              # Number of particles per cell along r
p_nt = 8              # Number of particles per cell along theta

# The diagnostics and the checkpoints/restarts
diag_dist = 10e-6
diag_period = int(round(diag_dist/dz_cell))
save_checkpoints = False
checkpoint_period = int( round(1e-3/dz_cell) )
use_restart = False
track_particles = True

def electron_dens_func( z, r ):
    n = np.ones_like(z)
    numba_electron_dens_func( n, z, r )
    return n

@numba.jit
def numba_electron_dens_func( n, z, r ):
    for i in range(len(z)):
        # Vacuum
        if z[i] < 0:
            n[i] = 0
        # Entrance ramp
        elif z[i] < ramp_length:
            n[i] = 0.5 * (1 - np.cos(pi * z[i] / ramp_length))
        # Plateau before grating
        elif z[i] < bump_centre - bump_width / 2:
            n[i] = 1
        # Transition between plateau and grating
        elif z[i] < bump_centre - bump_width / 2 + bump_pad:
            n[i] = (n_data_interp(z[i] - bump_centre) - 1) * \
                    (1 / bump_pad) * \
```

```
                    (z[i] - (bump_centre - bump_width / 2)) + 1
        # Grating
        elif z[i] < bump_centre + bump_width / 2 - bump_pad:
            n[i] = n_data_interp(z[i] - bump_centre)
        # Transition between grating and plateau
        elif z[i] < bump_centre + bump_width / 2:
            n[i] = (n_data_interp(z[i] - bump_centre) - 1) * \
                   (-1 / bump_pad) * \
                   (z[i] - (bump_centre + bump_width / 2)) + 1
        # Plateau
        elif z[i] < ramp_length + plateau_length:
            n[i] = 1
        # Exit ramp
        elif z[i] < 2*ramp_length + plateau_length:
            n[i] = 0.5*(1 + np.cos(pi*(z[i] - (ramp_length + \
                   plateau_length))/ramp_length))
        # Vacuum
        else:
            n[i] = 0


# --------------------------
# Simulation
# --------------------------

temperature_eV = 0
u_th = np.sqrt(temperature_eV*e/(m_e*c**2))

if __name__ == '__main__':

    # Initialize the simulation object
    sim = Simulation(
        Nz, zmax, Nr, rmax, Nm, dt,
        zmin=zmin,
        boundaries={'z':'open', 'r':'reflective'},
        initialize_ions=False,
        verbose_level=2,
        n_order=n_order,
        use_cuda=use_cuda,
        particle_shape='cubic',
        n_damp={'r': 100, 'z': 64}
    )

    sim.add_new_species(
        q=-e, m=m_e, n=n0,
        dens_func=electron_dens_func,
        p_nz=p_nz, p_nr=p_nr, p_nt=p_nt,
        p_zmin=p_zmin, p_zmax=p_zmax,
        p_rmin=p_rmin, p_rmax=p_rmax,
        ux_m=0, ux_th=u_th,
        uy_m=0, uy_th=u_th,
        uz_m=0, uz_th=u_th
    )

    if use_restart is False:
        add_laser(
            sim,
            a0=a0,
            w0=w0,
            ctau=ctau0,
            z0=z0,
            zf=zf,
            lambda0=lambda0,
            theta_pol=pi/2
        )
        # Track electrons if required
        if track_particles:
```

```
            sim.ptcl[0].track(sim.comm)
    else:
        # Load the fields and particles from the latest checkpoint file
        restart_from_checkpoint(sim)
        N_step -= sim.iteration

    # set moving window
    sim.set_moving_window(v=c)

    # Add diagnostics
    sim.diags = [
        FieldDiagnostic(
            diag_period,
            sim.fld,
            comm=sim.comm
        ),
        ParticleDiagnostic(
            diag_period,
            {"electrons" : sim.ptcl[0]},
            select={"gamma" : [25, None]},
            comm=sim.comm,
            particle_data=[
                'position',
                'momentum',
                'weighting',
                'gamma'
            ]
        )
    ]

    # Add checkpoints
    if save_checkpoints:
        set_periodic_checkpoint(sim, checkpoint_period)

    # Run the simulation
    sim.step(N_step)
    print('')
```

Bibliography

[1] Strickland, D. and Mourou, G. "Compression of amplified chirped optical pulses." *Optics Communications*, **56** (1985) 219. doi:10.1016/0030-4018(85)90120-8.

[2] "The International Committee on Ultra-High Intensity Lasers." `https://www.icuil.org/`.

[3] Backus, S., Durfee, C. G., *et al.* "High power ultrafast lasers." *Review of Scientific Instruments*, **69** (1998) 1207. doi:10.1063/1.1148795.

[4] Esarey, E., Schroeder, C. B., *et al.* "Physics of laser-driven plasma-based electron accelerators." *Reviews of Modern Physics*, **81** (2009) 1229. doi:10.1103/RevModPhys.81.1229.

[5] Macchi, A., Borghesi, M., *et al.* "Ion acceleration by superintense laser-plasma interaction." *Reviews of Modern Physics*, **85** (2013) 751. doi:10.1103/RevModPhys.85.751.

[6] Corde, S., Ta Phuoc, K., *et al.* "Femtosecond x rays from laser-plasma accelerators." *Reviews of Modern Physics*, **85** (2013) 1. doi:10.1103/RevModPhys.85.1.

[7] Albert, F. and Thomas, A. G. R. "Applications of laser wakefield accelerator-based light sources." *Plasma Physics and Controlled Fusion*, **58** (2016) 103001. doi:10.1088/0741-3335/58/10/103001.

[8] Suzuki-Vidal, F., Li, Y., *et al.* "Editorial review of HPLSE special issue on laboratory astrophysics." *High Power Laser Science and Engineering*, **7** (2019/ed). doi:10.1017/hpl.2019.2.

[9] Takabe, H. and Kuramitsu, Y. "Recent progress of laboratory astrophysics with intense lasers." *High Power Laser Science and Engineering*, **9** (2021/ed). doi: 10.1017/hpl.2021.35.

[10] Betti, R. and Hurricane, O. A. "Inertial-confinement fusion with lasers." *Nature Physics*, **12** (2016) 435. doi:10.1038/nphys3736.

[11] Kneip, S., McGuffey, C., *et al.* "Bright spatially coherent synchrotron X-rays from a table-top source." *Nature Physics*, **6** (2010) 980. doi:10.1038/nphys1789.

[12] Hussein, A. E., Senabulya, N., *et al.* "Laser-wakefield accelerators for high-resolution X-ray imaging of complex microstructures." *Scientific Reports*, **9** (2019) 3249. doi:10.1038/s41598-019-39845-4.

[13] Cole, J. M., Wood, J. C., *et al.* "Laser-wakefield accelerators as hard x-ray sources for 3D medical imaging of human bone." *Scientific Reports*, **5** (2015) 13244. doi:10.1038/srep13244.

[14] Fourmaux, S., Corde, S., *et al.* "Single shot phase contrast imaging using laser-produced Betatron x-ray beams." *Optics Letters*, **36** (2011) 2426. doi:10.1364/OL.36.002426.

[15] Wenz, J., Schleede, S., *et al.* "Quantitative X-ray phase-contrast microtomography from a compact laser-driven betatron source." *Nature Communications*, **6** (2015) 7568. doi:10.1038/ncomms8568.

[16] Hidding, B., Karger, O., *et al.* "Laser-plasma-based space radiation reproduction in the laboratory." *Scientific Reports*, **7** (2017) 42354. doi:10.1038/srep42354.

[17] Yoon, J. W., Kim, Y. G., *et al.* "Realization of laser intensity over 10^{23} W/cm^2." *Optica*, **8** (2021) 630. doi:10.1364/OPTICA.420520.

[18] Blackburn, T. G. "Radiation reaction in electron–beam interactions with high-intensity lasers." *Reviews of Modern Plasma Physics*, **4** (2020) 5. doi:10.1007/s41614-020-0042-0.

[19] Di Piazza, A., Müller, C., *et al.* "Extremely high-intensity laser interactions with fundamental quantum systems." *Reviews of Modern Physics*, **84** (2012) 1177. doi:10.1103/RevModPhys.84.1177.

[20] Marklund, M. and Shukla, P. K. "Nonlinear collective effects in photon-photon and photon-plasma interactions." *Reviews of Modern Physics*, **78** (2006) 591. doi:10.1103/RevModPhys.78.591.

[21] Malkin, V. M., Shvets, G., *et al.* "Fast compression of laser beams to highly overcritical powers." *Physical Review Letters*, **82** (1999) 4448. doi:10.1103/PhysRevLett.82.4448.

[22] Vieux, G., Cipiccia, S., *et al.* "An ultra-high gain and efficient amplifier based on Raman amplification in plasma." *Scientific Reports*, **7** (2017) 2399. doi:10.1038/s41598-017-01783-4.

[23] Ren, J., Cheng, W., *et al.* "A new method for generating ultraintense and ultrashort laser pulses." *Nature Physics*, **3** (2007) 732. doi:10.1038/nphys717.

[24] Ersfeld, B. and Jaroszynski, D. A. "Superradiant linear Raman amplification in plasma using a chirped pump pulse." *Physical Review Letters*, **95** (2005) 165002. doi:10.1103/PhysRevLett.95.165002.

[25] Milroy, R. D., Capjack, C. E., *et al.* "Plasma laser pulse amplifier using induced Raman or Brillouin processes." *The Physics of Fluids*, **22** (1979) 1922. doi:10.1063/1.862481.

[26] Marquès, J.-R., Lancia, L., *et al.* "Joule-level high-efficiency energy transfer to subpicosecond laser pulses by a plasma-based amplifier." *Physical Review X*, **9** (2019) 021008. doi:10.1103/PhysRevX.9.021008.

[27] Kapteyn, H. C., Murnane, M. M., *et al.* "Prepulse energy suppression for high-energy ultrashort pulses using self-induced plasma shuttering." *Optics Letters*, **16** (1991) 490. doi:10.1364/OL.16.000490.

[28] Thaury, C., Quéré, F., *et al.* "Plasma mirrors for ultrahigh-intensity optics." *Nature Physics*, **3** (2007) 424. doi:10.1038/nphys595.

[29] Leblanc, A., Denoeud, A., *et al.* "Plasma holograms for ultrahigh-intensity optics." *Nature Physics*, **13** (2017) 440. doi:10.1038/nphys4007.

[30] Chopineau, L., Denoeud, A., *et al.* "Spatio-temporal characterization of attosecond pulses from plasma mirrors." *Nature Physics*, **17** (2021) 968. doi:10.1038/s41567-021-01253-9.

[31] Lehmann, G. and Spatschek, K. H. "Plasma-based polarizer and waveplate at large laser intensity." *Physical Review E*, **97** (2018) 063201. doi:10.1103/PhysRevE.97.063201.

[32] Lehmann, G. and Spatschek, K. H. "Transient plasma photonic crystals for high-power lasers." *Physical Review Letters*, **116** (2016) 225002. doi:10.1103/PhysRevLett.116.225002.

[33] Lehmann, G. and Spatschek, K. H. "Laser-driven plasma photonic crystals for high-power lasers." *Physics of Plasmas*, **24** (2017) 056701. doi:10.1063/1.4977463.

[34] Edwards, M. R., Munirov, V. R., *et al.* "Holographic Plasma Lenses." *Physical Review Letters*, **128** (2022) 065003. doi:10.1103/PhysRevLett.128.065003.

[35] Edwards, M. R. and Michel, P. "Plasma Transmission Gratings for Compression of High-Intensity Laser Pulses." *Physical Review Applied*, **18** (2022) 024026. doi:10.1103/PhysRevApplied.18.024026.

[36] Jackson, J. D. *Classical Electrodynamics*. Wiley, New York, 3rd ed. (2012). ISBN 978-0-471-30932-1.

[37] Milonni, P. W. and Eberly, J. H. *Laser Physics*. John Wiley & Sons (2010). ISBN 978-0-470-38771-9.

[38] Self, S. A. "Focusing of spherical Gaussian beams." *Applied Optics*, **22** (1983) 658. doi:10.1364/AO.22.000658.

[39] Treacy, E. “Optical pulse compression with diffraction gratings.” *IEEE Journal of Quantum Electronics*, **5** (1969) 454. doi:10.1109/JQE.1969.1076303.

[40] Martinez, O. E., Gordon, J. P., *et al.* “Negative group-velocity dispersion using refraction.” *JOSA A*, **1** (1984) 1003. doi:10.1364/JOSAA.1.001003.

[41] Moulton, P. F. “Spectroscopic and laser characteristics of Ti:Al_2O_3.” *JOSA B*, **3** (1986) 125. doi:10.1364/JOSAB.3.000125.

[42] Spence, D. E., Kean, P. N., *et al.* “60-fsec pulse generation from a self-mode-locked Ti:sapphire laser.” *Optics Letters*, **16** (1991) 42. doi:10.1364/OL.16.000042.

[43] Negus, D. K., Spinelli, L., *et al.* “Sub-100 femtosecond pulse generation by kerr lens mode-locking in Ti: Al2O3.” In *Advanced Solid State Lasers (1991), Paper SPL7*, SPL7. Optical Society of America (1991). doi:10.1364/ASSL.1991.SPL7.

[44] Rigrod, W. W. “Gain saturation and output power of optical masers.” *Journal of Applied Physics*, **34** (1963) 2602. doi:10.1063/1.1729777.

[45] Hotz, D. F. “Gain narrowing in a laser amplifier.” *Applied Optics*, **4** (1965). doi:10.1364/AO.4.000527.

[46] Huang, C.-P., Kapteyn, H. C., *et al.* “Generation of transform-limited 32-fs pulses from a self-mode-locked Ti:sapphire laser.” *Optics Letters*, **17** (1992) 139. doi:10.1364/OL.17.000139.

[47] Huang, C.-P., Asaki, M. T., *et al.* “17-fs pulses from a self-mode-locked Ti:sapphire laser.” *Optics Letters*, **17** (1992) 1289. doi:10.1364/OL.17.001289.

[48] Asaki, M. T., Huang, C.-P., *et al.* “Generation of 11-fs pulses from a self-mode-locked Ti:sapphire laser.” *Optics Letters*, **18** (1993) 977. doi:10.1364/OL.18.000977.

[49] Kapteyn, H. C. and Murnane, M. M. “Femtosecond Lasers: The Next Generation.” *Optics and Photonics News*, **5** (1994) 20. doi:10.1364/OPN.5.3.000020.

[50] Lemoff, B. E. and Barty, C. P. J. "Quintic-phase-limited, spatially uniform expansion and recompression of ultrashort optical pulses." *Optics Letters*, **18** (1993) 1651. doi:10.1364/OL.18.001651.

[51] Tournois, P. "Acousto-optic programmable dispersive filter for adaptive compensation of group delay time dispersion in laser systems." *Optics Communications*, **140** (1997) 245. doi:10.1016/S0030-4018(97)00153-3.

[52] Verluise, F., Laude, V., *et al.* "Arbitrary dispersion control of ultrashort optical pulses with acoustic waves." *JOSA B*, **17** (2000) 138. doi:10.1364/JOSAB.17.000138.

[53] Korn, G., Bulanov, S. V., *et al.* "Extreme Light Infrastructure (ELI): Physics and Lasers at the ultra-intense frontier." In *Conference on Lasers and Electro-Optics 2010 (2010), Paper JThG2*, JThG2. Optical Society of America (2010). doi:10.1364/CLEO.2010.JThG2.

[54] Rus, B., Bakule, P., *et al.* "ELI-beamlines: Progress in development of next generation short-pulse laser systems." In *Research Using Extreme Light: Entering New Frontiers with Petawatt-Class Lasers III*, vol. 10241, 102410J. International Society for Optics and Photonics (2017). doi:10.1117/12.2269818.

[55] Gales, S., Tanaka, K. A., *et al.* "The extreme light infrastructure—nuclear physics (ELI-NP) facility: New horizons in physics with 10 PW ultra-intense lasers and 20 MeV brilliant gamma beams." *Reports on Progress in Physics*, **81** (2018) 094301. doi:10.1088/1361-6633/aacfe8.

[56] Kühn, S., Dumergue, M., *et al.* "The ELI-ALPS facility: The next generation of attosecond sources." *Journal of Physics B: Atomic, Molecular and Optical Physics*, **50** (2017) 132002. doi:10.1088/1361-6455/aa6ee8.

[57] Garrec, B. L. "Design update and recent results of the Apollon 10 PW facility." In *Conference on Lasers and Electro-Optics (2017), Paper SF1K.3*, SF1K.3. Optical Society of America (2017). doi:10.1364/CLEO_SI.2017.SF1K.3.

[58] Liang, X., Leng, Y., *et al.* "Recent Progress on the Shanghai Superintense Ultrafast Laser Facility (SULF) at SIOM." In *OSA High-brightness Sources and Light-driven Interactions Congress 2020 (EUVXRAY, HILAS, MICS) (2020), Paper HTh2B.2*, HTh2B.2. Optical Society of America (2020). doi:10.1364/HILAS.2020.HTh2B.2.

[59] Leemans, W. P., Daniels, J., *et al.* "BELLA laser and operations." In *Proceedings of PAC2013*. California (2013). ISBN 978-3-95450-138-0.

[60] Roso, L. "High repetition rate petawatt lasers." In *EPJ Web of Conferences* (2018). doi:10.1051/epjconf/201816701001.

[61] Gaul, E. W., Martinez, M., *et al.* "Demonstration of a 1.1 petawatt laser based on a hybrid optical parametric chirped pulse amplification/mixed Nd:glass amplifier." *Applied Optics*, **49** (2010) 1676. doi:10.1364/AO.49.001676.

[62] Hooker, C. J., Blake, S., *et al.* "Commissioning the Astra Gemini Petawatt Ti:Sapphire Laser System." In *Conference on Lasers and Electro-Optics/Quantum Electronics and Laser Science Conference and Photonic Applications Systems Technologies (2008), Paper JThB2*, JThB2. Optica Publishing Group (2008).

[63] Wiggins, S. M., Boyd, M., *et al.* "Application programmes at the Scottish Centre for the Application of Plasma-based Accelerators (SCAPA)." In *Relativistic Plasma Waves and Particle Beams as Coherent and Incoherent Radiation Sources III*, vol. 11036, 110360T. International Society for Optics and Photonics (2019). doi:10.1117/12.2520717.

[64] Holt, G. K., Battaglia, G., *et al.* "Progress towards laser wakefield acceleration and applications at the Scottish Centre for the Application of Plasma-based Accelerators (SCAPA)." *Journal of Physics: Conference Series*, **1596** (2020) 012037. doi:10.1088/1742-6596/1596/1/012037.

[65] Danson, C. N., Haefner, C., *et al.* "Petawatt and exawatt class lasers worldwide." *High Power Laser Science and Engineering*, **7** (2019/ed). doi:10.1017/hpl.2019.36.

[66] Einstein, A. "Concerning an heuristic point of view toward the emission and transformation of light." *Annalen der Physik*, **17** (1905) 132.

[67] Lambropoulos, P. "Topics on Multiphoton Processes in Atoms." In D. R. Bates and B. Bederson, eds., *Advances in Atomic and Molecular Physics*, vol. 12, 87–164. Academic Press (1976). doi:10.1016/S0065-2199(08)60043-3.

[68] Hall, J. L., Robinson, E. J., *et al.* "Laser double-quantum photodetachment of I^-." *Physical Review Letters*, **14** (1965) 1013. doi:10.1103/PhysRevLett.14.1013.

[69] Voronov, G. S. and Delone, N. B. "Many-photon ionization of the xenon atom by ruby laser radiation." *Soviet Physics JETP*, **23** (1966) 54.

[70] Agostini, P., Barjot, G., *et al.* "Multiphoton ionization of hydrogen and rare gases." *IEEE Journal of Quantum Electronics*, **4** (1968) 667. doi:10.1109/JQE.1968.1074955.

[71] Agostini, P., Fabre, F., *et al.* "Free-free transitions following six-photon ionization of xenon atoms." *Physical Review Letters*, **42** (1979) 1127. doi:10.1103/PhysRevLett.42.1127.

[72] Gontier, Y., Poirier, M., *et al.* "Multiphoton absorptions above the ionisation threshold." *Journal of Physics B: Atomic and Molecular Physics*, **13** (1980) 1381. doi:10.1088/0022-3700/13/7/013.

[73] Milošević, D. B., Paulus, G. G., *et al.* "Above-threshold ionization by few-cycle pulses." *Journal of Physics B: Atomic, Molecular and Optical Physics*, **39** (2006) R203. doi:10.1088/0953-4075/39/14/R01.

[74] Gontier, Y. and Trahin, M. "Energetic electron generation by multiphoton absorption." *Journal of Physics B: Atomic and Molecular Physics*, **13** (1980) 4383. doi:10.1088/0022-3700/13/22/012.

[75] Kruit, P., Kimman, J., *et al.* "Electron spectra from multiphoton ionization of xenon at 1064, 532, and 355 nm." *Physical Review A*, **28** (1983) 248. doi:10.1103/PhysRevA.28.248.

[76] Lompré, L. A., L'Huillier, A., *et al.* "Laser-intensity effects in the energy distributions of electrons produced in multiphoton ionization of rare gases." *JOSA B*, **2** (1985) 1906. doi:10.1364/JOSAB.2.001906.

[77] Xiong, W., Yergeau, F., *et al.* "Multiphoton ionisation of rare gases by a CO_2 laser: Electron spectroscopy." *Journal of Physics B: Atomic, Molecular and Optical Physics*, **21** (1988) L159. doi:10.1088/0953-4075/21/7/004.

[78] Bucksbaum, P. H., Freeman, R. R., *et al.* "Role of the ponderomotive potential in above-threshold ionization." *JOSA B*, **4** (1987) 760. doi:10.1364/JOSAB.4.000760.

[79] Keldysh, L. V. "Ionization in the field of a strong electromagnetic wave." *Soviet Physics JETP*, **20** (1964) 1307.

[80] Gibbon, P. *Short Pulse Laser Interactions with Matter: An Introduction.* Imperial College Press, London (2005). ISBN 978-1-86094-135-1.

[81] Bethe, H. A. and Salpeter, E. E. *Quantum Mechanics of One- and Two-Electron Atoms.* Springer-Verlag (1957).

[82] Ammosov, M. V., Delone, N. B., *et al.* "Tunnel ionization of complex atoms and of atomic ions in an electromagnetic field." *Soviet Physics JETP*, **64** (1986) 1191.

[83] Auguste, T., Monot, P., *et al.* "Multiply charged ions produced in noble gases by a 1 ps laser pulse at lambda =1053 nm." *Journal of Physics B: Atomic, Molecular and Optical Physics*, **25** (1992) 4181. doi:10.1088/0953-4075/25/20/015.

[84] Jackson, J. D. *Classical Electrodynamics.* John Wiley & Sons, 3rd ed. (1999). ISBN 0-471-30932-X.

[85] Eberly, J. H. and Sleeper, A. "Trajectory and mass shift of a classical electron in a radiation pulse." *Physical Review*, **176** (1968) 1570. doi:10.1103/PhysRev.176.1570.

[86] Sarachik, E. S. and Schappert, G. T. "Classical theory of the scattering of intense laser radiation by free electrons." *Physical Review D*, **1** (1970) 2738. doi:10.1103/PhysRevD.1.2738.

[87] Gunn, J. E. and Ostriker, J. P. "On the motion of radiation of charged particles in strong electromagnetic waves I. Motion in plane and spherical waves." *Astrophysical Journal*, **165** (1971) 523. doi:10.1086/150919.

[88] Landau, L. D. and Lifshitz, E. M. *The Classical Theory of Fields*, vol. 2. Pergamon Press, third revised english edition ed. (1971).

[89] Krüger, J. and Bovyn, M. "Relativistic motion of a charged particle in a plane electromagnetic wave with arbitrary amplitude." *Journal of Physics A: Mathematical and General*, **9** (1976) 1841. doi:10.1088/0305-4470/9/11/008.

[90] Meyer-ter-Vehn, J., Pukhov, A., *et al.* "Relativistic laser plasma interactions." In *Atoms, Solids and Plasma in Super-Intense Laser Fields*, 167. Springer (2001). ISBN 978-1-4615-1351-3.

[91] Landau, L. D. and Lifshitz, E. M. *Mechanics*, vol. 1 of *Course of Theoretical Physics*. Elsevier Butterworth-Heinemann, Oxford, 3rd ed. (1976). ISBN 978-0-7506-2896-9.

[92] Boot, H. A. H., Self, S. A., *et al.* "Containment of a fully-ionized plasma by radio-frequency fields." *Journal of Electronics and Control*, **4** (1958) 434. doi:10.1080/00207215808953862.

[93] Gaponov, A. V. and Miller, M. A. "Potential wells for charged particles in a high-frequency electromagnetic field." *Soviet Physics JETP*, **7** (1958) 168.

[94] Kibble, T. W. B. "Mutual refraction of electrons and photons." *Physical Review*, **150** (1966) 1060. doi:10.1103/PhysRev.150.1060.

[95] Hopf, F. A., Meystre, P., *et al.* "Classical theory of a free-electron laser." *Physical Review Letters*, **37** (1976) 1215. doi:10.1103/PhysRevLett.37.1215.

[96] Omohundro, S. M. *Geometric Perturbation Theory in Physics.* World Scientific, Singapore (1986). ISBN 9971-5-0136-8.

[97] Bauer, D., Mulser, P., *et al.* "Relativistic ponderomotive force, uphill acceleration, and transition to chaos." *Physical Review Letters*, **75** (1995) 4622. doi:10.1103/PhysRevLett.75.4622.

[98] Startsev, E. A. and McKinstrie, C. J. "Multiple scale derivation of the relativistic ponderomotive force." *Physical Review E*, **55** (1997) 7527. doi:10.1103/PhysRevE.55.7527.

[99] Chen, F. F. *Introduction to Plasma Physics and Controlled Fusion.* Springer, Switzerland, 3rd ed. (2018). ISBN 978-3-319-22308-7.

[100] Boyd, T. J. M. and Sanderson, J. J. *The Physics of Plasmas.* Cambridge University Press, Cambridge (2003). ISBN 978-0-521-45290-8.

[101] Tonks, L. and Langmuir, I. "Oscillations in ionized gases." *Physical Review*, **33** (1929) 195. doi:10.1103/PhysRev.33.195.

[102] Andreev, A. A., Mak, A. A., *et al.* *An Introduction to Hot Laser Plasma Physics.* Nova Science Publishers (2000). ISBN 978-1-56072-803-0.

[103] Akhiezer, A. I. and Polovin, R. V. "Theory of wave motion of an electron plasma." *Soviet Physics JETP*, **3** (1956) 696.

[104] Decoster, A. "Nonlinear travelling waves in a homogeneous cold collisionless plasma." *Physics Reports*, **47** (1978) 285.

[105] Noble, R. J. "Plasma-wave generation in the beat-wave accelerator." *Physical Review A*, **32** (1985) 460. doi:10.1103/PhysRevA.32.460.

[106] Sprangle, P., Esarey, E., *et al.* "Nonlinear interaction of intense laser pulses in plasmas." *Physical Review A*, **41** (1990) 4463. doi:10.1103/PhysRevA.41.4463.

[107] Sprangle, P., Esarey, E., *et al.* "Nonlinear theory of intense laser-plasma interactions." *Physical Review Letters*, **64** (1990) 2011. doi:10.1103/PhysRevLett.64.2011.

[108] Berezhiani, V. I. and Murusidze, I. G. "Interaction of highly relativistic short laser pulses with plasmas and nonlinear wake-field generation." *Physica Scripta*, **45** (1992) 87. doi:10.1088/0031-8949/45/2/007.

[109] Esarey, E., Ting, A., *et al.* "Nonlinear analysis of relativistic harmonic generation by intense lasers in plasmas." *IEEE Transactions on Plasma Science*, **21** (1993) 95. doi:10.1109/27.221107.

[110] Teychenné, D., Bonnaud, G., *et al.* "Wave-breaking limit to the wake-field effect in an underdense plasma." *Physical Review E*, **48** (1993) R3248. doi:10.1103/PhysRevE.48.R3248.

[111] Dawson, J. M. "Nonlinear electron oscillations in a cold plasma." *Physical Review*, **113** (1959) 383. doi:10.1103/PhysRev.113.383.

[112] Tajima, T. and Dawson, J. M. "Laser electron accelerator." *Physical Review Letters*, **43** (1979) 267. doi:10.1103/PhysRevLett.43.267.

[113] Kitagawa, Y., Matsumoto, T., *et al.* "Beat-wave excitation of plasma wave and observation of accelerated electrons." *Physical Review Letters*, **68** (1992) 48. doi:10.1103/PhysRevLett.68.48.

[114] Clayton, C. E., Marsh, K. A., *et al.* "Ultrahigh-gradient acceleration of injected electrons by laser-excited relativistic electron plasma waves." *Physical Review Letters*, **70** (1993) 37. doi:10.1103/PhysRevLett.70.37.

[115] Ebrahim, N. A. "Optical mixing of laser light in a plasma and electron acceleration by relativistic electron plasma waves." *Journal of Applied Physics*, **76** (1994) 7645. doi:10.1063/1.357937.

[116] Everett, M., Lal, A., *et al.* "Trapped electron acceleration by a laser-driven relativistic plasma wave." *Nature*, **368** (1994) 527. doi:10.1038/368527a0.

[117] Modena, A., Najmudin, Z., *et al.* "Electron acceleration from the breaking of relativistic plasma waves." *Nature*, **377** (1995) 606. doi:10.1038/377606a0.

[118] Nakajima, K., Fisher, D., *et al.* "Observation of ultrahigh gradient electron acceleration by a self-modulated intense short laser pulse." *Physical Review Letters*, **74** (1995) 4428. doi:10.1103/PhysRevLett.74.4428.

[119] Ting, A., Moore, C. I., *et al.* "Plasma wakefield generation and electron acceleration in a self-modulated laser wakefield accelerator experiment." *Physics of Plasmas*, **4** (1997) 1889. doi:10.1063/1.872332.

[120] Malka, V., Fritzler, S., *et al.* "Electron acceleration by a wake field forced by an intense ultrashort laser pulse." *Science*, **298** (2002) 1596. doi:10.1126/science.1076782.

[121] Geddes, C. G. R., Toth, C., *et al.* "High-quality electron beams from a laser wakefield accelerator using plasma-channel guiding." *Nature*, **431** (2004) 538. doi:10.1038/nature02900.

[122] Mangles, S. P. D., Murphy, C. D., *et al.* "Monoenergetic beams of relativistic electrons from intense laser–plasma interactions." *Nature*, **431** (2004) 535. doi:10.1038/nature02939.

[123] Faure, J., Glinec, Y., *et al.* "A laser–plasma accelerator producing monoenergetic electron beams." *Nature*, **431** (2004) 541. doi:10.1038/nature02963.

[124] Wang, X., Zgadzaj, R., *et al.* "Quasi-monoenergetic laser-plasma acceleration of electrons to 2 GeV." *Nature Communications*, **4** (2013) 1988. doi:10.1038/ncomms2988.

[125] Gonsalves, A. J., Nakamura, K., *et al.* "Petawatt laser guiding and electron beam acceleration to 8 GeV in a laser-heated capillary discharge waveguide." *Physical Review Letters*, **122** (2019) 084801. doi:10.1103/PhysRevLett.122.084801.

[126] Salehi, F., Le, M., *et al.* “Laser-accelerated, low-divergence 15-MeV quasimonoenergetic electron bunches at 1 kHz.” *Physical Review X*, **11** (2021) 021055. doi:10.1103/PhysRevX.11.021055.

[127] Maier, A. R., Delbos, N. M., *et al.* “Decoding sources of energy variability in a laser-plasma accelerator.” *Physical Review X*, **10** (2020) 031039. doi:10.1103/PhysRevX.10.031039.

[128] Leemans, W. and Esarey, E. “Laser-driven plasma-wave electron accelerators.” *Physics Today*, **62** (2009) 44. doi:10.1063/1.3099645.

[129] Schroeder, C. B., Esarey, E., *et al.* “Physics considerations for laser-plasma linear colliders.” *Physical Review Special Topics - Accelerators and Beams*, **13** (2010) 101301. doi:10.1103/PhysRevSTAB.13.101301.

[130] Shiltsev, V. and Zimmermann, F. “Modern and future colliders.” *Reviews of Modern Physics*, **93** (2021) 015006. doi:10.1103/RevModPhys.93.015006.

[131] Couprie, M. E., Labat, M., *et al.* “An application of laser–plasma acceleration: Towards a free-electron laser amplification.” *Plasma Physics and Controlled Fusion*, **58** (2016) 034020. doi:10.1088/0741-3335/58/3/034020.

[132] André, T., Andriyash, I. A., *et al.* “Control of laser plasma accelerated electrons for light sources.” *Nature Communications*, **9** (2018) 1334. doi:10.1038/s41467-018-03776-x.

[133] Cole, J. M., Behm, K. T., *et al.* “Experimental evidence of radiation reaction in the collision of a high-intensity laser pulse with a laser-wakefield accelerated electron beam.” *Physical Review X*, **8** (2018) 011020. doi:10.1103/PhysRevX.8.011020.

[134] Kostyukov, I., Kiselev, S., *et al.* “X-ray generation in an ion channel.” *Physics of Plasmas*, **10** (2003) 4818. doi:10.1063/1.1624605.

[135] Kiselev, S., Pukhov, A., *et al.* “X-ray generation in strongly nonlinear plasma waves.” *Physical Review Letters*, **93** (2004) 135004. doi:10.1103/PhysRevLett.93.135004.

[136] Rousse, A., Phuoc, K. T., *et al.* “Production of a keV X-Ray beam from synchrotron radiation in relativistic laser-plasma interaction.” *Physical Review Letters*, **93** (2004) 135005. doi:10.1103/PhysRevLett.93.135005.

[137] Cipiccia, S., Islam, M. R., *et al.* “Gamma-rays from harmonically resonant betatron oscillations in a plasma wake.” *Nature Physics*, **7** (2011) 867. doi:10.1038/nphys2090.

[138] Kneip, S., McGuffey, C., *et al.* “X-ray phase contrast imaging of biological specimens with femtosecond pulses of betatron radiation from a compact laser plasma wakefield accelerator.” *Applied Physics Letters*, **99** (2011) 093701. doi:10.1063/1.3627216.

[139] Svendsen, K., González, I. G., *et al.* “Optimization of soft X-ray phase-contrast tomography using a laser wakefield accelerator.” *Optics Express*, **26** (2018) 33930. doi:10.1364/OE.26.033930.

[140] Guo, B., Zhang, X., *et al.* “High-resolution phase-contrast imaging of biological specimens using a stable betatron X-ray source in the multiple-exposure mode.” *Scientific Reports*, **9** (2019) 7796. doi:10.1038/s41598-019-42834-2.

[141] Cole, J. M., Symes, D. R., *et al.* “High-resolution µCT of a mouse embryo using a compact laser-driven X-ray betatron source.” *Proceedings of the National Academy of Sciences*, **115** (2018) 6335. doi:10.1073/pnas.1802314115.

[142] Mahieu, B., Jourdain, N., *et al.* “Probing warm dense matter using femtosecond X-ray absorption spectroscopy with a laser-produced betatron source.” *Nature Communications*, **9** (2018) 3276. doi:10.1038/s41467-018-05791-4.

[143] Kettle, B., Gerstmayr, E., *et al.* "Single-shot multi-keV X-ray absorption spectroscopy using an ultrashort laser-wakefield accelerator source." *Physical Review Letters*, **123** (2019) 254801. doi:10.1103/PhysRevLett.123.254801.

[144] Glinec, Y., Faure, J., *et al.* "High-resolution γ-ray radiography produced by a laser-plasma driven electron source." *Physical Review Letters*, **94** (2005) 025003. doi:10.1103/PhysRevLett.94.025003.

[145] Ben-Ismaïl, A., Lundh, O., *et al.* "Compact and high-quality gamma-ray source applied to 10 μm-range resolution radiography." *Applied Physics Letters*, **98** (2011) 264101. doi:10.1063/1.3604013.

[146] Pukhov, A. and Meyer-ter-Vehn, J. "Laser wake field acceleration: The highly non-linear broken-wave regime." *Applied Physics B*, **74** (2002) 355. doi:10.1007/s003400200795.

[147] Kostyukov, I., Pukhov, A., *et al.* "Phenomenological theory of laser-plasma interaction in "bubble" regime." *Physics of Plasmas*, **11** (2004) 5256. doi:10.1063/1.1799371.

[148] Joshi, C. "Laser-driven plasma accelerators operating in the self-guided, blowout regime." *IEEE Transactions on Plasma Science*, **45** (2017) 3134. doi:10.1109/TPS.2017.2769455.

[149] Lehe, R., Kirchen, M., *et al.* "A spectral, quasi-cylindrical and dispersion-free Particle-In-Cell algorithm." *Computer Physics Communications*, **203** (2016) 66. doi:10.1016/j.cpc.2016.02.007.

[150] Kostyukov, I., Nerush, E., *et al.* "A multidimensional theory for electron trapping by a plasma wake generated in the bubble regime." *New Journal of Physics*, **12** (2010) 045009. doi:10.1088/1367-2630/12/4/045009.

[151] Yi, S. A., Khudik, V., *et al.* "Hamiltonian analysis of electron self-injection and acceleration into an evolving plasma bubble." *Plasma Physics and Controlled Fusion*, **53** (2010) 014012. doi:10.1088/0741-3335/53/1/014012.

[152] Kalmykov, S. Y., Beck, A., *et al.* "Electron self-injection into an evolving plasma bubble: Quasi-monoenergetic laser-plasma acceleration in the blowout regime." *Physics of Plasmas*, **18** (2011) 056704. doi:10.1063/1.3566062.

[153] Islam, M. R., Brunetti, E., *et al.* "Near-threshold electron injection in the laser–plasma wakefield accelerator leading to femtosecond bunches." *New Journal of Physics*, **17** (2015) 093033. doi:10.1088/1367-2630/17/9/093033.

[154] Kaganovich, D., Gordon, D. F., *et al.* "Observation of large-angle quasimonoenergetic electrons from a laser wakefield." *Physical Review Letters*, **100** (2008) 215002. doi:10.1103/PhysRevLett.100.215002.

[155] Zhang, L., Chen, L.-M., *et al.* "Electron acceleration via high contrast laser interacting with submicron clusters." *Applied Physics Letters*, **100** (2012) 014104. doi:10.1063/1.3673911.

[156] Yang, X., Brunetti, E., *et al.* "Three electron beams from a laser-plasma wakefield accelerator and the energy apportioning question." *Scientific Reports*, **7** (2017) 43910. doi:10.1038/srep43910.

[157] Behm, K., Hussein, A., *et al.* "Measurements of electron beam ring structures from laser wakefield accelerators." *Plasma Physics and Controlled Fusion*, **61** (2019) 065012. doi:10.1088/1361-6587/ab0622.

[158] Hooker, S. M. "Developments in laser-driven plasma accelerators." *Nature Photonics*, **7** (2013) 775. doi:10.1038/nphoton.2013.234.

[159] Lu, W., Huang, C., *et al.* "Nonlinear theory for relativistic plasma wakefields in the blowout regime." *Physical Review Letters*, **96** (2006) 165002. doi:10.1103/PhysRevLett.96.165002.

[160] Lu, W., Huang, C., *et al.* "A nonlinear theory for multidimensional relativistic plasma wave wakefields." *Physics of Plasmas*, **13** (2006) 056709. doi:10.1063/1.2203364.

[161] Kim, H. T., Pae, K. H., *et al.* "Enhancement of electron energy to the multi-GeV regime by a dual-stage laser-wakefield accelerator pumped by petawatt laser pulses." *Physical Review Letters*, **111** (2013) 165002. doi:10.1103/PhysRevLett.111.165002.

[162] Joshi, C., Corde, S., *et al.* "Perspectives on the generation of electron beams from plasma-based accelerators and their near and long term applications." *Physics of Plasmas*, **27** (2020) 070602. doi:10.1063/5.0004039.

[163] van Tilborg, J., Steinke, S., *et al.* "Active plasma lensing for relativistic laser-plasma-accelerated electron beams." *Physical Review Letters*, **115** (2015) 184802. doi:10.1103/PhysRevLett.115.184802.

[164] Sokollik, T., Shiraishi, S., *et al.* "Tape-drive based plasma mirror." *AIP Conference Proceedings*, **1299** (2010) 233. doi:10.1063/1.3520320.

[165] Steinke, S., van Tilborg, J., *et al.* "Multistage coupling of independent laser-plasma accelerators." *Nature*, **530** (2016) 190. doi:10.1038/nature16525.

[166] Pak, A., Marsh, K. A., *et al.* "Injection and trapping of tunnel-ionized electrons into laser-produced wakes." *Physical Review Letters*, **104** (2010) 025003. doi:10.1103/PhysRevLett.104.025003.

[167] Liu, J. S., Xia, C. Q., *et al.* "All-optical cascaded laser wakefield accelerator using ionization-induced injection." *Physical Review Letters*, **107** (2011) 035001. doi:10.1103/PhysRevLett.107.035001.

[168] Chen, M., Esarey, E., *et al.* "Theory of ionization-induced trapping in laser-plasma accelerators." *Physics of Plasmas*, **19** (2012) 033101. doi:10.1063/1.3689922.

[169] Li, Y. F., Li, D. Z., *et al.* "Generation of 20 kA electron beam from a laser wakefield accelerator." *Physics of Plasmas*, **24** (2017) 023108. doi:10.1063/1.4975613.

[170] Couperus, J. P., Pausch, R., *et al.* "Demonstration of a beam loaded nanocoulomb-class laser wakefield accelerator." *Nature Communications*, **8** (2017) 487. doi:10.1038/s41467-017-00592-7.

[171] Lécz, Z., Andreev, A., *et al.* "Generation of high-quality GeV-class electron beams utilizing attosecond ionization injection." *New Journal of Physics*, **23** (2021) 043016. doi:10.1088/1367-2630/abf076.

[172] Kalmykov, S., Yi, S. A., *et al.* "Electron self-injection and trapping into an evolving plasma bubble." *Physical Review Letters*, **103** (2009) 135004. doi: 10.1103/PhysRevLett.103.135004.

[173] Kostyukov, I., Nerush, E., *et al.* "Electron self-injection in multidimensional relativistic-plasma wake fields." *Physical Review Letters*, **103** (2009) 175003. doi:10.1103/PhysRevLett.103.175003.

[174] Thomas, A. G. R. "Scalings for radiation from plasma bubbles." *Physics of Plasmas*, **17** (2010) 056708. doi:10.1063/1.3368678.

[175] Umstadter, D., Kim, J. K., *et al.* "Laser injection of ultrashort electron pulses into wakefield plasma waves." *Physical Review Letters*, **76** (1996) 2073. doi: 10.1103/PhysRevLett.76.2073.

[176] Wang, W.-M., Sheng, Z.-M., *et al.* "Controlled electron injection into laser wakefields with a perpendicular injection laser pulse." *Applied Physics Letters*, **93** (2008) 201502. doi:10.1063/1.3020301.

[177] Horný, V., Petržílka, V., *et al.* "Short electron bunches generated by perpendicularly crossing laser pulses." *Physics of Plasmas*, **24** (2017) 103125. doi: 10.1063/1.5007889.

[178] Esarey, E., Hubbard, R. F., *et al.* "Electron injection into plasma wakefields by colliding laser pulses." *Physical Review Letters*, **79** (1997) 2682. doi:10.1103/PhysRevLett.79.2682.

[179] Fubiani, G., Esarey, E., *et al.* "Beat wave injection of electrons into plasma waves using two interfering laser pulses." *Physical Review E*, **70** (2004) 016402. doi:10.1103/PhysRevE.70.016402.

[180] Kotaki, H., Masuda, S., *et al.* "Head-on injection of a high quality electron beam by the interaction of two laser pulses." *Physics of Plasmas*, **11** (2004) 3296. doi:10.1063/1.1751171.

[181] Davoine, X., Lefebvre, E., *et al.* "Cold optical injection producing monoenergetic, multi-GeV electron bunches." *Physical Review Letters*, **102** (2009) 065001. doi: 10.1103/PhysRevLett.102.065001.

[182] Lehe, R., Lifschitz, A. F., *et al.* "Optical transverse injection in laser-plasma acceleration." *Physical Review Letters*, **111** (2013) 085005. doi:10.1103/PhysRevLett.111.085005.

[183] Bulanov, S., Naumova, N., *et al.* "Particle injection into the wave acceleration phase due to nonlinear wake wave breaking." *Physical Review E*, **58** (1998) R5257. doi:10.1103/PhysRevE.58.R5257.

[184] Suk, H., Barov, N., *et al.* "Plasma electron trapping and acceleration in a plasma wake field using a density transition." *Physical Review Letters*, **86** (2001) 1011. doi:10.1103/PhysRevLett.86.1011.

[185] Ohkubo, T., Zhidkov, A., *et al.* "Effects of density gradient on short-bunch injection by wave breaking in the laser wake field acceleration." *Physics of Plasmas*, **13** (2006) 033110. doi:10.1063/1.2181434.

[186] Geddes, C. G. R., Nakamura, K., *et al.* "Plasma-density-gradient injection of low absolute-momentum-spread electron bunches." *Physical Review Letters*, **100** (2008) 215004. doi:10.1103/PhysRevLett.100.215004.

[187] Brantov, A. V., Esirkepov, T. Z., *et al.* "Controlled electron injection into the wake wave using plasma density inhomogeneity." *Physics of Plasmas*, **15** (2008) 073111. doi:10.1063/1.2956989.

[188] Gonsalves, A. J., Nakamura, K., *et al.* "Tunable laser plasma accelerator based on longitudinal density tailoring." *Nature Physics*, **7** (2011) 862. doi:10.1038/nphys2071.

[189] Tooley, M. P., Ersfeld, B., *et al.* "Towards attosecond high-energy electron bunches: Controlling self-injection in laser-wakefield accelerators through plasma-density modulation." *Physical Review Letters*, **119** (2017) 044801. doi:10.1103/PhysRevLett.119.044801.

[190] Kuschel, S., Schwab, M. B., *et al.* "Controlling the self-injection threshold in laser wakefield accelerators." *Physical Review Letters*, **121** (2018) 154801. doi:10.1103/PhysRevLett.121.154801.

[191] Durfee, C. G. and Milchberg, H. M. "Light pipe for high intensity laser pulses." *Physical Review Letters*, **71** (1993) 2409. doi:10.1103/PhysRevLett.71.2409.

[192] Hosokai, T., Kando, M., *et al.* "Optical guidance of terrawatt laser pulses by the implosion phase of a fast Z-pinch discharge in a gas-filled capillary." *Optics Letters*, **25** (2000) 10. doi:10.1364/OL.25.000010.

[193] Durfee, C. G., Lynch, J., *et al.* "Development of a plasma waveguide for high-intensity laser pulses." *Physical Review E*, **51** (1995) 2368. doi:10.1103/PhysRevE.51.2368.

[194] Shalloo, R. J., Arran, C., *et al.* "Hydrodynamic optical-field-ionized plasma channels." *Physical Review E*, **97** (2018) 053203. doi:10.1103/PhysRevE.97.053203.

[195] Picksley, A., Alejo, A., *et al.* "Guiding of high-intensity laser pulses in 100-mm-long hydrodynamic optical-field-ionized plasma channels." *Physical Review Accelerators and Beams*, **23** (2020) 081303. doi:10.1103/PhysRevAccelBeams.23.081303.

[196] Picksley, A., Alejo, A., *et al.* "Meter-scale conditioned hydrodynamic optical-field-ionized plasma channels." *Physical Review E*, **102** (2020) 053201. doi:10.1103/PhysRevE.102.053201.

[197] Ehrlich, Y., Cohen, C., *et al.* "Guiding of high intensity laser pulses in straight and curved plasma channel experiments." *Physical Review Letters*, **77** (1996) 4186. doi:10.1103/PhysRevLett.77.4186.

[198] Spence, D. J. and Hooker, S. M. "Investigation of a hydrogen plasma waveguide." *Physical Review E*, **63** (2000) 015401. doi:10.1103/PhysRevE.63.015401.

[199] Butler, A., Spence, D. J., *et al.* "Guiding of high-intensity laser pulses with a hydrogen-filled capillary discharge waveguide." *Physical Review Letters*, **89** (2002) 185003. doi:10.1103/PhysRevLett.89.185003.

[200] Lopes, N. C., Figueira, G., *et al.* "Plasma channels produced by a laser-triggered high-voltage discharge." *Physical Review E*, **68** (2003) 035402. doi:10.1103/PhysRevE.68.035402.

[201] Turner, M., Gonsalves, A. J., *et al.* "Radial density profile and stability of capillary discharge plasma waveguides of lengths up to 40 cm." *High Power Laser Science and Engineering*, **9** (2021/ed). doi:10.1017/hpl.2021.6.

[202] Bobrova, N. A., Sasorov, P. V., *et al.* "Laser-heater assisted plasma channel formation in capillary discharge waveguides." *Physics of Plasmas*, **20** (2013) 020703. doi:10.1063/1.4793447.

[203] Teychenné, D., Bonnaud, G., *et al.* "Electrostatic and kinetic energies in the wake wave of a short laser pulse." *Physics of Plasmas*, **1** (1994) 1771. doi:10.1063/1.870682.

[204] Shadwick, B. A., Schroeder, C. B., *et al.* "Nonlinear laser energy depletion in laser-plasma accelerators." *Physics of Plasmas*, **16** (2009) 056704. doi:10.1063/1.3124185.

[205] Esarey, E., Shadwick, B. A., *et al.* "Nonlinear pump depletion and electron dephasing in laser wakefield accelerators." In *AIP Conference Proceedings*, vol. 737, 578–584. American Institute of Physics (2004). doi:10.1063/1.1842594.

[206] Katsouleas, T. "Physical mechanisms in the plasma wake-field accelerator." *Physical Review A*, **33** (1986) 2056. doi:10.1103/PhysRevA.33.2056.

[207] Sprangle, P., Hafizi, B., *et al.* "Wakefield generation and GeV acceleration in tapered plasma channels." *Physical Review E*, **63** (2001) 056405. doi:10.1103/PhysRevE.63.056405.

[208] Rittershofer, W., Schroeder, C. B., *et al.* "Tapered plasma channels to phase-lock accelerating and focusing forces in laser-plasma accelerators." *Physics of Plasmas*, **17** (2010) 063104. doi:10.1063/1.3430638.

[209] Wen, M., Shen, B., *et al.* "Controlled electron acceleration in the bubble regime by optimizing plasma density." *New Journal of Physics*, **12** (2010) 045010. doi:10.1088/1367-2630/12/4/045010.

[210] Kim, J., Kim, G. J., *et al.* "Energy enhancement using an upward density ramp in laser wakefield acceleration." *Journal of the Korean Physical Society*, **59** (2011) 3166. doi:10.3938/jkps.59.3166.

[211] Guillaume, E., Döpp, A., *et al.* "Electron rephasing in a laser-wakefield accelerator." *Physical Review Letters*, **115** (2015) 155002. doi:10.1103/PhysRevLett.115.155002.

[212] Zhang, Z., Liu, J., *et al.* "Generation of high quality electron beams from a quasi-phase-stable cascaded laser wakefield accelerator with density-tailored plasma segments." *New Journal of Physics*, **17** (2015) 103011. doi:10.1088/1367-2630/17/10/103011.

[213] Aniculaesei, C., Pathak, V. B., *et al.* "Electron energy increase in a laser wakefield accelerator using up-ramp plasma density profiles." *Scientific Reports*, **9** (2019) 11249. doi:10.1038/s41598-019-47677-5.

[214] Litvak, A. G. "Finite-amplitude wave beams in a magnetoactive plasma." *Soviet Physics JETP*, **30** (1970) 344.

[215] Max, C. E., Arons, J., *et al.* "Self-modulation and self-focusing of electromagnetic waves in plasmas." *Physical Review Letters*, **33** (1974) 209. doi:10.1103/PhysRevLett.33.209.

[216] Sprangle, P., Tang, C.-M., *et al.* "Relativistic self-focusing of short-pulse radiation beams in plasmas." *IEEE Transactions on Plasma Science*, **15** (1987) 145. doi:10.1109/TPS.1987.4316677.

[217] Ting, A., Esarey, E., *et al.* "Nonlinear wake-field generation and relativistic focusing of intense laser pulses in plasmas." *Physics of Fluids B: Plasma Physics*, **2** (1990) 1390. doi:10.1063/1.859561.

[218] Sprangle, P., Esarey, E., *et al.* "Propagation and guiding of intense laser pulses in plasmas." *Physical Review Letters*, **69** (1992) 2200. doi:10.1103/PhysRevLett.69.2200.

[219] Lu, W., Tzoufras, M., *et al.* "Generating multi-GeV electron bunches using single stage laser wakefield acceleration in a 3D nonlinear regime." *Physical Review Special Topics - Accelerators and Beams*, **10** (2007) 061301. doi:10.1103/PhysRevSTAB.10.061301.

[220] Esarey, E., Ting, A., *et al.* "Frequency shifts induced in laser pulses by plasma waves." *Physical Review A*, **42** (1990) 3526. doi:10.1103/PhysRevA.42.3526.

[221] Ren, C., Duda, B. J., *et al.* "Compressing and focusing a short laser pulse by a thin plasma lens." *Physical Review E*, **63** (2001) 026411. doi:10.1103/PhysRevE.63.026411.

[222] Tsung, F. S., Ren, C., *et al.* "Generation of ultra-intense single-cycle laser pulses by using photon deceleration." *Proceedings of the National Academy of Sciences*, **99** (2002) 29. doi:10.1073/pnas.262543899.

[223] Gordon, D. F., Hafizi, B., *et al.* "Asymmetric self-phase modulation and compression of short laser pulses in plasma channels." *Physical Review Letters*, **90** (2003) 215001. doi:10.1103/PhysRevLett.90.215001.

[224] Faure, J., Glinec, Y., *et al.* "Observation of laser-pulse shortening in nonlinear plasma waves." *Physical Review Letters*, **95** (2005) 205003. doi:10.1103/PhysRevLett.95.205003.

[225] Hockney, R. W. and Eastwood, J. W. *Computer Simulations Using Particles.* Taylor and Francis, London (1988). ISBN 978-0-85274-392-8.

[226] Birdsall, C. K. and Langdon, A. B. *Plasma Physics via Computer Simulation.* IOP, London (1991). ISBN 978-0-7503-0117-6.

[227] Yee, K. "Numerical solution of initial boundary value problems involving maxwell's equations in isotropic media." *IEEE Transactions on Antennas and Propagation*, **14** (1966) 302. doi:10.1109/TAP.1966.1138693.

[228] Chen, W. K. *The Electrical Engineering Handbook.* Academic Press (2005). ISBN 978-0-12-170960-0.

[229] Arber, T. D., Bennett, K., *et al.* "Contemporary particle-in-cell approach to laser-plasma modelling." *Plasma Physics and Controlled Fusion*, **57** (2015) 113001. doi:10.1088/0741-3335/57/11/113001.

[230] Boris, J. P. "Relativistic plasma simulation – optimization of a hybrid code." In *Proceedings of the Conference on the Numerical Simulation of Plasmas (4th)*, 3–67. Naval Research Laboratory, Washington D. C. (1970).

[231] Vay, J.-L. "Simulation of beams or plasmas crossing at relativistic velocity." *Physics of Plasmas*, **15** (2008) 056701. doi:10.1063/1.2837054.

[232] Higuera, A. V. and Cary, J. R. "Structure-preserving second-order integration of relativistic charged particle trajectories in electromagnetic fields." *Physics of Plasmas*, **24** (2017) 052104. doi:10.1063/1.4979989.

[233] Esirkepov, T. Z. "Exact charge conservation scheme for Particle-in-Cell simulation with an arbitrary form-factor." *Computer Physics Communications*, **135** (2001) 144. doi:10.1016/S0010-4655(00)00228-9.

[234] Courant, R., Friedrichs, K., *et al.* "Über die partiellen Differenzengleichungen der mathematischen Physik." *Mathematische Annalen*, **100** (1928) 32. doi:10.1007/BF01448839.

[235] Lifschitz, A. F., Davoine, X., *et al.* "Particle-in-Cell modelling of laser–plasma interaction using Fourier decomposition." *Journal of Computational Physics*, **228** (2009) 1803. doi:10.1016/j.jcp.2008.11.017.

[236] Meyers, M. D., Huang, C. K., *et al.* "On the numerical dispersion of electromagnetic particle-in-cell code: Finite grid instability." *Journal of Computational Physics*, **297** (2015) 565. doi:10.1016/j.jcp.2015.05.037.

[237] Lehe, R., Lifschitz, A., *et al.* "Numerical growth of emittance in simulations of laser-wakefield acceleration." *Physical Review Special Topics - Accelerators and Beams*, **16** (2013) 021301. doi:10.1103/PhysRevSTAB.16.021301.

[238] Delone, N. B. and Krainov, V. P. *Multiphoton Processes in Atoms.* Springer, Berlin, 2nd ed. (2000). ISBN 978-3-540-64615-0.

[239] Posthumus, J. H., Thompson, M. R., *et al.* "Molecular dissociative ionisation using a classical over-the-barrier approach." In *7th International Conference on Multiphoton Processes*, 298–307. IOP (1997).

[240] Ilkov, F. A., Decker, J. E., *et al.* "Ionization of atoms in the tunnelling regime with experimental evidence using Hg atoms." *Journal of Physics B: Atomic, Molecular and Optical Physics*, **25** (1992) 4005. doi:10.1088/0953-4075/25/19/011.

[241] "Epoch: Particle-in-cell code for plasma physics simulations." `https://github.com/Warwick-Plasma/epoch` (2021).

[242] "Fourier-Bessel Particle-In-Cell code (FBPIC)." `https://github.com/fbpic/fbpic` (2021).

[243] Stuart, B. C., Feit, M. D., *et al.* "Nanosecond-to-femtosecond laser-induced breakdown in dielectrics." *Physical Review B*, **53** (1996) 1749. doi:10.1103/PhysRevB.53.1749.

[244] Lebugle, M., Sanner, N., *et al.* "Guidelines for efficient direct ablation of dielectrics with single femtosecond pulses." *Applied Physics A*, **114** (2014) 129. doi:10.1007/s00339-013-8153-x.

[245] Mirza, I., Bulgakova, N. M., *et al.* "Ultrashort pulse laser ablation of dielectrics: Thresholds, mechanisms, role of breakdown." *Scientific Reports*, **6** (2016) 39133. doi:10.1038/srep39133.

[246] Borot, A., Malvache, A., *et al.* "Attosecond control of collective electron motion in plasmas." *Nature Physics*, **8** (2012) 416. doi:10.1038/nphys2269.

[247] Wheeler, J. A., Borot, A., *et al.* "Attosecond lighthouses from plasma mirrors." *Nature Photonics*, **6** (2012) 829. doi:10.1038/nphoton.2012.284.

[248] Hammond, T. J., Brown, G. G., *et al.* "Attosecond pulses measured from the attosecond lighthouse." *Nature Photonics*, **10** (2016) 171. doi:10.1038/nphoton.2015.271.

[249] Sheng, Z.-M., Zhang, J., *et al.* "Plasma density gratings induced by intersecting laser pulses in underdense plasmas." *Applied Physics B*, **77** (2003) 673. doi:10.1007/s00340-003-1324-2.

[250] Sheng, Z. M., Meyer-ter-Vehn, J., *et al.* "Analytic and numerical study of magnetic fields in the plasma wake of an intense laser pulse." *Physics of Plasmas*, **5** (1998) 3764. doi:10.1063/1.872986.

[251] Pérez, F., Gremillet, L., *et al.* "Improved modeling of relativistic collisions and collisional ionization in particle-in-cell codes." *Physics of Plasmas*, **19** (2012) 083104. doi:10.1063/1.4742167.

[252] Nanbu, K. and Yonemura, S. "Weighted particles in Coulomb collision simulations based on the theory of a cumulative scattering angle." *Journal of Computational Physics*, **145** (1998) 639. doi:10.1006/jcph.1998.6049.

[253] Okuda, H. "Nonphysical noises and instabilities in plasma simulation due to a spatial grid." *Journal of Computational Physics*, **10** (1972) 475. doi:10.1016/0021-9991(72)90048-4.

[254] Yeh, P. *Optical Waves in Layered Media.* Wiley, New York (1988).

[255] Kronig, R. D. L., Penney, W. G., *et al.* "Quantum mechanics of electrons in crystal lattices." *Proceedings of the Royal Society of London. Series A, Containing Papers of a Mathematical and Physical Character*, **130** (1931) 499. doi:10.1098/rspa.1931.0019.

[256] Cohen, L. *Time-Frequency Analysis.* Prentice Hall (1995).

[257] "Scipy.signal.hilbert — SciPy v1.7.1 Manual." `https://docs.scipy.org/doc/scipy/reference/generated/scipy.signal.hilbert.html`.

[258] "Numpy.fft.fft — NumPy v1.21 Manual." `https://numpy.org/doc/stable/reference/generated/numpy.fft.fft.html#numpy.fft.fft`.

[259] Harris, C. R., Millman, K. J., *et al.* "Array programming with NumPy." *Nature*, **585** (2020) 357. doi:10.1038/s41586-020-2649-2.

[260] Shurcliff, W. A. *Polarized Light: Production and Use.* Harvard University Press, Cambridge, Massachusetts (1962).

[261] Fowles, G. R. *Introduction to Modern Optics.* Dover Publications, New York (1989). ISBN 0-486-65957-7.

[262] Dover, N. "Overdense gas jets for ion acceleration studies." (2012).

[263] Kruer, W. *The Physics of Laser Plasma Interaction.* Addison-Wesley, Reading, MA (1988).

[264] Matsuoka, T., McGuffey, C., *et al.* "Stimulated Raman side scattering in laser wakefield acceleration." *Physical Review Letters*, **105** (2010) 034801. doi:10.1103/PhysRevLett.105.034801.

[265] Hooker, C. J., Collier, J. L., *et al.* "The Astra Gemini petawatt Ti:sapphire laser." *The Review of Laser Engineering*, **37** (2009) 443. doi:10.2184/lsj.37.443.

[266] George, N. and Morris, G. M. "Diffraction by serrated apertures." *JOSA*, **70** (1980) 6. doi:10.1364/JOSA.70.000006.

[267] O'Shea, P., Kimmel, M., *et al.* "Highly simplified device for ultrashort-pulse measurement." *Optics Letters*, **26** (2001) 932. doi:10.1364/OL.26.000932.

[268] McClain, S. C., Bartlett, C. L., *et al.* "Depolarization measurements of an integrating sphere." *Applied Optics*, **34** (1995) 152. doi:10.1364/AO.34.000152.

[269] Peng, H., Riconda, C., *et al.* "Dynamical aspects of plasma gratings driven by a static ponderomotive potential." *Plasma Physics and Controlled Fusion*, **62** (2020) 115015. doi:10.1088/1361-6587/abb3aa.

[270] Blanc, S. P. L., Sauerbrey, R., *et al.* "Spectral blue shifting of a femtosecond laser pulse propagating through a high-pressure gas." *JOSA B*, **10** (1993) 1801. doi:10.1364/JOSAB.10.001801.

[271] Lehmann, G. and Spatschek, K. H. "Plasma volume holograms for focusing and mode conversion of ultraintense laser pulses." *Physical Review E*, **100** (2019) 033205. doi:10.1103/PhysRevE.100.033205.

[272] Lehmann, G. and Spatschek, K. H. "Plasma photonic crystal growth in the trapping regime." *Physics of Plasmas*, **26** (2019) 013106. doi:10.1063/1.5079810.

[273] Langdon, A. B. "Kinetic theory for fluctuations and noise in computer simulation of plasma." *The Physics of Fluids*, **22** (1979) 163. doi:10.1063/1.862452.

[274] "Scipy.ndimage.uniform_filter1d — SciPy v1.7.1 Manual." `https://docs.scipy.org/doc/scipy/reference/generated/scipy.ndimage.uniform_filter1d.html`.

[275] Brunetti, E., Yang, X., *et al.* "Wide-angle electron beams from laser-wakefield accelerators." In *Laser Acceleration of Electrons, Protons, and Ions IV*, vol. 10240, 61–72. SPIE (2017). doi:10.1117/12.2269314.

[276] Valenta, P., Grittani, G. M., *et al.* "On the electromagnetic-electron rings originating from the interaction of high-power short-pulse laser and underdense plasma." *Physics of Plasmas*, **28** (2021) 122104. doi:10.1063/5.0065167.

[277] Floettmann, K. "Some basic features of the beam emittance." *Physical Review Special Topics - Accelerators and Beams*, **6** (2003) 034202. doi:10.1103/PhysRevSTAB.6.034202.

[278] Ferran Pousa, A., Martinez de la Ossa, A., *et al.* "Intrinsic energy spread and bunch length growth in plasma-based accelerators due to betatron motion." *Scientific Reports*, **9** (2019) 1. doi:10.1038/s41598-019-53887-8.